EINDHOVEN UNIVERSITY OF TECHNOLOGY
Eindhoven University of Technology

MASTER

Towards all electrical spin injection and detection in GaAs in a lateral geometry

Schoonus, J.J.H.M.

Award date:
2004

Link to publication

Disclaimer
This document contains a student thesis (bachelor's or master's), as authored by a student at Eindhoven University of Technology. Student theses are made available in the TU/e repository upon obtaining the required degree. The grade received is not published on the document as presented in the repository. The required complexity or quality of research of student theses may vary by program, and the required minimum study period may vary in duration.

General rights
Copyright and moral rights for the publications made accessible in the public portal are retained by the authors and/or other copyright owners and it is a condition of accessing publications that users recognise and abide by the legal requirements associated with these rights.

- Users may download and print one copy of any publication from the public portal for the purpose of private study or research.
- You may not further distribute the material or use it for any profit-making activity or commercial gain

Eindhoven University of Technology
Department of Applied Physics
Group Physics of Nanostructures

Towards all electrical spin injection and detection in GaAs in a lateral geometry

J.J.H.M. Schoonus

August 2004

Report of a graduation project from September 2003 to August 2004, carried out at the Eindhoven University of Technology in the group Physics of Nanostructures

Supervisors:	dr. A.T. Filip
	dr. ir. H.J.M. Swagten
Groupleaders:	prof. dr. B. Koopmans
	prof. dr. ir. W.J.M. de Jonge

FNA

Abstract

The realization of fully electrical semiconductor-based devices making use of the electron spin is an important challenge. We discuss our approach of all electrical spin injection and detection in GaAs. The envisioned device consists of two ferromagnetic electrodes crossing an n-doped epitaxial grown GaAs channel. AlOx tunnel barriers are to be used in order to overcome the impedance mismatch and different width of the electrodes ensures difference in coercive fields.

We performed a detailed theoretical analysis of the expected magnetoresistance, based on a Boltzmann formalism. Differences in behavior between our lateral and the common well known vertical device, the influence of the electric field (applied bias) and the opportunities offered by measurement geometries were explored. On a GaAs (100) undoped wafer, 100 nm $Al_{0.3}Ga_{0.7}As$ for electrical confinement, 100 nm n-doped ($4{\cdot}10^{17}$ cm^{-3} Si) GaAs and $3{\times}2.5$ nm n^{++} δ-doped ($5{\cdot}10^{13}$ cm^{-2} Si) GaAs, to suppress the Schottky barrier are MBE grown respectively. Finally 1.5 nm of Al is grown and oxidized naturally in order to obtain a homogeneous insulating layer, which will act as a tunnel barrier. On top of the AlOx, with in-situ shadow masks, a 0.1 mm wide channel is defined, by covering the rest of the sample with a thick insulating SiO_2 layer. Large Ta bonding pads were deposited on the SiO_2 for external wiring. With e-beam lithography and afterwards a sputtering step, a 500 nm and a 1000 nm wide and 0.1 mm long $Co_{90}Fe_{10}$ electrodes, 1 μm separated of eachother, were obtained.

Measured I-V characteristics of the CoFe/AlOx/GaAs interface corresponds with tunneling as the main injection mechanism. However, the measured silicon doping was fifty times higher then intended, leading to a too low square resistance of our n-doped GaAs layer (51 Ω) compared with the resistance $\times$ area product of the tunnel barrier ($5 \cdot 10^{12}$ $\Omega \cdot \mu m^2$). Therefore the magnetoresistance was quenched and no spintransport could be observed. Experiments are in progress to optimize the resistance ratio between the tunnel barrier and semiconductor transport channel.

Contents

1 Introduction and Technology Assessment **1**

1.1 Spintronics: a review 1

1.2 This thesis 4

2 Theoretical concepts in describing spin polarized transport **6**

2.1 Basic theoretical concepts 6

2.1.1 GaAs/metal interfaces and Schottky barrier formation 6

2.1.2 Free electron tunneling and spin polarization 8

2.2 Spin relaxation 10

2.3 Spin polarized electron transport 12

2.3.1 Spin injection and accumulation: the basic idea 13

2.3.2 Boltzmann equation model 14

2.3.3 Macroscopic spin transport model 18

2.3.4 Carrier density versus electrochemical potential 20

2.3.5 Magnetoresistance 21

2.3.6 Resistor model 31

3 Towards electrical detection of spin accumulation in GaAs **34**

3.1 Design requirements 34

3.2 Device layout and characteristic dimensions 35

3.2.1 Magnetization reversal via uniform rotation 39

3.3 Sample fabrication techniques 41

3.3.1 Sputtering 41

3.3.2 Molecular Beam Epitaxy 42

3.3.3 Electron Beam Lithography 42

3.4 Sample fabrication 43

3.5 Characterization techniques 45

3.5.1 Transport measurements 45

3.5.2 The Van der Pauw method 46

3.5.3 Hall effect 48

3.6 Results 48

3.6.1 GaAs wafer characterization 48

3.6.2 Insulator choice and characterization 49

3.6.3 Tunnel barrier characterization 50

3.6.4 Transport measurements 51

4 Conclusions and outlook **54**

5 Appendix **59**

Chapter 1

Introduction and Technology Assessment

Until recently, mainstream electronics was exclusively based on charge properties. A newly emerging approach is the use of not only the charge but also the intrinsic angular momentum of the electron to which a magnetic moment is directly coupled [1]. The quantization of the spin for a free electron imposes that whenever measurements are done along a certain direction there are only two possible outcomes: namely spin-up and spin-down. Interaction via coupling of this intrinsic magnetic moment to an external magnetic field results in a shift in energy levels of the two eigenstates. In general this difference in energy is much smaller as the Fermi energy and the effects on transport should be negligible. Elementary ferromagnetic transition (3d) metals, in which an intrinsic inequivalence between two spin eigenstates is present, are an exception. Due to the negative sign of the quantum mechanical exchange interaction, the spins of the electrons tend to align parallel. For the two spin-subbands a difference in density of states at the Fermi-energy as well as in Fermi-velocities exists, resulting in spin depending bulk conductivities.

Through incorporation of the electron spin in the existing electronic devices the fields of magnetism and electronics could overlap. Magneto-electronics is already applied in sensor industry and is regarded as the technological basis for future logical electronic devices. The key advantage of magnetism is hysteresis, which leads to non-volatility. Other potential advantages are increased data processing speed, decreased electric power consumption, and increased integration densities. Moreover, it could be interesting for quantum computing, since the intrinsic binary and quantum mechanical nature of electron spin suggests its usage as basic unit, the qubit, for quantum information storage and processing. As spin interactions with the environment and with other spins are much weaker than Coloumb interactions, spin coherence is preserved on much longer time scale compared to charge. For better electronic devices and quantum computation applications, one has to resolve physical questions and technical issues such as efficient injection of electrons with preferable only one spin direction into a normal (non-magnetic) material, transport of the excess spin in the normal material, control and manipulation, and detection at different spatial position of spin accumulation as well as spin-polarized currents. Here, the term spin accumulation refers to the thermodynamic inequilibrium of spin-up and spin-down electrons in non magnetic metals. The unbalance is normally maintained by an applied bias voltage. We shortly review the spin-based devices and issues in spin transport, which are significant for full electrical manipulation of inhomogeneous electron spin currents.

1.1 Spintronics: a review

The first observations of transport properties being influenced by magnetic properties was the anomalous magneto resistance effect(AMR) (see figure 1.1a). The resistance of a metallic fer-

romagnet is dependent on the angle between the magnetization and current direction. The physical origin is the s-d band scattering induced by an external magnetic field, and is dependent on the wave vector of the electron. Higher effective mass of the d band provided an increase in resistivity when electrons are scattered from the s band into the d band [2, 3].

Experimentally, the first determination of the spin polarization of the conduction band in a ferromagnetic material has been performed by Tedrow and Meservey [4]. They studied the magnetoconductance of a ferromagnet/Al_2O_3/Al tunnel junction. If spin and total current is conserved during the process, the tunnelling current between two metallic electrodes separated by a thin insulating layer depends on the products of density of states of the two electrodes. In superconducting Al, through Zeeman splitting of the two sharp BSC peaks in densities of states at the Fermi level, the spin polarization at the Fermi level is exactly known.

In 1989 Baibich *et al.* observed a strong dependence in the resistance of a ferromagnetic-metal multilayer as function of the relative parallel/anti-parallel alignment of the ferromagnetic layers [5]. This effect, named giant magneto resistance (GMR), is the first effect directly related to spin transport (see figure 1.1b). There are two contributions: the conductivity of a bulk ferromagnet and the specific interface transmission of a clean ferromagnet/non-metal interface will both depend on the spin specific subband index. In anti-parallel alignment the majority carriers in one layer become the minority in the other and the other way around. The spin subband dependent interface transmissivities are reversed, resulting in spin accumulation near the interface and relative to parallel alignment a higher resistivity.

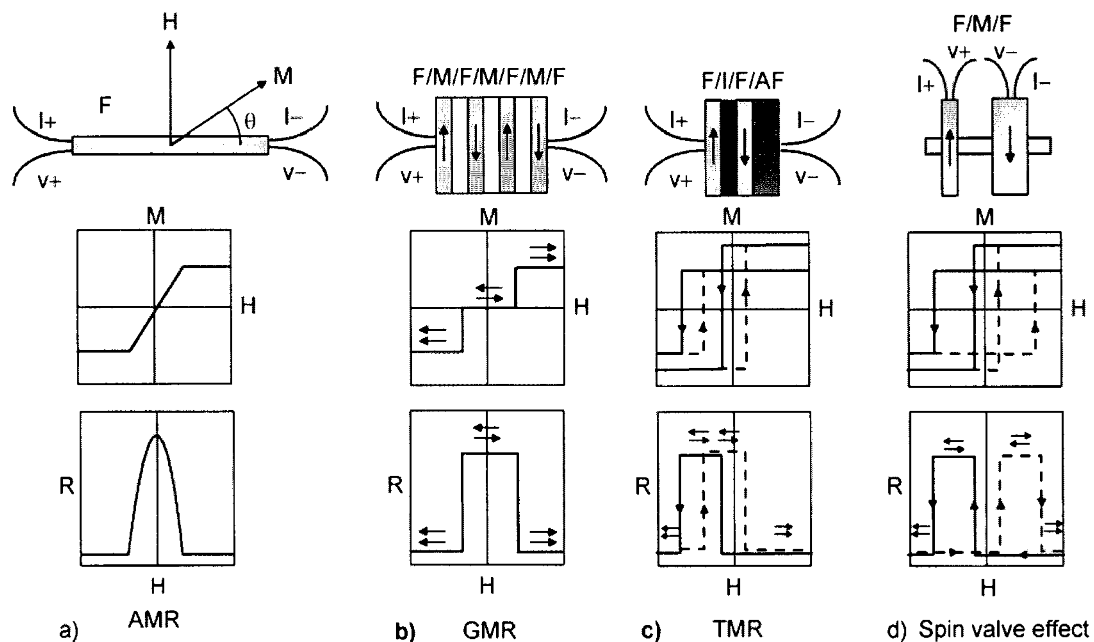

Figure 1.1: a) AMR effect: In a ferromagnetic thin film F the resistance R is dependent on the angle θ between the magnetization M (due to an applied field H) and the direction of the current I. The hysteresic curve is also shown. b) GMR effect: In a ferromagnet-metal(M)-ferromagnet the resistance is dependent on the relative orientations of the magnetizations. c) TMR effect: In a exchanged bias tunnel junction (ferromagnet -isolator(I)-ferromagnet), the resistance is dependent on the relative orientation of the magnatizations. One layer is pinned by an anti-ferromagnet AF. d) Spin valve effect: Through shape anisotropy two ferromagnetic layers have different coercive fields. Via the first ferromagnet, a spin current is injected into a non-magnetic metal. If the second ferromagnet is fully spin-polarized, it will only be sensitive to the respective spin population. The resistance is dependent on the relative orientation of the magnetization of the two electrodes.

Based on early measurements, Julliere [6] showed in 1975 that the conductance in a ferromagnet-isolator-ferromagnet junction is different when the magnetization directions of the

two ferromagnetic layers are parallel or anti-parallel. This effect is called the tunnel magnetoresistance (TMR), and is related to the tunneling current, which is dependent on the the products of the density of states for each subband and the specific transmission coefficients for each subband (figure 1.1). Different magnetization orientations are obtained by exchange biasing via an anti-ferromagnet/ferromagnet coupling or by different coercive fields. In 1995 Moodera *et al.* [7] succeeded in developing a fabrication process for good tunnel barriers and demonstrated this spin valve effect more clearly.

The most important recent results on spin polarized transport will be very briefly discussed in the following part of this section. From a fundamental point of view, one is interested in injecting non-equilibrium spin population in a non magnetic material and how it is transported. Electrical spin injection was realized by Johnson and Silsbee [8], who demonstrated spin accumulation and precession in a single crystal aluminium bar. They observed that the total conductance of an permalloy-aluminium-permalloy spin valve (magnetization of permalloy electrodes remains fixed in a certain direction) varied periodically with a perpendicular applied magnetic field. The injected spins coherently precess periodically with the external magnetic field and a changing effective direction of the spins is seen by the detecting electrode. However their results are rather controversial, not in the last place because of the extremely small signals in the pV range. The first active device, an electron wave analog (spin-FET) of the electro-optic light modulator was proposed by Data and Das [9]. Current modulation in the proposed structure arises from spin precession due to an asymmetric quantum well, while magnetized contacts are used to preferentially inject and detect specific spin orientations.

This has attracted growing interest in realizing spin injection in semiconductor heterostructures and the first all optical results were reported by Kikkawa and Awschalom [10, 11]. Excitation by normally incident pulses of circularly polarized light produces a conduction-band spin imbalance, whose degeneracy is removed by a transverse magnetic field. The quantum coherent beating between these states results in Larmor precession of the classical spin vector. The ensemble-average projection is measured with a time-delayed probe pulse, whose lineair polarization rotates an amount proportional to the electric magnetization upon transmission through the sample. Macroscopic lateral transport of coherently precessing electronic spins over distances exceeding 100 μm was found in n-type bulk gallium arsenide.

In contrast to optical experiments, initial attempts to realizing spin injection via ferromagnet-semiconductor contacts failed or proved unreliable. Schmidt *et al.* [12, 13] reported that the ratio between the resistivity of the ferromagnet and the resistivity of the nonmagnetic semiconductor is commonly unfavorable for spin injection. The result is a major obstacle for injection experiments, commonly referred as the impedance mismatch problem. Rashba [14] proposed that a tunnel barrier could be a way to overcome this problem. Electrical spin injection by optical detection was proved by Fiederling *et al.* [15] and simultaneously by Awschalom *et al.* [16]. The large electronic Zeeman splittings in diluted magnetic semiconductors, at low temperatures and high magnetic fields enabled Fiederling to drive a fully spin-aligned current intro a light emitting diode to subsequently look to the polarization of the emitted light. Zhu *et al.* [17] demonstrated injection of spin polarized electrons from Fe into a GaAs(In,Ga)As light emitting diode. Again the circular polarization degree of the observed electroluminescence reveals the spin injection efficiency. The underlying injection mechanism is explained in terms of a tunnelling process. Another possibility, but not pratical in devices, is tunnel injection by ferromagnetic STM tips [18]. The first use of an AlO_x tunnel barrier for electron spin injection from a ferromagnetic metal into a III-V semiconductor LED was in the experiments of Montsnyi *et al.* [19].

One of the main challenges for device implementation is now the efficient creation of a spin-polarized ensemble within a semiconductor and subsequent electrical detection. The first related results were reported by Tanaka *et al.*, who observed a tunneling magneto resistance in epitaxially grown GaMnAs/AlAs/GaMnAs ferromagnetic semiconductor tunnel junctions [20]. Subsequent, Hu *et al.* [21], investigated ferromagnetic metal contacts on a InAs two-dimensional electron gas and claimed to have measured spin injection and detection. Besides the fact that

their geometry may suffer from local Hall effects, at low temperatures semiconductors show strong weak localization corrections to the conductance. Due to dependence on the local magnetization of the contacts via the stray fields, these spurious phenomena often closely resemble the signals expected from spin transport [13]. New attempts focussed on making use of the Rashba spin-orbit interaction as a detection mechanism. Meier *et al.* [22] observed from temperature and gate-voltage dependence oscillatory changes in the resistance of MOSFET's with ferromagnetic contacts when an external, magnetic field is applied along the current direction. Nevertheless weak localization effects cannot be fully excluded in this case either. Recently, Mattana *et al.* [23] created spin accumulation from a GaMnAs ferromagnet through an AlAs barrier into a p-type GaAs quantum well. The created spin accumulation is electrical detected by a same multilayer. Their results account for a sequential tunnelling with a non relaxed spin splitting of the chemical potential of the holes in GaAs.

1.2 This thesis

The objective of this thesis is to demonstrate electrical injection of a non-equilibrium spin population of electrons in GaAs and subsequently electrical detection. The realization of fully electrical devices still remains an important challenge in the field of spintronics, because presently most consumer products are electric ones. The aim of this project is considered as a proof of principle. The research of spintronics became interested in semiconductor materials, which offer the possibility of new device functionalities not realizable in metallic systems. The device impedance is controllable over a wide range via doping. Furthermore, because the typical carrier densities in semiconductors are low compared to metals, electronic properties are easily tunable by gate potentials. For constructing multi functional devices a long coherence length is desirable. Spin polarized electrons are, especially in GaAs, less subject to spin flip than holes and thus have a longer spin flip time. Spin is a good quantum number for electrons in the conduction band and the spin can only be changed via spin-orbit interaction or electron-electron scattering. In contrast for holes the angular momentum and spin are not separately preserved, therefore momentum scattering by Coloumb interaction through impurities induces also spin flip transition.

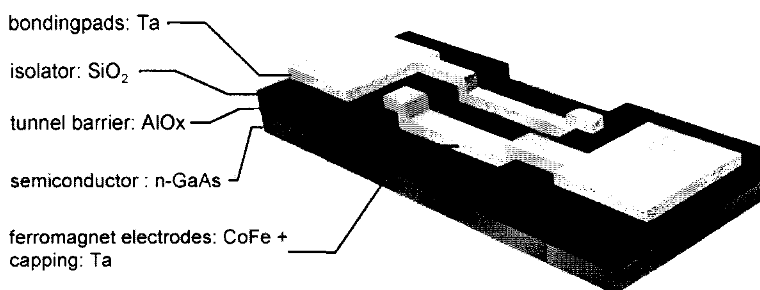

Figure 1.2: Schematic overview of a fully electrical semiconductor-based spin valve device. Dimensions are not drawn to scale.

A critical issue is to find a method to isolate in a reliable way spin accumulation from all other magneto resistive effects. Our envisioned device will be based on a combination of ideas from earlier work by Jedema *et al.* [24, 25] and Montsnyi *et al.* [19]. Jedema performed electrical spin injection and detection measurements on all metal systems. His device consists of two ferromaganetic electrodes, crossing a metal wire 1.1d. Secondly, it has been shown by Motsnyi that efficient spin injection can be achieved from a ferromagnetic metal into a semiconductor by using an AlOx tunnel barrier to overcome the impedance mismatch (see section 1.1). In order

to use 'standard' epitaxially grown GaAs wafers, we propose analog to the devices of Jedema, a lateral geometry (see figure 1.2). In our case the metal transport channel will be replaced by a GaAs wafer. In between the GaAs wafer and the ferromagnetic electrodes on top of the GaAs substrate, an AlOx layer is grown. The small ferromagnetic electrodes have to be electrically connected via large bonding pads to external wiring. The bonding pads are deposited next to the electrodes, and will be isolated from the substrate by a thin SiO_2 layer. Control over the magnetic properties of injector and detector electrodes is gained by the control of coercivity via shape anisotropy (this will be explained in full detail in § 3.2.1).

Having discussed the main goal, motivation and proposed structure of the device, we present a brief outline of this thesis. In chapter 2, relevant theory for the analysis of the design and experimental results is discussed. Especially, a fundamental derivation is given for the macroscopic spin transport model including electric field effects [26] and subsequent this macroscopic model is applied to our devices. The requirements and correlated layout analysis is described in the first section of chapter 3. For the sample fabrication the most important techniques and in more detail all steps and encountered difficulties are explained. Next we briefly presents the characterization techniques, followed by experimental characterization of the individual parts of the device and an outlook of the desired results. Finally in chapter 4 the conclusions are drawn and an outlook for further research is given. In the appendix some valuable drawings are compiled.

Chapter 2

Theoretical concepts in describing spin polarized transport

In this chapter a model describing spin polarized transport in semiconductors is introduced. For a better understanding of this model and the design of our device, we will first discuss some basic theoretical concepts like Schottky barriers, free electron tunneling, spin polarization and spin relaxation. Before we introduce the Boltzmann model and the macroscopic spin transport model, we will first explain the basic idea of spin injection and spin accumulation. Finally the presented theory will be applied on several device and measurement geometries.

2.1 Basic theoretical concepts

2.1.1 GaAs/metal interfaces and Schottky barrier formation

Realization of electrical spin injection or detection requires somehow a metal- (isolator-) semiconductor contact. In this section the specific physics of such contacts is discussed. Let us consider in general a metal/isolator/GaAs system. Near the interface there may be a high density of extra electronic states due to breakdown of the periodic boundary conditions [27, 28]. The surface states do not obey Bloch's theorem, because their reciprocal wavevector (in the direction normal to the interface plane) is imaginary. Therefore they bear no relation to the band structure of the rest of the material; in particular the states are localized and a non propagating wave does not contribute to transport. In GaAs, these states occupy a narrow band of energies near the middle of the band gap at $\phi \approx 0.7\ eV$ below the conduction band, with e the electron charge. The Fermi level of a layer is then always pinned within this band, because it seems impossible to put enough charge into the surface states to fill the empty band and allow the Fermi level to leave it. Through this charge accumulation, the conduction band is forced to meet the surface of GaAs at an energy ϕ above the local Fermi level. This results in the formation of a Schottky barrier.

In figure 2.1 the bandstructure of a CoFe/Al_2O_3/n-GaAs/$Al_{0.3}Ga_{0.7}As$ system, similar to the envisioned injection part of our device, is drawn. A Schottky barrier will form at the interface of the n-doped GaAs with the Al_2O_3 as well as at the interface with the $Al_{0.3}Ga_{0.7}As$. The semiconductor transport channel is now given by the n-doped GaAs layer, called the active layer. In particular there will be charge transfer from the bulk donors to the surface states. Positive charged localized ions remain in the active layer (see figure 2.2b and c). A depletion region is formed over the distance where the electrons are removed. If an active layer with a well defined carrier density is desired, we do not want that a large fraction of the carriers is needed to neutralize the undesired barrier states. In order to suppress the Schottky barrier an extra thin layer of semiconductor with an adapted much higher doping profile is inserted at the place where the Schottky barrier is formed. Now it is these extra dopants instead of the dopants in the active layer, the ones neutralize the barrier states. Figure 2.2a shows a

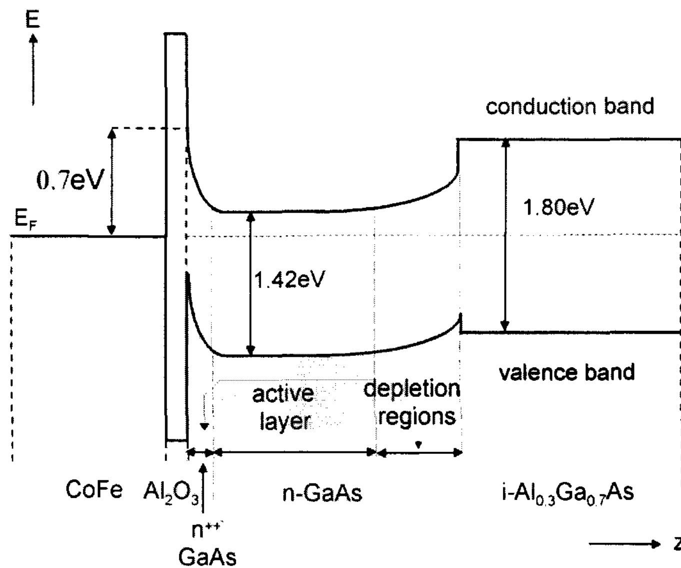

Figure 2.1: Band structure of the valence and conduction band for a CoFe/ Al_2O_3/ n^{++}-GaAs/ n-GaAs/ $Al_{0.3}Ga_{0.7}As$. Shaded areas represent filled states, open areas are empty states.

redrawn representation of the GaAs/Al_2O_3 interface. This idealized controlled barrier contact consists of a variable number x of delta-doped n^{++} (all dopants within a single monolayer, with total surface concentration n^{++}) layers at distances a. The effective barrier height and depth can be tuned by controlling their number of delta doped layers, the spacing between them and the doping concentration. The advantage of using delta-doped layers instead of a homogenous doping, is that the probability of scattering is smaller, because of less randomly localization. In this way the mobility is not decreased. The behavior of the conduction band as a result of the charge density of Schottky suppression layer can be calculated by solving Poisson's equation. The condition for a perfectly balanced interface is as follows: all the surface charge has to equal the amount of charge needed to compensate a Schottky barrier height ϕ. The Schottky barrier height is set equal to the maximum height that can be compensated by the charge;

$$\phi = \frac{x(x+1)}{2}\frac{n^{++}e}{\varepsilon_0\varepsilon_r}a, \tag{2.1}$$

where ε_0 is the dielectric permittivity of vacuum and ε_r the relative dielectric permittivity of the semiconductor. A combination of the parameters x, a and n^{++} should be chosen such that the surface states are exactly compensated by the extra charge. In the case of silicon doping in GaAs [100], the delta doping layer density is limited to a certain maximum where the implanted dopants forms bindings to each other, that is they share the common electron. Equation 2.1 is then not valid anymore. If total charge of the Schottky suppression layer exceeds the threshold concentration, overcompensation is present. The surface states are filled by just a part of the donors in the n^{++} δ-doped layer (see figure 2.2b). The remaining uncompensated dopants will donate their charge to the active layer, and the effective concentration increases. In case of undercompensation (see figure 2.2c) we obtain the same problem as described in absence of the Schottky suppression layer. All the donors in the n^{++} δ-doped layer plus a part of the donors in the active n-doped layer are needed to compensate the surface states. The doping concentration in the active layer is less than intended. A depletion region is formed over the depth where dopants generates electrons that become localized at the surface.

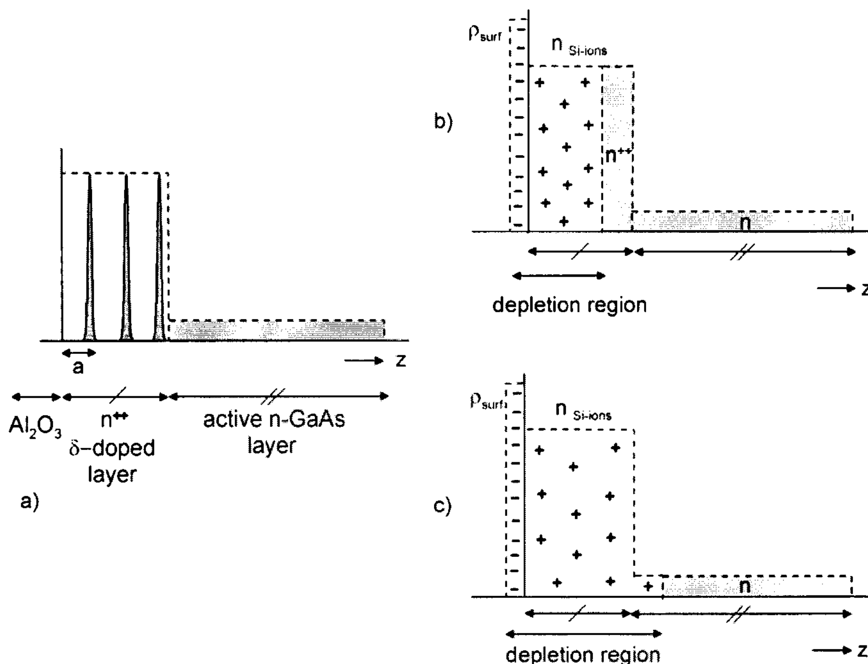

Figure 2.2: (a) Si-doping concentration as function of depth of the GaAs layer. (b) Overcompensation: the surface states are occupied by a part of the n^{++}-doping in the Schottky suppression layer, the rest will be donated to the active layer. The active layer is now too heavily doped. (c) Undercompensation: the surface states are occupied by all the n^{++}-doping in Schottky suppression layer and a part of the n-doping present in the active layer. The active layer is now too lightly doped.

2.1.2 Free electron tunneling and spin polarization

Electron tunneling is a quantum phenomenon by which an electric current may flow from one electrode, through an insulating barrier into another electrode [29]. An electron wave encountering a potential barrier, will be partially reflected and partially transmitted through the barrier. Inside the barrier the wave will decay exponentially. For sufficiently thin barriers a finite intensity of the electron wave reaches the other side, so the probability is finite that the electron is localized there (see figure 2.3). The most straightforward implementation is a metal-insulator-metal trilayer structure, in which the insulator is typically provided by a metal oxide. The tunneling can be studied by measuring the current as function of the bias voltage across the junction. Due to a bias voltage V_b, the right Fermi-level shifts eV_b with respect to the left electrode. The tunnel current density $J_{l\to r}$ from left to right is given by [30]:

$$J_{l\to r}(V_b) \propto \int_{-\infty}^{+\infty} dE N_l(E) N_r(E - eV_b)|T|^2 f(E)[1 - f(E - eV_b)] \tag{2.2}$$

where $N_{l(r)}$ is the density of states for the left (right) electrode and $|T|^2$ the transmission probability. The terms $f(E)$, the Fermi Dirac distribution and $[1 - f(E - V_b)]$, expresses the requirement that the states in the left electrode has to be occupied to tunnel to an empty state in the right electrode. The integral is taken over the whole energy range, although at low bias only the Fermi surface properties matter. The total current is now $J_{l\to r}$-$J_{r\to l}$. Simmons [31] used the WKB approximation to calculate the transmission probability for an arbitrary barrier of thickness d and of average height $\bar{\phi}$ above the Fermi-energy. The current density at $T = 0$, using a free electron relation for $N_{\uparrow(\downarrow)}$ and approximating the Fermi-Dirac functions as step

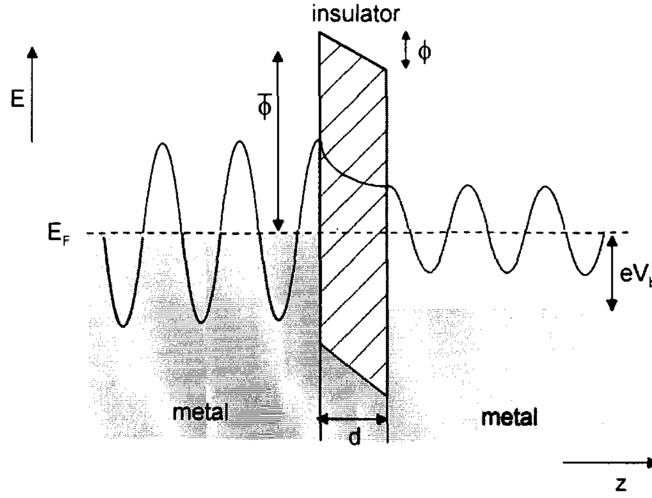

Figure 2.3: Potential diagram for tunneling in metal-isolator-metal structures. Shaded areas represent filled states, open areas are empty states, and the hatched area represents the forbidden gap in the insulator. Over the insulating barrier, with thickness d, a bias voltage V_b is applied. An incoming electron wave is partially reflected (not shown) and partially transmitted through the barrier. In the barrier region the electron wave function decays exponentially.

functions is:

$$J = \frac{e^2}{2\pi h d^2}\left(\frac{\bar{\phi}}{e} - \frac{V_b}{2}\right) exp\left[\frac{-4\pi d\sqrt{2m_e^*}}{h}\left(\frac{\bar{\phi}}{e} - \frac{V_b}{2}\right)^{\frac{1}{2}}\right] - \frac{e^2}{2\pi h d^2}\left(\frac{\bar{\phi}}{e} + \frac{V_b}{2}\right) exp\left[\frac{-4\pi d\sqrt{2m_e^*}}{h}\left(\frac{\bar{\phi}}{e} + \frac{V_b}{2}\right)^{\frac{1}{2}}\right] \tag{2.3}$$

with h Planck's constant and m_e^* the effective electron mass in the barrier conduction band. At moderate bias voltages the conductance dJ/dV_b increases parabolically, and the tunnel current goes inversely exponential with the barrier thickness. For a tunnel junction with different electrode materials, the difference in barrier height at both metal-isolator interfaces makes the barrier potential canted, resulting in an asymmetric current voltage behavior. Brinkman *et al.* [32] have addressed this problem under introducing an extra parameter to account for the tilted barrier. Brinkman found:

$$J = \frac{e^2\sqrt{2m_e^*}\sqrt{\bar{\phi}}}{h^2 d}\exp\left(\frac{-4\pi d\sqrt{2m_e^*}\sqrt{\bar{\phi}}}{h}\right)\left(V_b - \left(\frac{\pi\sqrt{2m_e^*}e}{12h}\frac{d\Delta\phi}{\bar{\phi}^{3/2}}\right)V_b^2 + \left(\frac{\pi^2 m_e^* e^2}{3h^2}\frac{d^2}{\bar{\phi}}\right)V_b^3\right) \tag{2.4}$$

with $\Delta\phi$ the difference between the barrier height at the right interface minus that at the left interface and $\bar{\phi}$ the average barrier height.

In the approaches of Simmons and Brinkman any dependence of the transport characteristics on the electronic density of states in the electrodes is assumptions absent. The presence of the interactions responsible for ferromagnets in electrodes, changes the way the transmission probability and the density of states in equation (2.3) should be treated. In ferromagnets an effect of the exchange splitting is that the density of states at the Fermi-energy and the Fermi velocities become different for the two spin sub-bands. In fact, the transmission coefficients represents the overlap of the electrode wave functions in the barrier region where many-body interactions are no longer present and can be dependent on $N_{\uparrow(\downarrow)}$. For the density of states one should not take the bulk, but rather those of the metallic electrodes in a strongly perturbed region (a few Fermi wavelengths) near interface, implying that the tunnel characteristics, such

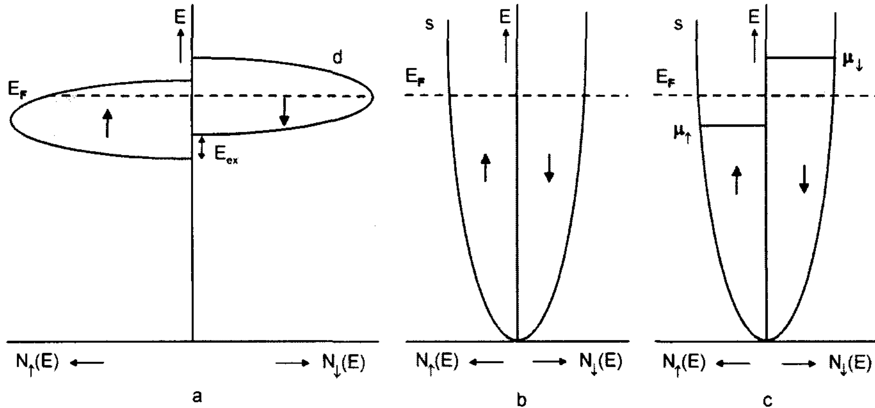

Figure 2.4: (a) Schematic representation of the spin dependent DOS and occupation of the d states in a ferromagnetic material. (b) Unpolarized DOS of the free electron like s states in a non magnetic metal. (c) Spin accumulation in a non magnetic metal: the induced magnetization. The non-equilibrium population of the spin-up and spin-down states is caused by the injection of spin polarized current.

as spin polarization will be highly susceptible to the interface quality as result of the growth. Typically a tunneling spin polarization P is now defined for vanishing bias and independent of the wave vector parallel to the surface by

$$P(V_b = 0) = \frac{N_\uparrow |T_\uparrow|^2 - N_\downarrow |T_\downarrow|^2}{N_\uparrow |T_\uparrow|^2 + N_\downarrow |T_\downarrow|^2} \tag{2.5}$$

in which the density of states are taken at the Fermi surface and weighted by the transmission probability, expressing the influence of the isolating material [30]. For non-vanishing bias, the energy dependence of the transmission probability and the density of states must be taken into account as well when integrating over all energies in (2.3), although only the energy range where there are filled states in one electrode and empty states in the other will contribute. In tunneling spin polarization experiments (see section 1.1) positive values were found for P [4]. The experimental determined polarization for Co is 40%. The most striking feature of this results was the fact the tunneling spin polarization of 3d ferromagnetic metals was positive (i.e. spin up majority) in all cases, seemingly at odds with the bulk band structures of these materials, which show a dominant minority contribution to the density of states at the Fermi level. For more in-depth discussions about tunneling spin polarization, we refer the reader to the references [33, 34, 35]. We point out that the situation becomes even more complex for non-epitaxial electrodes and amorphous barriers, when wave vector conservation rules are broken. Even when the parallel wave vector conservation is taken into account, transport characteristics becomes a complex function of the wave vector, barrier thickness and asymmetrical Bloch states.

2.2 Spin relaxation

Spin relaxation refers to interactions that bring an unbalanced population of spins, equivalent to a non-equilibrium magnetization, into equilibrium. Two types of relaxation processes can be identified, processes which require energy exchange with the environment and processes induced by mutual exchange. In order to discriminate the two processes, a good quantization axis is defined by an external applied magnetic field **B**. S_0 is the equilibrium spin along the quantization axis. The spin component along the spin quantization axis decreases as individual spins flip, bringing the populations towards equilibrium. Because the total momentum has to be

conserved, this direct process requires energy relaxation towards the lattice. The second type of process, i.e. spin-spin relaxation, can destroy the perpendicular component and for this no netto energy exchange with the outside world is necessary. Every spin sees the magnetic field created by adjoining spins, therefore precessing in a local field which contains a random component. The motion of the spin due to the two processes will be described by the Bloch equations:

$$\frac{\partial S_{\parallel}}{\partial t} = -\frac{(S_0 - S_{\parallel})}{T_1}, \tag{2.6}$$

$$\frac{\partial S_{\perp}}{\partial t} = \gamma(\mathbf{B} \times \mathbf{S})_{\perp} - \frac{(S_{\perp})}{T_2} \tag{2.7}$$

where γ is the gyromagnetic ratio and $\mathbf{S}$ the total spin. The terms $\parallel$ and $\perp$ describe the components parallel and perpendicular tot the quantization axis. The time constants T_1 and T_2 describe the decay of the longitudinal and transverse spin order and they are analogous to the constants introduced to describe nuclear magnetic resonance (NMR) experiments. Because T_1 normally exceeds T_2, the last will be used as spin life time in the following sections ($\tau_{sf} = T_2$) and can be obtained in electron spin resonance (ESR) measurements. Interactions between spins and other degrees of freedom affect the original spin states, therefore they are not anymore the real eigenstates and their lifetime become finite.

The only possible interaction for the spin degree of freedom is with a magnetic field, which can be either externally applied or generated by spin-orbit interaction. Spin-orbit interaction is a relativistic effect that occurs when a quantum mechanical particle with a non zero spin moves in a region with a non-zero electric field. If an electron moving with relativistic velocities in a static electric field, in the rest frame of the electron the original electric field transforms into a field that has also a magnetic component. This effective magnetic field in the rest frame of the electron effects the dynamics and the total energy of the electron. The static electric field can be caused by the atomic nucleus, or related to the band or crystal structure of the solid. Below we will very briefly describe three main spin relaxation mechanisms for conducting electrons in metals and semiconductors.

- The Elliot-Yafet mechanism (EY) [36][37] (see figure 2.5a) originates from the fact that the lattice ions induce a local atomic electric field, the spin up and spin down states are mixed by spin-orbit coupling. The exact Bloch state (i.e. momentum eigenstate) is no longer a spin eigenstate but a superposition of them. This induces a finite probability for spin flip when the spatial part of the electron wave function experiences a transition through scattering even if the involved interaction is spin independent. The spin relaxation time is inversely proportional to the momentum scattering rate and if this scattering mechanism for momentum relaxation is dominant than the spin-flip length wil be linearly proportional to the mean free path.

- In III-V semiconductors, the degeneracy in the conduction band is lifted for $k \neq 0$ due to the absence of inversion symmetry. The resulting energy difference, for electrons with the same k but different spin states, plays the role of an effective magnetic field and results in spin precession with angular velocity $\omega(k)$ during the time between collisions. Since the magnitude and the direction of k changes in an uncontrolled way due to electron scattering with impurities and excitations, this process contributes to spin relaxation. The spin relaxation rate induced by this so called D'yakonov-Perel mechanism (DP) [38] (see figure 2.5b) will be inversely proportional on the momentum scattering rate, therefore the corresponding spin flip length is independent of the mean free path.

- The electron spin-flip transition is also made possible by the exchange interaction between electrons and holes. This is called the Bir-Aronov-Pikus mechanism (BAP) (see figure 2.5c), and is especially strong at low temperatures (<50 K) in semiconductors with a high overlap between the electron and free hole wavefunctions [39].

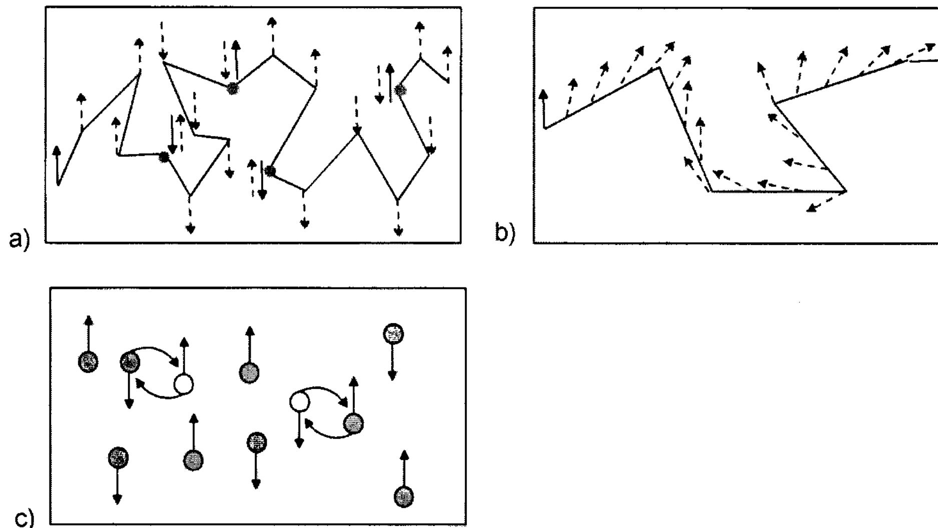

Figure 2.5: (a) The Elliot-Yafet mechanism. This mechanism is due to the interaction of the spins with the electric field of the nnuclei. (b) The D'Yakonov-Perel mechanism. In non-symmetric crystals, spin bands are no longer degenerate. The electron spin relaxation takes place as it randomly changes precession direction and frequency and is independent on the mean free path. (c) The Bir-Aronov-Pikus mechanism. The exchange interaction between electron and hole spins cause spin flip. An electron and hole flip their spin at the same time and therefore maintain their total quantum numbers.

Generally, electrons in semiconductors with specific doping retain their spin information much longer than holes (1 ns for electrons versus 1-100 ps for holes). One of the main reasons for the fast hole spin relaxation is that the orbital momentum carried by the hole allows an efficient exchange of the angular momentum with phonons. The total angular momentum has to be conserved. Through spin-orbit interaction the spin is coupled to the orbital momentum and therefore if the orbital momentum changes, the the spin will also be changed. Therefore electrons as information carriers are more used for spintronic applications.

For n-type semiconductors, the contribution of the BAP mechanism is negligible, since the equilibrium hole concentration is extremely small. In n-type GaAs neither EY nor DP processes depend explicitly on the doping concentration, but the temperature dependence often distinguishes between scattering processes. In n-type GaAs with doping concentrations in the range from 10^{16} cm^{-3} to 10^{18} cm^{-3} the DP mechanism is found to be dominant down to a temperature of 30 K, whereas below 5 K the EY mechanism dominates [40]. For moderate doping the spin lifetimes are extended significantly. Kikkawa and Awschalom [41] found for doping of 10^{16} cm^{-3} spin lifetimes from 10^3 ps at 100 K up to 10^5 ps at 5 K. Spin lifetimes of this order are necessary for our device as designed in chapter 3. The EY mechanism suppresses the spin lifetimes at high magnetic fields around 2 T and therefore this high magnetic fields could not be used in our experiments.

2.3 Spin polarized electron transport

To give the reader a global idea of the theoretical status in modelling spin polarized transport, first we give a brief historical overview and show how our work fits within this framework. The discovery of giant magnetoresistance effects has triggered a large number of studies on the transport properties of magnetic multilayers. For the geometry in which the current flows in the planes of the multilayers, classical [42, 43] and quantum [44] models have been worked

out. For the geometry in which the current flows perpendicular to plane of the multilayers, Lee *et al.* [45] proposed to explain the magnetoresistance by a two-current scheme with volume and interface resistances in series for each spin direction. Alternatively, Johnson and Silsbee [46] and independently van Son, van Kempen, and Wyder [47] introduced a concept based on spin dependent distribution functions to describe the spin transport through an interface between ferromagnetic an nonmagnetic conductors. Valet and Fert [48] extended the model in a Boltzmann equation formalism, which reduces to the same macroscopic transport equations found by Van Son *et al.*. If the mean free path is much shorter that the spin diffusion length, the macroscopic transport equations are recovered regardless the ratio between the layer thickness and the spin diffusion length. The formalism of Valet-Fert is extensively explained in section 2.3.2. Recently, the macroscopic transport equations were utilized to analyze the feasibility of spin injection into semiconductors, with the result that the crucial parameter is the impedance mismatch between the semiconductor and ferromagnet [12]. Yu and Flatté [49] studied the electric field effects on spin diffusion and injection in semiconductors. They started with the diffusion and the Poisson equation and include carrier concentration effects and treated the problem in terms of particle densities. Afterwards they switched to chemical potentials and neglected third order terms and higher. Their result was an extension of the macroscopic transport equations with an extra term containing the influence of the electric field. In section 2.3.3 we continue the work based on the Boltzmann formalism and show that if we do not neglect the influence of the electric field, we arrive to the same drift-diffusion equation as found by Yu and Flatté. In section 2.3.5 our macroscopic spin transport model will be applied to a ferromagnet- isolator- semiconductor- isolator- ferromagnet structure, schematically shown in figure 2.11. Alternatively in section 2.3.6 we discuss our model in the linear transport regime (resistor model) and it is mainly meant to give the reader some more physical insight into the physics of the spin valve device. Before we start describing the Boltzman formalism, we try to explain in the next section the physical picture behind spin injection and accumulation and introduce the fundamental quantities used in describing spin transport.

2.3.1 Spin injection and accumulation: the basic idea

Here the concept of spin injection and accumulation is introduced. If a current passes between a spin reservoir and a non-magnetic material an unbalance in spin-up and spin-down population out of thermal equilibrium may be created in the non-magnetic material. An external electric field can maintain this spin unbalance.

Let us consider a ferromagnet/ semiconductor contact, through which electric current is passed. As the conductivities for the spin-up and spin-down electrons in a ferromagnetic metal are unequal, the usual charge current ($J_\uparrow$+$J_\downarrow$) in the ferromagnet is accompanied by a spin current ($J_\uparrow$-$J_\downarrow$) transporting magnetization in the direction of the charge current. The conductance for the spin-up and spin-down electrons are equal in the non-magnetic semiconductor. As the net spin supply and drain at the two side of the contact are unequal, this leads the spin-up electrons to accumulate and the spin-down electrons to be depleted over a distance λ_f and λ_s, the spin diffusion lengths in the ferromagnet and semiconductor respectively. This local spin imbalance is equivalent to an induced magnetization (see figure 2.4). Even when the conductance in a semiconductor are the same, the total currents for each spin direction might be different, because it may have both a drift component (which is controlled by the conductance) and a diffusion component (controlled by the local spin density). In principle this would make a ferromagnetic metal an ideal candidate as an electrical source of spin currents for temperatures below the Curie temperatures. However, the ratio between the conductance of the ferromagnet and the conductance of the non-magnetic semiconductor is commonly unfavorable for spin injection. The physics is discussed in detail in section 2.3.5.

To overcome this so called impedance mismatch [12], an isolator layer may be inserted between the ferromagnet and semiconductor. Let us consider the system shown in figure 2.6,

a magnetic metal serving as a spin reservoir is coupled via a tunnel barrier to a non-magnetic semiconductor. A current J is flowing perpendicular to the F/I/SC interface. The tunnel barrier has different conductances for up and down spins and the spin relaxation during tunneling is negligible. Because of the spin polarization, the electric current crossing the tunnel barrier is also accompanied by a spin current. The advantage of inserting a tunnel barrier is that the tunnel barrier conductance may have the same order of magnitude as the conductance of the semiconductor.

Spin transport in this system has both a drift component (induced by the external electric field) and the diffusion component (induced by a variation by the local spin density). A simple approach would be to consider only one driving force, the gradient in the electrochemical potential. The presence of a net spin current leads to a difference in the electrochemical potential for the two spin directions. The induced magnetization is proportional to the difference in difference in electrochemical potential. Spin-flip processes lead to decay in the spin splitting of the chemical potentials away from the interface.

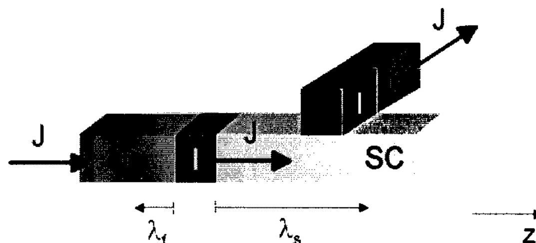

Figure 2.6: Schematic representation of the experimental layout for electrical spin injection. A current J is flowing through a F/I/SC system. The arrows indicated with λ_f and λ_s represent the distances where the spin accumulation exists in the ferromagnet and semiconductor. The spin accumulation can be probed by attaching a I/F voltage probe to SC within a distance λ_s from the I/SC interface.

Let us consider a second tunnel barrier towards a ferromagnet in close proximity to the injector tunnel barrier, so that the electrochemical potentials are still out of equilibrium in the semiconductor at the second SC/I/F interface. If the ferromagnet would be fully spin-polarized (only one spin direction is available at the Fermi level), it will only be sensitive to the electrochemical potential to the respective spin population. Flipping the magnetization of the second ferromagnet with respect to the first, makes it sensitive now to the minority spin direction. Therefore, this ferromagnet can be used to detect the presence of a spin imbalance. A real ferromagnet with a finite polarization would measure a weighted average of the two spin directions, its detection efficiency being proportional to the tunnel polarization of the barrier. Therefore, this contact can be still used to detect the presence of the spin accumulation.

2.3.2 Boltzmann equation model

Let us consider a one dimensional structure where a single domain ferromagnetic metal layer alternates with a nonmagnetic layer (see figure 2.7). A current density J flows parallel to the x axis and the magnetization of the ferromagnetic material is taken 'up' or 'down' along the x-axis, in this case the spin quantization axis. Because the magnetizations are all colinear, a

Figure 2.7: Schematic representation of the experimental layout for which the Boltzmann equation will be solved. A current J is flowing through a ferromagnetic-nonmagnetic system.

local velocity distribution function of the conduction electrons for the spin direction $\uparrow$, $f_\uparrow(x, v)$

is introduced. The analysis is confined to zero temperature, where for ferromagnetic metals the electron-magnon spin-flip scattering is absent and spin-flip scattering processes are through spin-orbit interactions mainly via the Elliot-Yafet mechanism. For semiconductors the spin relaxation mechanism EY, DP, BAP and their influence at certain temperatures are already described in section 2.2. The difference in spin-flip diffusion length in figure 2.6 is explained by the fact that the mean free path in metal is much smaller than in semiconductors. In addition, 3d electrons are generally stronger spin-orbit scatterers than s and p electrons. In a steady state the linearized Boltzmann equation determines that the changes in the distribution due to drift (particle transport), due to the applied field and due to particle collisions (momentum scattering) cancel each other. At any point (x, v) and for values $\downarrow$ and $\uparrow$, the net rate of change of $f_{(\uparrow)}(x, v)$ is zero;

$$v_x \frac{\partial f_\uparrow}{\partial x}(x,v) - eE(x) v_x \frac{\partial f_\uparrow}{\partial \epsilon}(v) = \int d^3v' Q_\uparrow(x, \epsilon(v))(f_\uparrow(x,v') - f_\uparrow(x,v)) + \int d^3v' Q_{sf}(x, \epsilon(v))(f_\downarrow(x,v') - f_\uparrow(x,v)) \quad (2.8)$$

where '$-e$' and $\epsilon(v) = \frac{1}{2}mv^2$ are respectively the charge and energy of the electrons and $E(x) = -\frac{\partial V}{\partial x}$. $Q_\uparrow(x, \epsilon)$ and $Q_{sf}(x, \epsilon)$ are the spin conserving and spin-flip transition probabilities, respectively. Assumed is that they are isotropic in space, so that $Q_{sf}(x, \epsilon)$ does not transfer momentum between the two channels, i.e. the spin flip chance to flip from spin-up to down equals the chance to flip from spin-down to spin-up.

A more extended non-analytical treatment in which electron-electron scattering is taken into account is given by Flensberg [50] and D'Amico [51]. However this is beyond the objective of our work and we only summarize briefly a few implications. The two spin species have different drift velocities and e-e interactions are in equilibrating, leading to a spin drag effect where the spins carrying the larger current will drag along the spins carrying smaller current. Therefore, if a spin-polarized current is driven through a the system, the spin drag will give rise to an additional resistivity, which increases with temperature. The spin drag resistivity can become considerable and even exceed the ordinary impurity scattering-induced resistivity.

When the steady state does not depart very far from equilibrium, a small perturbation to the Fermi-Dirac distribution is considered, i.e. a linear approximation:

$$f_{(\uparrow)}(x,v) = f^0(v) + \frac{\partial f^0}{\partial \epsilon}\left((\mu^0 - \mu_\uparrow(x)) + g_\uparrow(x,v)\right) \quad (2.9)$$

where $\mu_\uparrow(x)$, μ^0 is the chemical potential for spin up, respectively in equilibrium. The term between the brackets consists of an anisotropic part $(\partial f/\partial \epsilon) g_\uparrow(x, v)$ and a velocity independent isotropic term expressing the local variations of $\mu_\uparrow(x)$ in order to account for spin accumulation. In principle these two term could be expressed in one velocity dependent term. While developing this term in Legendre polynomials, we will identify the zeroth-order term with the deviation of the chemical potential from equilibrium. For clarity we have chosen to split off the isotropic term already now. Instead of directly solving equation (2.8) by substituting (2.9), a scattering time approximation is used for the righthand side. In expressing the relaxation of the spin accumulation, the perturbation to $f^0(v)$ is assumed to be inverse proportional to a scattering time $\tau_\uparrow$ and τ_{sf} for respectively the first and second term of the right hand side of equation 2.8. Now substitution of equation 2.9 in 2.8 and neglecting second and higher order terms we obtain:

$$v_x \frac{\partial g_\uparrow}{\partial x}(x,v) + \left(\frac{1}{\tau_s} + \frac{1}{\tau_{sf}}\right) g_\uparrow(x,v) = \left(v_x \frac{\partial \bar{\mu}_\uparrow}{\partial x}(x) + \frac{\bar{\mu}_\uparrow(x) - \bar{\mu}_\downarrow(x)}{\tau_{sf}}\right), \quad (2.10)$$

where $\bar{\mu}_\uparrow(x) = \mu_\uparrow(x) - eV(x)$ is the electrochemical potential for spin $\uparrow$. Through a cylindrical symmetry around the x-axis $g_\uparrow(x, v)$ can be developed in Legendre polynomials of $\cos\theta$, where

θ is the angle between the velocity and the x-axis:

$$g_\uparrow(x,v) = \sum_{n=1}^{\infty} g_\uparrow^{(n)}(x) P_n(\cos\theta) \tag{2.11}$$

where the zero-order (isotropic) term is absent since $(\partial f^0/\partial\epsilon) g_\uparrow(x,v)$ was defined by equation (2.9) as the anisotropic part of the electron distribution perturbation. The dependence in x and v can now be separated by putting equation (2.11) in equation (2.10) and projecting on the complete basis of Legendre polynomials, yielding an infinite chain of differential equations. Regarding that in the degenerated electron gas regime of a semiconductor and in metals, the Fermi-Dirac distribution is related to the electron velocity v_F at the Fermi surface as:

$$\frac{\partial f_0}{\partial \epsilon} = \frac{1}{mv}\frac{\partial f_0}{\partial v} = \frac{-\delta(v - v_F)}{m v_F} \tag{2.12}$$

it is found that

$$\cos\theta \sum_{n=1}^{\infty} \frac{\partial g_\uparrow^{(n)}}{\partial x}(\cos\theta) + \frac{1}{\lambda_\uparrow}\sum_{n=1}^{\infty} g_\uparrow^{(n)} P_n(\cos\theta) = \cos\theta \frac{\partial \bar{\mu}_\uparrow}{\partial x} + \frac{\bar{\mu}_\uparrow - \bar{\mu}_\downarrow}{v_F \tau_{sf}} \tag{2.13}$$

with $\lambda_\uparrow = v_F(1/\tau_\uparrow + 1/\tau_{sf})^{-1}$ the mean free path for spin-up and $v_x = v_F \cos\theta$. In order to solve equation (2.13), it can be projected on the Legendre polynomals of order $\tilde{n}$ as:

$$\sum_{n=1}^{\infty} \frac{\partial g_\uparrow^{n}}{\partial x} \int_{-1}^{1} du P_1(u) P_{\tilde{n}}(u) P_n(u) + \frac{1}{\lambda_\uparrow}\sum_{n=1}^{\infty} g_\uparrow^{(n)} \int_{-1}^{1} du P_{\tilde{n}}(u) P_n(u) =$$
$$\frac{\partial \bar{\mu}_\uparrow}{\partial x}\int_{-1}^{1} du P_1(u) P_{\tilde{n}}(u) + \frac{\bar{\mu}_\uparrow - \bar{\mu}_\downarrow}{v_F \tau_{sf}} \int_{-1}^{1} du P_{\tilde{n}}(u). \tag{2.14}$$

Using the orthogonality relation between Legendre polynomials

$$\int_{-1}^{1} du P_{\tilde{n}}(u) P_n(u) = \frac{2}{2n+1}\delta_{n,\tilde{n}}, \tag{2.15}$$

where $\delta_{\tilde{n},n}$ is the usual Kronecker delta every term except the first term in equation 2.14 can be calculated. For determining the first term in equation (2.14) the following recurrence formula is needed

$$P_1 P_n = \frac{(n+1)}{(2n+1)} P_{n+1} + \frac{n}{(2n+1)} P_{n-1}, \tag{2.16}$$

equation (2.14) leads to

$$\sum_{n=1}^{\infty} \frac{\partial g_\uparrow^{(n)}}{\partial x}\left(\frac{2(n+1)}{(2n+1)(2n+3)}\delta_{\tilde{n},n+1} + \frac{2n}{(2n+1)(2n-1)}\delta_{\tilde{n},n-1}\right) +$$
$$\frac{1}{\lambda_\uparrow}\sum_{n=1}^{\infty} g_\uparrow^{(n)} \frac{2}{(2n+1)}\delta_{\tilde{n},n} = \frac{2}{3}\frac{\partial \bar{\mu}_\uparrow}{\partial x}\delta_{\tilde{n},1} + 2\frac{\bar{\mu}_\uparrow - \bar{\mu}_\downarrow}{v_F \tau_{sf}}\delta_{\tilde{n},0}. \tag{2.17}$$

Determing the general expression (2.17) for given values of $\tilde{n}$, one obtains:

$$\begin{aligned}
\frac{\partial g_\uparrow^{(1)}}{\partial x} &= \lambda_\uparrow \frac{\bar{\mu}_\uparrow - \bar{\mu}_\downarrow}{l_\uparrow^2}, && \text{for} \quad \tilde{n} = 0, \\
\frac{2}{5}\frac{\partial g_\uparrow^{(2)}}{\partial x} - \frac{\partial \bar{\mu}_\uparrow}{\partial x} &= -\frac{g_\uparrow^{(1)}}{\lambda_\uparrow}, && \text{for} \quad \tilde{n} = 1, \\
\frac{\tilde{n}+1}{2\tilde{n}+3}\frac{\partial g_\uparrow^{(\tilde{n}+1)}}{\partial x} + \frac{\tilde{n}}{2\tilde{n}-1}\frac{\partial g_\uparrow^{(\tilde{n}-1)}}{\partial x} &= -\frac{g_\uparrow^{(\tilde{n})}}{\lambda_\uparrow}, && \text{for} \quad \tilde{n} > 1,
\end{aligned} \tag{2.18}$$

where it is defined that $D_\uparrow = \frac{1}{3} v_F \lambda_\uparrow$ [52], the spin diffusion constant for spin-up electrons. The factor $\frac{1}{3}$ is the result of a calculation of the average velocity in only one dimension. When the diffusion equation is solved, using the characteristic length scales for spin diffusion we obtain for the spin diffusion length $l_\uparrow = [D_\uparrow \tau_{sf}]^{1/2}$. For gaining a better understanding of the physical significance of equation (2.18) it is worthwhile to establish the exact relation between the current of spin-up $J_\uparrow$ and $g_\uparrow$. By definition of $g_\uparrow$, given by equation (2.9), the spin-up current reads:

$$J_\uparrow = -e \left(\frac{m}{h}\right)^3 \int d^3 v \frac{\partial f^0}{\partial \epsilon} g_\uparrow \mathbf{v} v_x, \tag{2.19}$$

where h is the Planck constant. Now changing to cylindrical coordinates and using the cylindrical symmetry of the system, equation (2.19) can be written with equation (2.12) as:

$$J_\uparrow = \frac{e}{m v_f} 2\pi \left(\frac{m v_f}{h}\right)^3 \int_{-1}^{1} du P_1(u) g_\uparrow(u). \tag{2.20}$$

From the development (2.11) in Legendre harmonics of $g_\uparrow$, using orthogonality relation (2.15), equation 2.20 immediately leads to

$$\int_{-1}^{1} du P_1 g_\uparrow(u) = \frac{2}{3} g_\uparrow^{(1)}. \tag{2.21}$$

Thus

$$J_\uparrow = \frac{\sigma_\uparrow}{e\lambda_\uparrow} g_\uparrow^{(1)}, \quad \text{with} \quad \sigma_\uparrow = \frac{n_\uparrow e^2 (1/\tau_\uparrow + 1/\tau_{sf})^{-1}}{m} \tag{2.22}$$

where and $n_\uparrow = \frac{4}{3}\pi (\frac{m v_f}{h})^3$ is the number of electrons with spin-up. So the system of equations is given by:

$$\begin{aligned}
\frac{e}{\sigma_\uparrow} \frac{\partial J_\uparrow}{x} &= \frac{\bar{\mu}_\uparrow - \bar{\mu}_\downarrow}{l_\uparrow^2}, \\
\frac{\partial \bar{\mu}_\uparrow}{\partial x} &= \frac{e}{\sigma_\uparrow} J_\uparrow + \frac{2}{5} \frac{\partial g_\uparrow^{(2)}}{\partial x}, \\
g_\uparrow^{(2)} + \frac{3}{7} \lambda_\uparrow \frac{\partial g_\uparrow^{(2)}}{\partial x} &= -\frac{2e\lambda_\uparrow^2}{3\sigma_\uparrow} \frac{\partial J_\uparrow}{\partial x}, \\
\frac{n}{2n-1} \lambda_\uparrow \frac{\partial g_\uparrow^{(n-1)}}{\partial x} + g_\uparrow^{(n)} + \frac{n+1}{2n+3} \lambda \uparrow \frac{\partial g_\uparrow^{(n+1)}}{\partial x} &= 0, \qquad \text{for} \quad n > 2,
\end{aligned} \tag{2.23}$$

which are the macroscopic transport equations in one dimension including spin relaxation. A formal solution of equation (2.23) can be given

$$g_\uparrow^{(n)}(x) = -\frac{2e\lambda_\uparrow}{3\sigma_\uparrow} \int_{-\infty}^{\infty} d\tilde{x} G_\uparrow^{(n)}(x, \tilde{x}) \left(\lambda_\uparrow(\tilde{x}) \frac{\partial J_\uparrow}{\partial \tilde{x}}\right), \tag{2.24}$$

where $G_\uparrow^{(n)}(x, \tilde{x})$ is the Green function of equation (2.23). Through the lack of translational invariance in the z direction, $G_\uparrow^{(n)}$ is explicitly dependent on both variables. Substituting equation (2.24) in equation (2.23) yields for the first two equations of 2.23:

$$\frac{e}{\sigma_\uparrow} \frac{\partial J_\uparrow}{\partial x} = \frac{\bar{\mu}_\uparrow - \bar{\mu}_\downarrow}{l_\uparrow^2}, \tag{2.25}$$

$$\frac{\partial \bar{\mu}_\uparrow}{\partial x}(x) = \frac{e}{\sigma_\uparrow(x)} \left[J_\uparrow(x) - \frac{4}{15} \lambda_\uparrow(x) \frac{\partial}{\partial x} \int_{-\infty}^{+\infty} d\tilde{x} G_\uparrow^{(2)}(x, \tilde{x}) \left[\lambda_\uparrow(\tilde{x}) \frac{\partial J_\uparrow}{\partial \tilde{x}} \right] \right]. \tag{2.26}$$

The terms in equation 2.23 for n≥1 are negligibly small and will be neglected. In the next section we will solve this set of two equations and discuss the limitations.

2.3.3 Macroscopic spin transport model

The 'Boltzmann correction', i.e. the second term at the right hand side of equation 2.26, beyond the macroscopic transport equations breaks the locality of the linear response relation between electrochemical potential gradient and the current. At a given point $\partial\bar{\mu}_\uparrow/\partial x$ no longer depends only on the current at the same point, but also on the current divergence integrated over a domain centered at this point and extending upon the decay length of $G_\uparrow^{(2)}(x,\tilde{x})$. The decay length of $G_\uparrow^{(2)}(x,\tilde{x})$ is a length of the order of the mean free path, because this is the unique scaling length of equation (2.23). Although equation (2.23) indicates current conservation, there still is a current divergence for spin-up, because of the spin relaxation mechanisms, taking place on a length scale of the spin diffusion length. So the term $\lambda_\uparrow(\partial J_\uparrow/\partial x)$ in equation (2.26) can be approximated for a layer of thickness t by $(t/l_{sf})(\lambda_\uparrow/l_{sf})J$ with $(1/l_{sf})^2 = (1/l_\uparrow)^2 + (1/l_\downarrow)^2$ [47]. The whole 'Boltzmann correction' is, independently of the thickness of the sample, proportional to $\lambda_\uparrow/l_{sf}$. In the limit of $\lambda_\uparrow/l_{sf} \ll 1$ equation (2.26) reduces to Ohm's law and equation (2.25) expresses that there is a balance in steady state between the spin accumulation related to the spin current divergences and spin-flip processes. This condition is reasonable fulfilled, at least at low temperatures and for moderate spin-orbit interaction, described in section 2.2, it follows that

$$\frac{\nabla\sigma_\uparrow}{\sigma_\uparrow}\nabla\bar{\mu}_\uparrow + \nabla^2\bar{\mu}_\uparrow = \frac{\bar{\mu}_\uparrow - \bar{\mu}_\downarrow}{D_\uparrow\tau_{sf}}, \tag{2.27}$$

We point out that this equation is restricted to the x direction. The coefficient of the first term can be found using:

$$\sigma_\uparrow = n_\uparrow e\nu_\uparrow. \tag{2.28}$$

The mobility through different scattering potentials is defined as:

$$\nu_\uparrow = e(1/\tau_\uparrow + 1/\tau_{sf})^{-1}/m. \tag{2.29}$$

Calculating the gradient of the number of up-spin electrons divided by the total number of electrons with spin-up

$$\frac{\nabla\sigma_\uparrow}{\sigma_\uparrow} = -\frac{\int_0^\infty N_\uparrow(\epsilon)\frac{\partial f^0}{\partial\epsilon}d\epsilon}{\int_0^\infty N_\uparrow(\epsilon)f^0 d\epsilon}\nabla(\bar{\mu}_\uparrow + eV), \tag{2.30}$$

with ϵ the energy measured from the bottom edge of the conduction band, $N(\epsilon)$ the density of states and f^0 the Fermi-Dirac distribution function.

All the analysis above are done for the spin up channel, but for the down-spin system similar equations can be easily obtained. For nonmagnetic materials $\nu_\uparrow = \nu_\downarrow = \nu$ and $D_\uparrow = D_\downarrow = D$ (equation 2.28, 2.29 and $D_\uparrow = \frac{\nu_\uparrow}{ekT}$) and for ferromagnetic materials, approximately the mobility and diffusion constant of the lower-conductivity spin species, usually the minority spins, are dominant $\nu \simeq \nu_\downarrow$ and $D \simeq D_\downarrow$ [53]. The first term in equation (2.27) will introduce an electric field and the question is, when the drift term is of the same order as the diffusive term. The characteristic length scale for the transport is the spin diffusion length. Therefore ∇ can be substituted by approximately $1/\sqrt{D\tau_{sf}})$. A critical field is now defined as

$$E_c \equiv \frac{1}{e\sqrt{D\tau_{sf}}}\left(-\frac{\int_0^\infty N(\epsilon)\frac{\partial f^0}{\partial\epsilon}d\epsilon}{\int_0^\infty N(\epsilon)f^0 d\epsilon}\right)^{-1}. \tag{2.31}$$

When the electric field exceeds the critical field, the electric-field effects can not be neglected anymore. In a three-dimensional system, $N(\epsilon) = A\epsilon^{1/2}$ and equation(2.30) can be calculated. For three temperatures E_c is plotted in figure 2.8 as a function of the electron density using a

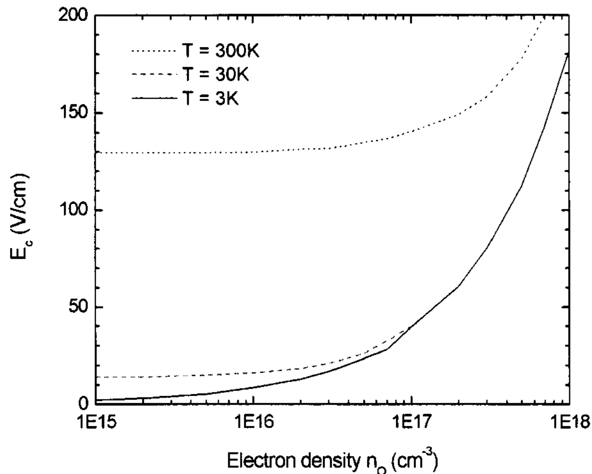

Figure 2.8: Critical field E_c as a function of the electron density for different temperatures in 3D systems. The effective electron mass is 0.067 m_0, where m_0 is the free electron mass.

typical spin diffusion length of 2 μm for GaAs [11]. The metal regime is characterized by a density of conducting electrons higher than $1 \cdot 10^{18}$ cm^{-3} and a critical field, which is nearly independent of the temperature. The drift term can be neglected, because the effective electric field is screened by the individual Coloumb fields of all the conducting electrons (like a nucleus is screened for impinging electrons by the electrons orbiting around the nucleus). The diffusion equation as introduced by Van Son [47] and Van Kempen [46] is recovered. However for lightly doped degenerate semiconductor spintronic devices, the critical field is much lower and a moderate electric field can already dominate the carrier motion [11] [54]. For temperatures up to room temperature more electrons are exited to the conduction band and higher values for the critical electric field are calculated. In chapter three we will use semiconductors with a n-doping in the order of $4 \cdot 10^{17}$ cm^{-3}. In this case the critical field is 80 V/cm, a realistic field under which the spintronic devices operate. Therefore we have to include the drift term in our calculations. At a measuring temperature of 4K, the Fermi energy exceeds the thermal energy and the system should be treated in the degenerated regime [55]. On the other hand, analytical solutions are preferred. Therfore we chose for the non-degenerate assumption in which f^0 has just a Boltzmann form $\sigma \sim e^{-\epsilon/k_B T}$, obtaining $\nabla\sigma_\uparrow/\sigma_\uparrow = \nabla(\bar{\mu}_\uparrow + eV)/k_b T$.

In absence of space charge, the total amount of electrons is balanced by a local hole concentration. In doped systems spin polarization is created without changing electrons or hole densities, and therefore we require conservation of the total number of particles,

$$\mu_\uparrow + \mu_\downarrow = 0. \tag{2.32}$$

Now subtracting both equations (2.27) for up-spin and down-spin electrons and filling in the equation above, a general drift-diffusion equation for up-spin polarization is deduced (for the down-spin channel similar equations can be found);

$$\begin{aligned} \nabla^2\bar{\mu}_\uparrow + \frac{eE}{kT}\nabla\bar{\mu}_\uparrow &= \frac{\bar{\mu}_\uparrow}{D\tau_{sf}} \\ \nabla^2\bar{\mu}_\downarrow + \frac{eE}{kT}\nabla\bar{\mu}_\downarrow &= \frac{\bar{\mu}_\downarrow}{D\tau_{sf}}. \end{aligned} \tag{2.33}$$

The general form of the steady state solution to equation 2.33 in a homogeneous medium, using

the requirement of current conservation, is given by

$$\bar{\mu}_{\uparrow} = A + Bx + \frac{C}{\sigma_{\uparrow}} exp(-x/\lambda_d) + \frac{D}{\sigma_{\uparrow}} \exp(x/\lambda_u) \tag{2.34}$$

$$\bar{\mu}_{\downarrow} = A + Bx - \frac{C}{\sigma_{\downarrow}} exp(-x/\lambda_d) - \frac{D}{\sigma_{\downarrow}} \exp(x/\lambda_u), \tag{2.35}$$

where the two quantities λ_d and λ_u are the up-stream and down-stream spin diffusion lengths [49], defined as

$$\lambda_d = \left(-\frac{eE}{2kT} + \sqrt{\left(\frac{eE}{2kT}\right)^2 + \frac{1}{\lambda_s^2}} \right)^{-1} \tag{2.36}$$

$$\lambda_u = \left(+\frac{eE}{2kT} + \sqrt{\left(\frac{eE}{2kT}\right)^2 + \frac{1}{\lambda_s^2}} \right)^{-1} \tag{2.37}$$

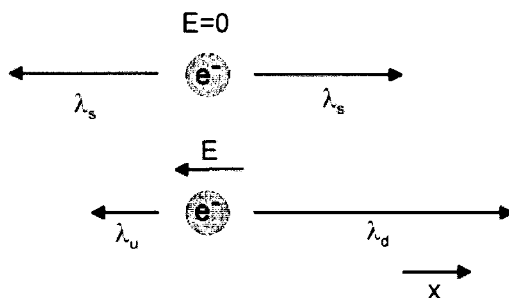

Figure 2.9: Schematic representation of the spin diffusion lengths in absence of an electric field and for an electric field directed in the negative x-direction.

For semiconductors in absence of an electric field or for metals, the up- and down-stream diffusion lengths converge to the intrinsic diffusion length $\lambda_s = \sqrt{D\tau_{sf}}$. As shown in figures 2.9 & 2.10, an applied electric field decreases the spin diffusion length of electrons moving in the direction of the electric field and increases the spin diffusion length of electrons moving opposite of the direction of the electric field. To understand the physical consequence of the electric field, we assume a spin is injected at $x = 0$ in the absence of an electrical field. In figure 2.10a the probability that spin can be found at position x is shown (assuming no spin flip takes place). The cumulative probability that the spins travel across a certain boundary is proportional to the diffusion constant D. By applying an electric field, spins follow both a drift motion v_{drift} in the electric field and a random walk diffusive motion (see figure 2.10b). The diffusion constant for upstream direction D_u is smaller than D and the diffusion constant for the downstream direction D_{down} is larger than D. The physics of the field effects on the spin diffusion becomes clearer at the strong-field limit, where the electrons move with the drift velocity and so does the spin polarization. λ_d is simply the distance over which the carriers move within the spin lifetime $\nu_e|E|\tau_{sf}$ and $\lambda_u = k_B T/|eE|$ [53].

2.3.4 Carrier density versus electrochemical potential

For non degenerate semiconductors, the particle density of up- and down-spin electrons is sometimes in the literature (e.g. Yu and Flatté [26]) a more familiar way to describe the spin unbalance. It is therefore useful to describe the connection between these two quantities and express the drift-diffusion equation in particle densities. For a Boltzmann distribution, the chemical potential is related to the carrier density, the electrons in the conduction band, via

$$n_{\uparrow(\downarrow)} = n^0_{\uparrow(\downarrow)} \left(\exp\left(\frac{\mu_{\uparrow(\downarrow)}}{kT}\right) - 1 \right) \tag{2.38}$$

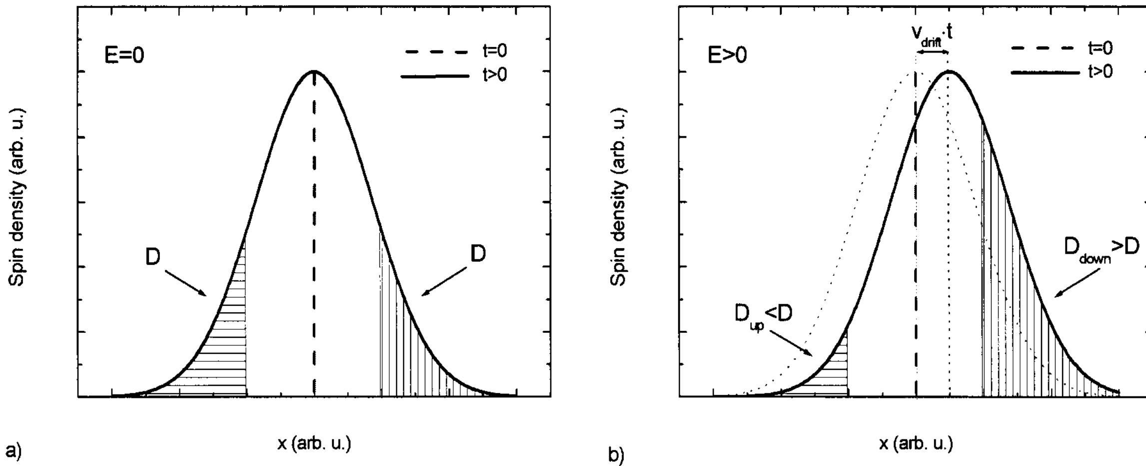

Figure 2.10: (a) The normalized probability to find the spin in position x at time t in absence of an electrical field. The originally injected spin population is a delta function for x=0, t=0. The probability to cross a certain section is proportional to the diffusion constant D. (b) Applying an electrical field, spins follow both a drift motion and a random diffusive walk. This leads to different upstream and downstream diffusion constants.

The drift-diffusion equation can be expressed in terms of $n_\uparrow - n_\downarrow$ by using equation 2.38 in equations 2.25 and 2.26. The established results will contain nonlinear terms, expressing the disadvantage of the use carrier densities. By means of the approximation of dropping all third and higher orde terms in the generalized series expanding of all logarithmic terms, the found differential equation is in agreement with the one earlier calculated by Yu and Flatté [26]

$$\nabla^2(n_\uparrow - n_\downarrow) + \frac{eE}{kT} \cdot \nabla(n_\uparrow - n_\downarrow) - \frac{n_\uparrow - n_\downarrow}{\lambda_s^2} = 0. \tag{2.39}$$

2.3.5 Magnetoresistance

We apply the macroscopic spin transport model to a ferromagnet/ tunnel barrier (insulator)/ semiconductor/ tunnel barrier (insulator)/ ferromagnet structure, schematically shown in figure 2.11. We consider two geometries. The first one, we denote as a vertical geometry (see figure 2.11a). The vertical geometry is simple to solve and describes correctly experimental devices as those of Mattana *et al.* [23]. The geometry shown in figure 2.11b corresponds to our envisioned experimental device for all electrical spin injection and detection in GaAs as described in chapter three. This so called lateral geometry differs slightly from the standard vertical geometry, due to the fact the GaAs channels extends to infinity in both direction. However, apart from being technologically simpler to make, a lateral device also allows four terminal measurements to be performed in different configurations. In the first one, to be addressed as the 'classic' configuration, the current is injected and taken out from the ferromagnetic electrodes. The voltage is measured between the same electrodes, giving a standard four terminal measurement. A second measurement geometry, which we refer to as the non-local measurement geometry, corresponds to injecting current from the normal channel into the first ferromagnetic electrode and measure the voltage between the second ferromagnetic electrode and the normal channel (see figure 2.17).

Vertical geometry

A lightly-doped semiconductor layer between $x = -L/2$ and $x = L/2$, for which the critical field E_c is lower than the operating electric field, separates two infinitely small tunnel barriers and two semi-infinite layers of the same ferromagnetic metal. A tunnel barrier is chosen for its high spin-dependent interface resistance effect, and therefore enhances the spin polarization of the injected current. In ballistic contacts the total spin-accumulation induced at the interface resistance is proportional to the minimum of either of both conductances over a distance of the spin flip length [25]. The conductance of a semiconductor is much lower than the conductance of a ferromagnetic metal so the spin dependent part of the interface resistance is negligible in relation to the spin independent part. This effect, known as 'conductivity mismatch' [12] is therefore not present. A second advantage of the use of tunnel barriers is that an injected electron has low probability to lose their spin information by escaping back into the ferromagnet. Finally, for for the conductance of the interface in the limit to infinity, one recovers the clean contact case. Therefore, we treat the most general problem possible.

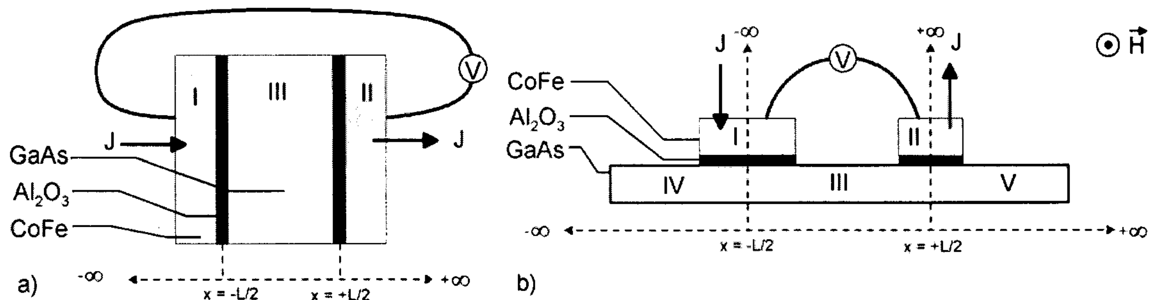

Figure 2.11: (a) vertical geometry) Cross section of the vertical spin valve device. (b) lateral geometry) Cross section of the lateral spin valve device. Regions I and II denote the injecting and detecting ferromagnetic contacts, each separated from the semiconductor channel (region II) by an isolating tunnel barrier. The origin is taken in middle of the channel, the arrows indicate the chosen direction of the positive x-coordinate. A spin polarized current is injected from region I into region III and detected at region II. Region IV and V represent the semi-infinite extension of the semiconductor.

The applied bias between the two current leads is the origin of an electric field E. We assume that the electric field is homogeneous through the whole device, and there is no linear current-voltage dependence of the tunnel barriers. The polarization of the tunneling conductance is assumed to be independent of the voltage drop over the barriers. In reality, the magnon-assisted conductance will increase for higher bias voltage [56, 57]. Thus, the resistance change between parallel and anti-parallel magnetization orientations wil also decrease for higher bias voltage over the tunnel barriers. The bias dependence also an intrinsic component has via the underlying electronic structure . Two effects must be considered, that the Fermi level of one electrode is shifted relative to the other and that the barrier shape is altered at finite bias. Shifting of the chemical potential allows new states to be accessed for tunnelling, essentially making the spin polarization a voltage-dependent quantity. And second, through a modified barrier form, higher energy states tunnel also more easily [58]. Considering these effects, we overestimate P for high bias. Three different regions, marked with roman letters are identified, corresponding in also three forms of solutions of the drift-diffusion equation for each spin state. These six equations are given by eqn. 2.34. Assuming current is injected in region I and extracted in region III, and that voltage is measured between regions I and III and parallel magnetization of

the ferromagnetic regions, leads to

$$\begin{aligned} I: \mu_{\uparrow(\downarrow)} &= A + \frac{Je}{\sigma_f}x \pm \frac{B}{\sigma_{1\uparrow(\downarrow)}}\exp(x/\lambda_f) \\ II: \mu_{\uparrow(\downarrow)} &= C + \frac{Je}{\sigma_f}x \pm \frac{D}{\sigma_{2\uparrow(\downarrow)}}\exp(-x/\lambda_f) \\ III: \mu_{\uparrow(\downarrow)} &= \frac{Je}{\sigma_s}x \pm \frac{2F}{\sigma_s}\exp(-x/\lambda_d) \pm \frac{2G}{\sigma_s}\exp(x/\lambda_u) \end{aligned} \tag{2.40}$$

where we have written for the total conductivity of the ferromagnet $\sigma_f = \sigma_{1(2)f} = \sigma_{1(2)\uparrow} + \sigma_{1(2)\downarrow}$ and for the total current density $J = J_\uparrow + J_\downarrow$. In equation $\sigma_{1(2)\uparrow(\downarrow)}$ stands for the conductivity of the injector (detector) ferromagnet in region I (II) for the spin-up and spin-down, respectively. σ_s stands for the conductivity of the semiconductor, and A to G are six independent unknown constants. For regions I and II, the exponential term which increases for $x \rightarrow \pm\infty$, respectively, is omitted. The equations for the spin-down electrons can be found by putting a minus sign in front of constants B, D, F and G and adjusting the conductivity. The average potential at the middle of the semiconductor is set to zero. The lineair term in equations 2.40 is imposed because at $\pm\infty$ the solutions for the chemical potentials must coincide with the standard bulk dependence ($\mu_\uparrow|_{x\rightarrow\pm\infty} = \mu_\downarrow|_{x\rightarrow\pm\infty} = constant + Je/\sigma \cdot x$) (see equation 2.26). The tunnel current through the Al_2O_3 can be approximated for low bias-voltages ($V_b \ll 2\bar{\phi}/e$) to be voltage-independent (see equation 2.3). If no spin-flip scattering at the interface with the tunnel barrier is present, the first boundary condition at the interfaces is the discontinuity of $\mu_\uparrow$ and $\mu_\downarrow$ associated with the existence of spin-selective interface resistances $G_{1\uparrow(\downarrow)}$ and $G_{2\uparrow(\downarrow)}$ (analogy with equation 2.26), that is: [28].

$$\mu_{\uparrow(\downarrow)}(x = -L/2^-) - \mu_{\uparrow(\downarrow)}(x = -L/2^+) = G_{1\uparrow(\downarrow)}J_{\uparrow(\downarrow)}(x = -L/2) \tag{2.41}$$

$$\mu_{\uparrow(\downarrow)}(x = L/2^-) - \mu_{\uparrow(\downarrow)}(x = L/2^+) = G_{2\uparrow(\downarrow)}J_{\uparrow(\downarrow)}(x = L/2), \tag{2.42}$$

where $J_{\uparrow(\downarrow)}$ can be found from (2.26). Secondly there is continuity of the derivative of the chemical potential or in other words, the current density in each spin channel is conserved. We assume that no spin flip processes at the interface take place:

$$J_{\uparrow(\downarrow)}(x = -L/2^-) = J_{\uparrow(\downarrow)}(x = -L/2^+) \tag{2.43}$$

$$J_{\uparrow(\downarrow)}(x = L/2^-) = J_{\uparrow(\downarrow)}(x = L/2^+) \tag{2.44}$$

(analogy with equation 2.25). Again the current passing through the interface is given by (2.26). In total there are eight equations; two conditions for both two regions, one for each spin state. The unknown parameters can now be computed and the spatial dependence of the two spin potentials are determined relative to the equilibrium chemical potential (figure 2.12). As we pointed out in §2.3.1, there will be a negligible small spin splitting at the interface of CoFe with Al_2O_3. However the tunnel barrier serves as a spin filter due to the spin dependence of the tunnel resistance and therefore a larger spin unbalance is created in the GaAs. Owing to spin-flip processes, the spin imbalance decreases exponentially on a length scale λ_s. Another CoFe in combination with a tunnel barrier is used to detect the spin unbalance. Note that the same direction of spin quantization axes throughout the system is used. For parallel magnetization, the slopes of the electrochemical potentials in the semiconductor are different for both spin orientations. They cross in the middle between the contacts. Because the conductivity of both spin channels is equal, this results in a spin polarization of the current in the semiconductor, which is positive and high near the tunnel barriers and positive, but low in the middle. Changing the magnetization orientation of one ferromagnetic electrode relative to the other, the axis of spin quantization is also changed. Tunnelling between corresponding spin states at the detection tunnel barrier now means tunnelling from a majority to a minority band and vice versa. This implies that for the antiparallel calculation $G_{2\uparrow}$ should be exchanged for $G_{2\downarrow}$ and $\sigma_\uparrow$

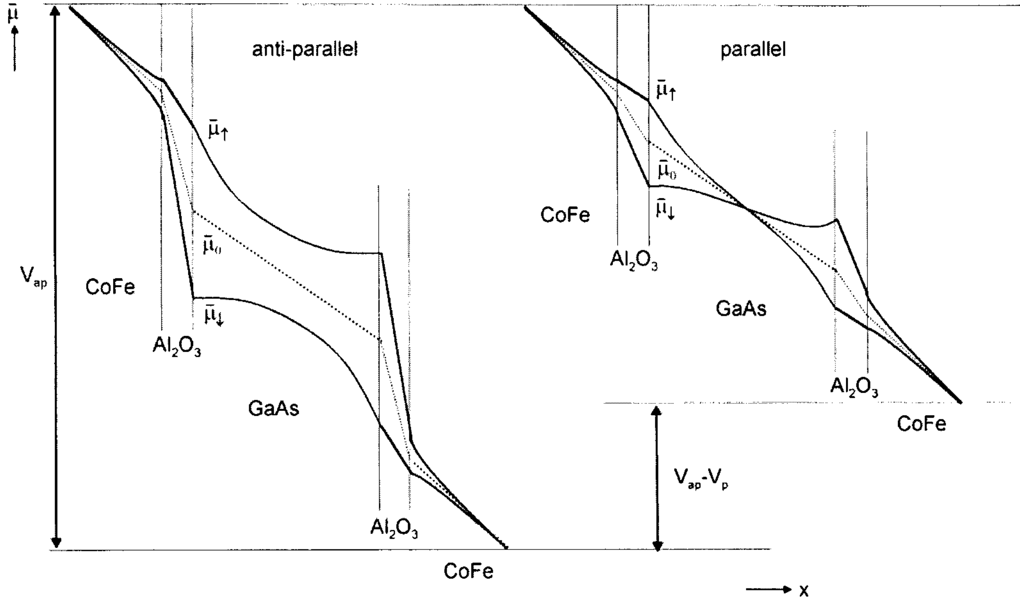

Figure 2.12: Spatial dependence of the spin-up and spin-down electrochemical potentials (solid) for a device consisting of a semiconductor with two isolator/ferromagnetic contacts for parallel and anti-parallel magnetization of the ferromagnets. The dashed lines indicate the equilibrium electrochemical potential (voltage). The electric field is set zero in this picture. The relative value of spin splitting in different regions is not drawn to scale.

for $\sigma_\downarrow$. In the antiparallel case the the spin polarization current is in the semiconductor near the injection tunnel barrier positive and high. In the middle of the semiconductor the slopes of the electrochemical potential are equal, resulting in unpolarized current flow. Near the extraction tunnel barrier the spin polarization current is again high but now negative. The most important constants are A and C, giving directly the difference between the electrochemical potentials at both ferromagnetic ends. The difference in antiparallel and parallel resistance now reads:

$$R_{ap} - R_p = \frac{V_{ap} - V_p}{J} =$$

$$\frac{4\sigma_s(Q1-)(Q2-)(\frac{1}{\lambda_u} + \frac{1}{\lambda_d})\cosh(\frac{L}{2}(\frac{1}{\lambda_u} + \frac{1}{\lambda_d}))}{\left[4 + \frac{\sigma_s}{\lambda_d}(Q1+)\right]\left[4 + \frac{\sigma_s}{\lambda_u}(Q2+)\right]\exp(\frac{L}{2}(\frac{1}{\lambda_u} + \frac{1}{\lambda_d})) - \left[4 - \frac{\sigma_s}{\lambda_u}(Q1+)\right]\left[4 - \frac{\sigma_s}{\lambda_d}(Q2+)\right]\exp(-\frac{L}{2}(\frac{1}{\lambda_u} + \frac{1}{\lambda_d}))}$$

$$\text{with} \quad Q1(2)\pm = ((\frac{1}{\sigma_{1(2)\uparrow}} \pm \frac{1}{\sigma_{1(2)\downarrow}})\lambda_f + (G_{1(2)\uparrow} \pm G_{1(2)\downarrow})). \tag{2.45}$$

Reducing this equation to measurable quantities we will introduce a number of new quantities. First, $\sigma_s = 1/\rho^*$, with ρ^* the resistivity of the semiconductor. A K-factor $K = \lambda_s/L$ is defined as the ratio between the spin diffusion length and the length of the semiconductor channel, being equivalent to the layer thickness in this structure. Further we define the square resistance of the semiconductor as $rch = \rho^* \cdot L$ and the interface resistances as $G_{1\uparrow(\downarrow)} = 2rtb1/(1 + (-)P)$ and $G_{2\uparrow(\downarrow)} = 2rtb2/(1 + (-)P)$, with $rtb1$ and $rtb2$ the spin independent square resistances of the tunnel barriers and P the polarization at the interface. In order to shorten the equation a factor M is assigned to the ratio of the potential energy, due to an electrical field over a length of the characteristic diffusion length, compared to the thermal energy, $M = \mid eE \mid /kT$. This reflects the importance of the drift term over the diffusive part of the drift-diffusion equation.

The magnetoresistance is generally defined as the difference in resistance between parallel and antiparallel magnetization, normalized by the antiparallel resistance, $((R_{ap} - R_p)/(R_{ap}))$. With this definition, it is impossible to give a compact state expression for the magnetoresistance. Therefore instead of normalizing by the parallel resistance an approximation is made to normalize by the total resistance in case no spin unbalance is present $(rtb1 + rch + rtb2)$. The magnetoresistance calculated from our definition is below 1% from the MR obtained with the standard definition.

In ferromagnets the spin flip length is several orders of magnitude shorter than in a semiconductor and for both spin states its characteristic resistance is much smaller than the interface resistances:

$$G_{1\uparrow(\downarrow)} \gg \frac{\lambda_f}{\sigma_{1\uparrow(\downarrow)}} \tag{2.46}$$

$$G_{2\uparrow(\downarrow)} \gg \frac{\lambda_f}{\sigma_{2\uparrow(\downarrow)}}. \tag{2.47}$$

Therefore, we may neglect the dependence of bulk ferromagnet properties. In this limit and changed to our measurable quantities, we come to a magnetoresistance for a vertical device (see figure 2.11):

$$\begin{aligned} MR_{vertical} &= \frac{R_{ap} - R_p}{rtb1 + rch + rtb2} = \\ &\frac{\frac{4P^2 rtb1 rtb2 \left(M^2+4\right)^{(1/2)} cosh\left(\frac{M}{2K}\right)}{Krch(1-P^2)^2 (rtb1+rtb2+rch)}}{-\left[Q2-\right]\left[Q1-\right]\exp\left(-\frac{(M^2+4)^{1/2}}{2K}\right) + \left[Q2+\right]\left[Q1+\right]\exp\left(\frac{(M^2+4)^{1/2}}{2K}\right)} \\ \text{with} \quad Q1\pm &= \left[1 + \frac{rtb1\left(-M/2 \pm \sqrt{(M/2)^2+1}\right)}{(1-P^2)\,Krch}\right] \\ \text{with} \quad Q2\pm &= \left[1 + \frac{rtb1\left(+M/2 \pm \sqrt{(M/2)^2+1}\right)}{(1-P^2)\,Krch}\right]. \end{aligned} \tag{2.48}$$

As a direct important result, for small polarization the MR is related to the polarization via approximately P^2, corresponding the simple diffusive model of van Son et al. [47]. rch only depends of the properties of the material and will be together with $P = 0.4$ (a standard spin valve result [30]) a fixed design parameter for the following analysis. In fact both resistance times area products of the tunnel barriers are rated to rch, so it is preferable to work with ratios normalized to the channel resistance. Leaving the electric field out of consideration, the device properties are fully symmetric and injection and detection sides can be interchanged. In fig. 2.13a, the MR value is calculated as a function of the ratio between the tunnel barrier resistance and the resistance of the GaAs, where was set $rtb1 = rtb2 = rtb$, $K = 5$ and $M = 0$. For small rtb/rch and $\lambda_s \gg L$ the discontinuities in the electrochemical potential ($\mu_\uparrow$ and $\mu_\downarrow$) introduced by the interface resistances are too small to generate a high enough splitting in the semiconductor (in comparison with the splitting in the ferromagnet) and polarize the current. As mentioned earlier, this phenomenon is called the resistivity mismatch. In the region near the maximum magnetoresistance the predominant contribution to the variation of electrochemical potential comes from the potential drops at the interface. In the antiparallel configuration, this gives rise to a splitting which is negligibly relaxed by the spin flips in the GaAs since the number of spin flips is much too small in comparison with J/e. The upper limit of rtb/rch for the high K regime is clear. At constant spin lifetime in the semiconductor and constant current, on increasing rtb, the rise of the spin splitting saturates. However, the voltage drop over device still increases and the magnetoresistance drops down to zero. In figure 2.13b, the MR is plotted as

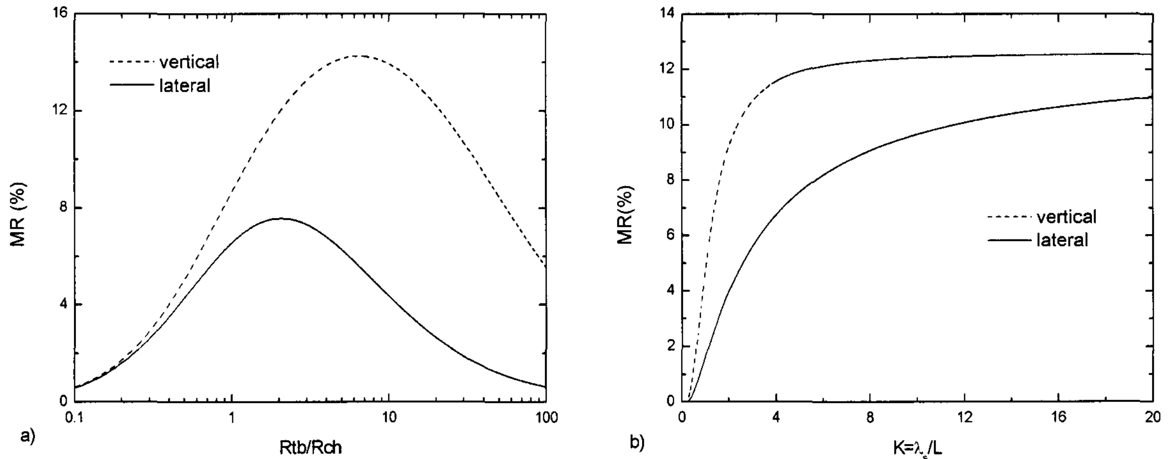

Figure 2.13: (a) Magneto resistance versus tunnel barrier resistance normalized at the resistance of the semiconductor channel for a vertical and lateral F/I/SC/I/F structure, where P=0.4, λ_s/L=5, M=0 and $Rtb1$ = $Rtb2$ = Rtb. (b) Magneto resistance as function of the ratio between the spin diffusion length and semiconductor channel, again for a vertical and lateral structure, where P=0.4, M=0 and $Rtb1/Rch = Rtb2/Rch = 2$. The geometries of the structures are shown in figure 2.11).

a function of K for a realistic set of parameters $(rtb1/rch = rtb2/rch = 2, M = 0)$. $1/K$ can be interpreted as the rate of spatial decay of the spin accumulation in the diffusion direction. For high rates, we expect a MR to approach zero, because of a lack of spin splitting. This is indeed observed in figure 2.13b. For semiconductor transport channels much smaller as the diffusion length, in combination with optimized resistances for the barriers (i.e. Rtb$\rightarrow \infty$), the MR goes to $P^2/(1-P^2))$. This maximum magnetoresistance is the fundamental limit. If we are able to measure this magnetoresistance dependence on the channel length, we have proved the observed magnetoresistance was caused by the presence of spin accumulation in a semiconductor.

Lateral geometry: 'classic' measurement geometry

Another geometry we considered, is a lateral F/I/SC/I/F structure in which the semiconductor layer spreads from $-\infty$ to ∞ as can be seen from figure 2.11b. At positions $(x = -L/2)$ and $(x = L/2)$ on the semiconductor two ferromagnetic electrodes are placed, separated from the semiconductor via a tunnel barrier. Because the width of the semiconductor channel is about hundred times larger than the length, deviations due to non-straight current paths influencing the effective spin diffusion lengths are negligibly. Therefore, the current is considered to be flowing homogeneously through the device. We assume that the width of the electrodes are negligible small compared to the channel length, and therefore, the current is injected at only one point in the semiconductor. The system is modelled as one-dimensional. The conditions and equations for regions I, II and III can be treated analogously to the vertical structure, however for regions IV and V for $x = \pm\infty$ the total current of both spin channels must be zero [59];

$$IV : \mu_{\uparrow(\downarrow)} = K \pm \frac{2M}{\sigma_s} exp(x/\lambda_s) \tag{2.49}$$

$$V : \mu_{\uparrow(\downarrow)} = N \pm \frac{2O}{\sigma_s} exp(-x/\lambda_s). \tag{2.50}$$

The five equations for the chemical potentials can be solved with boundary conditions analogously obtained as for the vertical structure (equations 2.41 and 2.43). Additionally, continuity

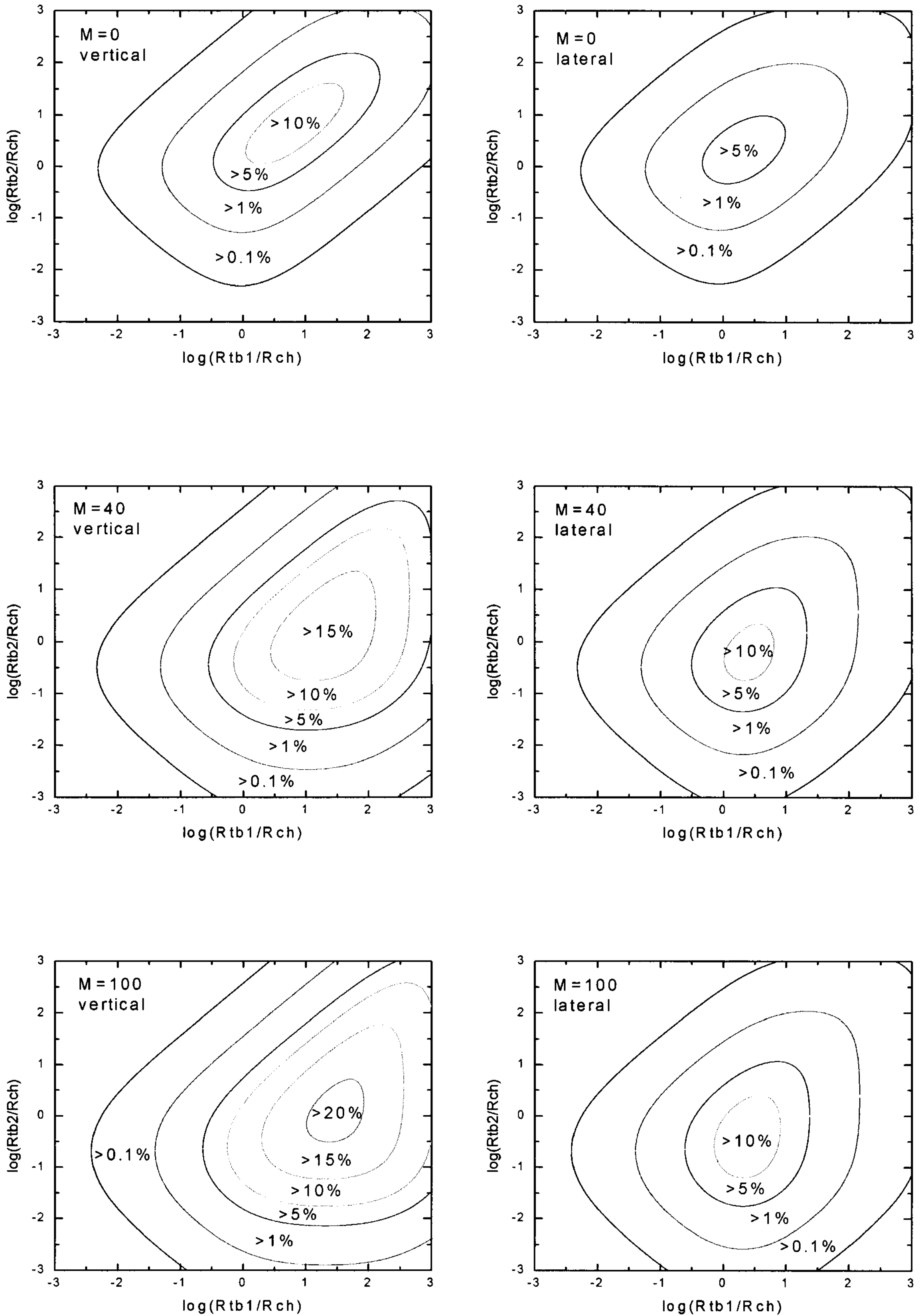

Figure 2.14: Contour plots of the magneto resistance versus the injecting and detecting tunnel barrier resistances normalized at the resistance of the semiconductor channel. The MR is calculated for a vertical and a lateral F/I/SC/I/SC structures for an increasing electric field (M=0, 40, 100). P=0.4, λ_s/L=5

is assumed of spin-up and -down chemical potentials and continuity of spin-up and -down currents between the two semiconductor regions at the injection and the detection point. The magnetoresistance for the lateral device then reads:

$$MR_{lateral} = \frac{\frac{4P^2 rtb1 rtb2}{Krch(1-P^2)^2(rtb1+rch+rtb2)}(M^2+4)^{1/2}\cosh(\frac{M}{2K})}{[Q1+]\,[Q2+]\,exp(\frac{(M^2+4)^{1/2}}{2K}) - [Q1-]\,[Q2-]\,exp(-\frac{(M^2+4)^{1/2}}{2K})} \tag{2.51}$$

$$\text{with} \quad Q1\pm = \left[\frac{rtb1}{rch(1-P^2)K}\left(1-\frac{M}{2}\pm\sqrt{\left(\frac{M}{2}\right)^2+1}\right)+1\right]$$

$$\text{with} \quad Q2\pm = \left[\frac{rtb2}{rch(1-P^2)K}\left(1+\frac{M}{2}\pm\sqrt{\left(\frac{M}{2}\right)^2+1}\right)+1\right]$$

As seen in figure 2.13b the MR signal of the lateral device is always smaller than of the vertical structure. Now a significant MR is only restored in a relatively small range of rtb/rch. Again, conductivity mismatch takes place for low rtb/rch ratios and for larger rtb/rch ratios, the splitting of the electrochemical potential in the anti-parallel state saturates, while the voltage drop increases. At too high resistances the detector efficiency also decreases for the lateral geometry, because more spin current is dissipated in the semiconductor regions IV and V, with less resistance. This is the cause of the very fast suppression of the MR. Obviously, figure 2.13b shows that the spin valve effect in a lateral has exactly the same MR asymptotic value as in a vertical device. Much larger K values are required to reach it's maximum, because of extension of spin accumulation over the spin diffusion length on both sides of the channel. Let us estimate reasonable ranges for K and spin flip length for our device. A spin diffusion length of $\approx$2 μm is calculated with $\lambda_s = \sqrt{k_B T \tau_{sf} \mu / 2e}$ [60] for a spin lifetime of 80 ns given in reference [41]. Due to e-beam lithography restrictions (L >100 nm), the range of the horizontal axis ($K = \lambda_s/L$) for the lateral device has to be limited to around 20.

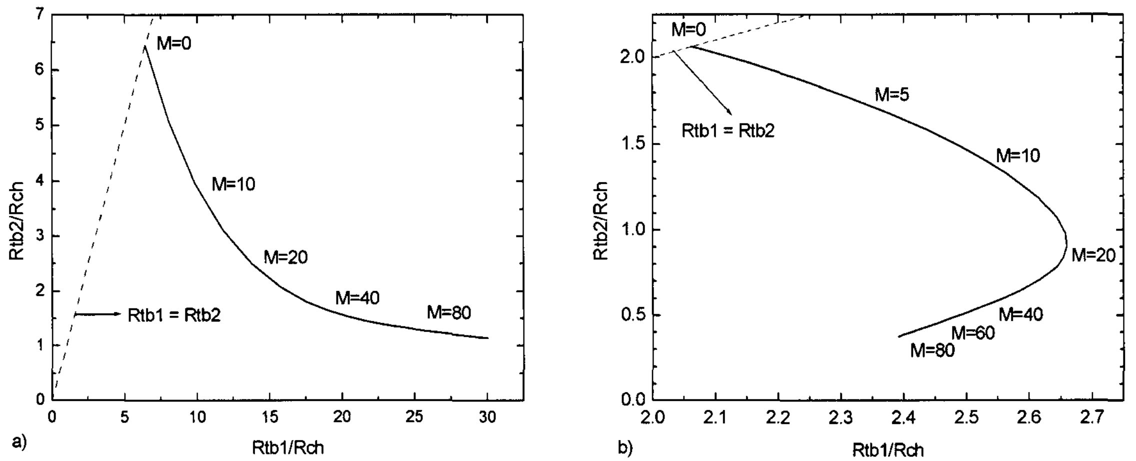

Figure 2.15: Optimization for the largest magnetoresistance as function of the injection and detection tunnel barrier normalized at the resistance of the semiconductor channel for different electric fields E (represented by $M = e \mid E \mid /kT$), for P=0.4 and λ_s/L=5. (a) vertical F/I/SC/I/SC structure; (b) lateral F/I/SC/I/SC structure.

Applying an electric field, can enhance spin diffusion dramatically [49]. A high field in contrast to a low-field creates a preferable drift direction between up-spin and down-spin electrons. The imbalance in the chemical potential has a similar sign as the spin polarization of the current,

where they can be quite distinct for low-field. For $M = e \mid E \mid /kT$=0, M = 40 and M = 80, figure 2.14 gives a contourplot of the dependence of the magnetoresistance on both barrier resistances. When an electric field is applied, we observe that the $rtb1$ and $rtb2$ ranges in which the MR could be detected increases. The measurement geometry is no longer symmetric and the maximum MR shifts. As long as the resistance of the detection tunnel barrier is larger than the resistance of the injection tunnel barrier, the MR increases monotonously with increasing M.

In figure 2.15a, we calculated for a vertical geometry for each value of the electric field, the optimum value of each tunnel barrier resistance, that optimize the MR for given channel parameters. For a small electric field, the device has reversal symmetry, and the injection and detection sides can be interchanged. Therefore the optimum corresponds to $rtb1 = rtb2$. As the electrical field increases, the absolute value of the optimum injection barrier resistance ($rtb1$) increases, and the absolute value of the optimum detection barrier resistance ($rtb2$) decreases. This is a consequence of the fact that the upstream and downstream spin diffusion lengths start to differ ($\lambda_u < \lambda_s < \lambda_d$). As the injection barrier should match downstream spin diffusion ($rtb1 \sim 1/\lambda_d$) and the detector barrier the upstream diffusion ($rtb2 \sim 1/\lambda_u$), optimum barrier values start to diverge.

Again, we calculated for a lateral geometry for each value of the electric field as shown in figure 2.15b the optimum value of each tunnel barrier resistance, that optimize the MR for given channel parameters. The optimum injection barrier resistance ($rtb1$) increases and the optimum detection barrier resistance ($rtb2$) decrease for increasing electric fields up to $M = 20$ ($P = 0.4, K = 5$). For larger electric fields $M > 20$ the optimum injection (detection) barrier resistance slowly drops towards the asymptotic value 2.4 (0.4). The reason that the optimum barrier resistance of the detector becomes small in the high field regime, is that the influence on spin transport in the semiconductor is localized within the up-stream length λ_u from the tunnel barrier resistance. λ_u decreases with increasing field and would become much shorter than L. Matching of both resistances in according to $rtb1rtb2/rch^2 \approx 1$ leads to a maximum in $rtb1/rch$. When the optimum injector barrier resistance no longer increases, the benefits of extra injection is balanced by the drawbacks of less detection, an optimum is found. Finally, when the spin-down length comes to the same value of the semiconductor channel, further rise of M hardly effects the spin valve effect and the optimum resistances do not change anymore.

If we compare the the optimum in the limit of zero M for the lateral and vertical geometries, the both resistances are also equal but more than three time higher, this is consistent with the volume of the semiconductor transport channel.

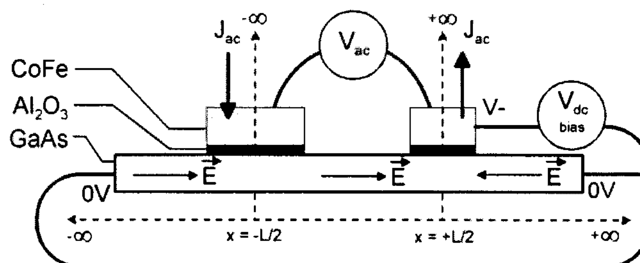

Figure 2.16: Cross section of the lateral spin valve device in the local measurement geometry with an extra dc bias voltage between the detector ferromagnet and the two extensions of the semiconductor. A spin polarized current is injected from region I into region III and detected at region II.

Lateral geometry: measurement geometry with both dc & ac voltages

In this last part of this section we will discuss two different measuring techniques. The much lower magnetoresistance value obtained in the lateral geometry compared to the vertical one stem from the extra spin flip processes in the two semiconductor areas (region IV and V). Moreover, the MR improvements induced by the electric field are quenched in the lateral geometry due to the lack of electric fields in the two areas (regions IV and V). Here we will show that by making use of both a dc bias and ac measurement techniques, improved MR ratio can also be obtained. We apply a dc bias voltage on the detector electrode, while putting the two arms to ground (see figure 2.16). The electric field produced by the applied bias, which sets the current is much smaller than the dc bias voltage. The electric field is pointed inwards in both semiconductor arms (regions IV and V) and pointed to the detector electrode in the semiconductor transport channel (region III). In order to distinguish the spin dependent voltage signal from the dc bias voltage ac measurement techniques has to be used. Large spin currents in the infinite GaAs arms (regions IV and V), which results in a large amount of spin flips, are now avoided, because drift in those regions will be minimal due to an opposite electric field. Therefore relatively large detection spin currents and small spin currents in the semiconductor extensions will enhance the MR. Substituting λ_u for λ_s in equations 2.49 corresponds to

$$MR_{bias} = \frac{\frac{4P^2 rtb1 rtb2}{Krch(1-P^2)^2(rtb1+rch+rtb2)}(M^2+4)^{1/2}\cosh(\frac{M}{2K})}{[Q1]\,[Q2]\,exp(\frac{(M^2+4)^{1/2}}{2K}) - [Q3]\,exp(-\frac{(M^2+4)^{1/2}}{2K})} \tag{2.52}$$

$$\text{with} \quad Q1 = \left[\frac{rtb1}{rch(1-P^2)K}(-M+\sqrt{4+M^2})+1\right]$$

$$\text{with} \quad Q2 = \left[\frac{rtb2}{rch(1-P^2)K}(\sqrt{(4+M^2})+1\right]$$

$$\text{with} \quad Q3 = \left[\frac{rtb1}{rch(1-P^2)K}(-M)+1\right]$$

If the electric field goes to infinite, the magnetoresistance converges to values found for vertical devices. The opposite electric fields in regions IV and V are so strong that any current is absent and the current-layout of the vertical device is recovered. From equation 2.52 ($rtb1/rch = rtb2/rch = 2, K = 5$) at $M = 40$ they are already within 5%. For $M \to \infty$ and $K \to \infty$ the MR_{bias} is proportional to the maximum obtained for vertical devices, i.e.:

$$MR_{bias} = \frac{2P^2}{1-P^2}\frac{rtb1}{rch+rtb1+rtb2} \tag{2.53}$$

The scaling factor is the ratio of the injection tunnel barrier over the total resistance. This once again indicates the importance of the spin injection in non symmetrical devices. For high values of $rtb1$ and $rtb2$, MR_{bias} equals $MR_{vertical}$.

Lateral geometry: nonlocal measurement geometry

The above described conventional local measuring geometry suffers from relatively large background resistances as compared to the spin valve resistance. Parts of the ferromagnetic electrodes are included in this background resistance, which can give rise to AMR contributions. Moreover a net current and stray magnetic fields are present in the semiconductor channel, which can lead to Hall effects. To remove these effects and to ensure only a voltage drop is measured due to spin accumulation in the semiconductor, the spin valve effect can be measured in the 'non-local' geometry [25]. The current is sent from contact area I to IV and the voltage is measured between area II and V (figure 2.17). Any form of (magneto)resistance due to the current injecting contact electrode is not relevant, because any voltage drop across it will not influence the current that is sent through it and similarly, no current flows through the ferromagnetic voltage detection

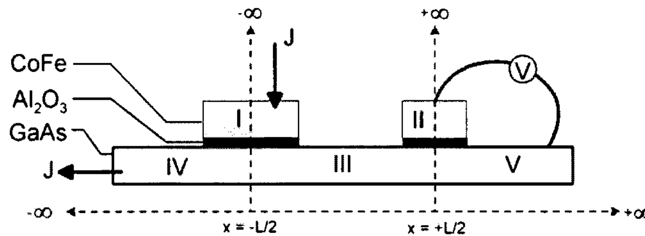

Figure 2.17: Cross section of the lateral spin valve device in the nonlocal measurement geometry. A ferromagnetic spin injector is separated from the semiconductor by an insolating tunnel barrier. A second electrode is used to detect the spin accumulation at distance L from the injector.

contact so its (magneto)resistance does not effect the voltage measurement. In order to obtain an expression for $(R_{ap}\text{-}R_p)/(rtb1 + rch + rtb2)$, the drift-diffusion equation has to be solved for each region with boundary conditions eq. 2.41 and 2.43. Similar solutions as equations 2.40 and 2.49 are found except the solutions for region I and IV contains a linear terms, and the solutions for regions II, III and V lacking the linear term, because in in that region there is no net current. After recalculation, for (M=0) the expected spin dependent voltage signal in the non-local geometry is found to be half of MR=$(R_{ap}\text{-}R_p)/(rtb1 + rch + rtb2)$ in the classic geometry.

2.3.6 Resistor model

To gain some more physical insight in the working of the spin valve device, we consider an equivalent resistor network (see figure 2.18) [45, 61]. This model is an approximation of the macroscopic model (section 2.3.3) in the lineair transport regime where the measured voltages are linear functions of the applied currents. The main assumption is that in the used materials the interactions between the two spin populations are weak, or in other words the spin lifetime is larger than the momentum relaxation time. An independent series of resistances can be attributed to each spin population, leading to a spin-up channel and a spin-down channel. If this does not hold an extra spin-mixing resistance needs to be introduced.

The current is injected from a ferromagnet and the spin-up will face a different bulk ferromagnet resistance as spin-down, reflected by $R_{F\uparrow}$ and $R_{F\downarrow}$. The interaction between the two spin populations is relatively strong, therefore the spin flip length is very short and both spin species are at the interface nearly at the same potential. We assume that tunneling is spin conserving, consequently the tunnel barriers can be modelled as to different conductances for each spin channel given by: $R_{tb\uparrow(\downarrow)} \sim 1/N_{\uparrow(\downarrow)}(E_F) \sim 2R_{tb}/(1-(+)P)$, with N the density of states at the Fermi energy and P the polarization (see section 2.1.2). The tunnel barrier resistances $R_{tb\uparrow}$ and $R_{tb\downarrow}$ are different for both channels and the difference is of the order of $k\Omega$. Because the difference in ferromagnet resistances for both spins populations is at least six orders smaller, the ferromagnet resistances are negligible in our model. A semiconductor wire of length L much smaller than the spin diffusion length λ_s ($L \ll \lambda_s$) can be modelled, in the second order approximation in (L/λ_s) by the equivalent resistor network shown in figure 2.18 for region III [62]. In the semiconductor the spin information is conserved over a spin diffusion length λ_s. The resistance for both spin species are equal in a semiconductor, but the spin flips cause the potential between the two spin channels to reduce away of the injection point, reflected by resistances $8R_{sc}(\lambda_s/L)^2$ connecting the two channels. Analogous, the semi-infinite GaAs arms (regions IV and V) with a length W, which act as an extra spin flip channel is than equivalent

(for $W \gg \lambda_s$) with a resistance $2R_{sc}(\lambda_s/W)$ for each spin channel.

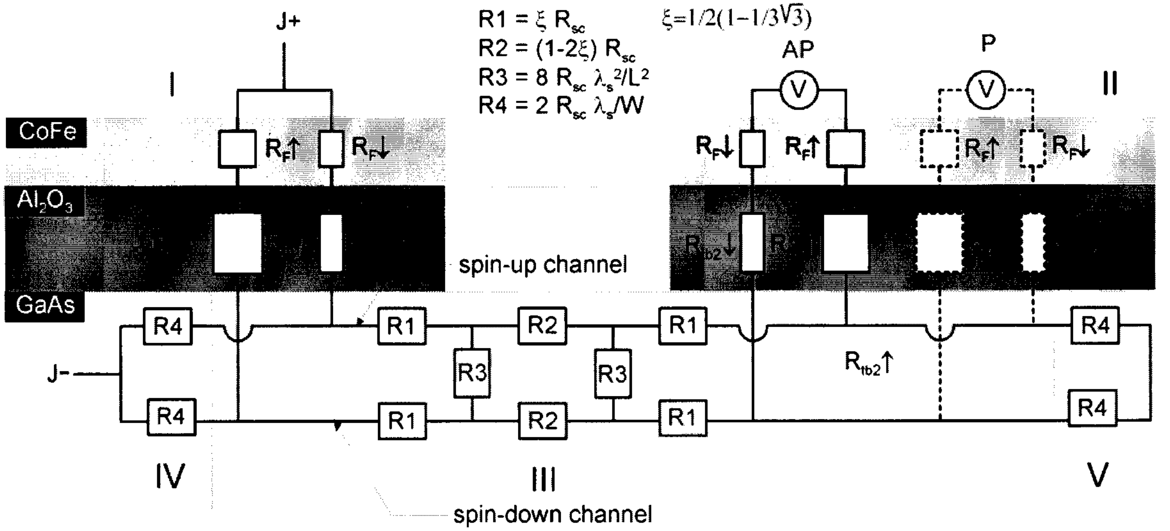

Figure 2.18: Resistor model of a fully electrical semiconductor-based spin valve device. $R_{F\uparrow(\downarrow)}$, $R_{tb\uparrow(\downarrow)}$ denotes respectively the resistance of the ferromagnet and the tunnel barrier for spin-up and spin-down electrons. R1, R2, R3, R4 are fractions of the semiconductor resistivity. The shown model is given for the non local measurement lateral geometry for anti-parallel alignment (solid line) and parallel alignment (dashed line), but can be easily adapted to other structures and geometries.

The current and voltage contacts are indicated for the non-local geometry. In the regions (I, IV and the left tunnel barrier), where net current is flowing, the total current in both channels has to be the same in each region (current conservation). In the other regions there is no net charge current, because spin up and down current are opposite. The current distribution over the two spin channels is mainly determined by $(R_{tb1} + R4)/(R_{tb2} + R4)$ in the limit $R3 \gg R4 (L \ll \lambda_s)$. A difference in potential $\Delta\mu_{(x=0)}$ arises underneath the injector. At $x = L$ the difference in potential is decayed with a ratio λ_s/L to a value $\Delta\mu_{(x=L)}$. The detector measures a weighted average of the spin up and spin down electrochemical potentials. The magnetization configuration determines for which spin channel the detector is most sensitive. The measured detector potential is $(1 + P)\Delta\mu_{(x=L)}/2$ and $(1 - P)\Delta\mu_{(x=L)}/2$ for parallel and antiparallel configuration. For a non negligible electric field, the resistances $R3$ and $R4$ in the two semiconductor are no longer equal for both current directions. Additional diodes have to ensure different resistances for different current directions. The model is easily adapted for a vertical or a local measurement.

The above described resistor model holds the best for tunnel barrier resistances much larger then the channel resistance or if the spin lifetime is smaller then the length of the semiconductor transport channel. In our measurement regime ($Rtb_{\uparrow(\downarrow)} \approx R_{sc}$, λ_s/L=5) the same trends as in figures 2.13 are observed, but values of maximum 20% larger were found.

In figure 2.18, the semiconductor transport channel is treated as an infinitesimal segment, correct up to the second order in $(L/\lambda_s)^2$. Let us consider the most simplest resistor model, where the semiconductor is modelled by a first order approximation. The spin flip resistance $R3$ is proportional to $\lambda_s^2/(\sigma \cdot V)$, and $R2$ scales with $L^2/(\sigma \cdot V)$, where σ is the bulk conductivity and V the volume of the semiconductor channel. For $L \ll \lambda_s$, $R2 \ll R3$ and the middle loop in the semiconductor channel can be substituted for a single resistance $R3/2$ (note that $R1$ has to be adjusted). For a vertical device, the whole resistor model reduces now to a Wheatstone bridge. In the parallel magnetization alignment, the products of resistances of opposite arms are equal. Therefore, the voltage drop over the spin flip resistance $R3$ is zero and no net spin current is present in the semiconductor. However, in the anti-parallel alignment, a finite voltage drop over the spin flip resistance leads to a current between the spin up and spin down channel.

Calculation of the voltage drop between region I and II shows that is the anti-parallel device resistance is larger than the parallel device resistance. Therefore, the presence of polarized currents can be detected.

Chapter 3

Towards electrical detection of spin accumulation in GaAs

3.1 Design requirements

In this section our design for the fully electrical GaAs-based spin valve device is discussed in detail. Basically the structure requires a ferromagnetic source and drain, one is serving as a spin injector and the other as spin detector, and a semiconductor in between, functioning as a transport medium. In order to show the spin valve effect, the device should meet the following requirements:

- In order to preserve spin information over distances as long as possible, high mobility and high spin life time are desirable in the semiconductor channel. Therefore epitaxially grown GaAs heterostructures are the best solution. In order to be able to make use of 'standard' epitaxially grown GaAs, we propose a lateral geometry, analog to experiments on all metal systems [24] (see fig. 3.1). Two ferromagnetic electrodes are placed on top of a GaAs wafer in order to measure a spin dependent voltage signal. The separation between the electrodes (L) should be smaller than the spin diffusion length of GaAs (λ_{sf}) , that is:

$$L <\sim \lambda_{sf}. \tag{3.1}$$

- A high spin injection and spin detection efficiency is necessary, as the expected signal in the first order is proportional to the product of these two. At the first place, a high tunneling spin polarization of the combination ferromagnet/tunnel barrier is necessary, because the magnetoresistance is for low spin-polarization approximately proportional to the square of the spin-polarization (2.51). Secondly, a basic obstacle of direct spin injection in semiconductors from ferromagnetic metals is that the degree of spin-polarization of the current in the purely diffusive regime is limited to less than 0.1% [13]. The change in device resistance for parallel and antiparallel magnetization of the contact is much smaller than 0.1%, and thus is difficult to detect (see equation 2.51). The solution to overcome this impedance mismatch problem was given by Rashba [14]. He proposed to use tunnel contacts of which the resistance R_{tb} is of the same order as the resistance of the GaAs R_{GaAs} over a spin relaxation length (see detailed calculations in section 2.3.5), that is:

$$R_{electrodes} \ll R_{tb} \propto R_{GaAs}. \tag{3.2}$$

  Furthermore, a uniform current density in the semiconductor requires a homogenous injection and detection through the tunnel barrier. Therefore, the resistance of the wire ($R_{electrodes}$) (see equation 3.2) should be much smaller than the resistance of the tunnel barrier.

- The magnetic properties of the injector and detector electrodes have to be separately controlled with one applied magnetic field. Parallel and anti-parallel magnetization directions of the micro-magnets have to be realized (see section 2.3.5). The solution is different coercive fields H_c of the electrodes:

$$H_{c1} \neq H_{c2}, \tag{3.3}$$

leading to different hysteretic behavior of the magnetization of the electrodes (see figure 1.1d to be discussed in detail in section 3.2.1). The ferromagnetic electrodes should be single domain over the region where current is injected in the semiconductor. Multiple domains would mean injection and detection of both spin components, reducing the efficiency.

3.2 Device layout and characteristic dimensions

The envisioned device is shown in figure 3.1. It consists of a GaAs substrate, with on top respectively a GaAs buffer layer, an $Al_{0.3}Ga_{0.7}As$ layer, a n-doped GaAs layer and finally a n^{++}-GaAs layer. On top of this wafer a uniform aluminium layer is grown, which is naturally oxidized. A channel is defined by covering the rest of the sample by insulating SiO_2, followed by deposition of the tantalum bonding pads. Two CoFe electrodes of different width cross the channel and are in electrical contact with the bonding pads. In the next subsections we will shortly discuss the temperature effects of the most important quantities. Subsequently, we discuss in full detail the device layout, characteristic dimensions and technical limitations of the different parts of our envisioned device. Next, we give dimensions for which a measurable magnetoresistance should be obtained and check if we have satisfied the requirements given in previous section. Finally, the compatibility with existing equipment is described.

Temperature effects

Estimations for spin lifetime $\sim 1/T^{3/2}$, mobility $\sim 1/T^{x}$ and resistivity $\sim \exp(\epsilon_g/kT)$ in GaAs are based on a working temperature of our device of 5K. Device functioning at 300K would be put much stronger constraints on device dimensions. In addition the magnetization and polarization of the ferromagnetic electrodes at the interface CoFe/AlOx/GaAs will decrease with increasing temperature, i.e. $M(T) = M(0)(1 - \alpha T^{3/2})$, for low (T/T_c), with T_C the Curie-temperature. The current opinion is generally that both intrinsic (e.g., band effects) and extrinsic (inelastic processes like thermal excitation of spin waves) contributions are the cause.

Tunnel barrier

The exponential dependence of the tunnel resistance on the barrier thickness makes that the resistances of tunnel junctions can be chosen in an extremely broad range and adapted to various geometry types. Aluminium oxide as a tunnel barrier material is particulary easy from fabrication point of view and it has proven itself as a reliable barrier over many years in tunneling experiments [63]. The barrier resistance should not become too high in order to limit the voltage drop over the barrier as such barriers break down at bias voltages typically around 1-2 Volt [30]. Our choice was a thickness of 1.5 nm. After oxidation the thickness will increase with 25%, so we obtain an Al_2O_3 barrier of around 1.85 nm thick. The expected resistance times area product, based on results on all metal junctions [30], should be of the order of magnitude of 100 $k\Omega \cdot \mu m^2$. We expect that our experimental obtained value will be lower than the value obtained for metallic junctions, because GaAs has a lower density of states.

Ferromagnetic electrodes

The dimensions of the ferromagnetic electrodes has to be such that the single-domain state is more stable than the multidomain state [64]. The latter regime is obtained for electrode widths

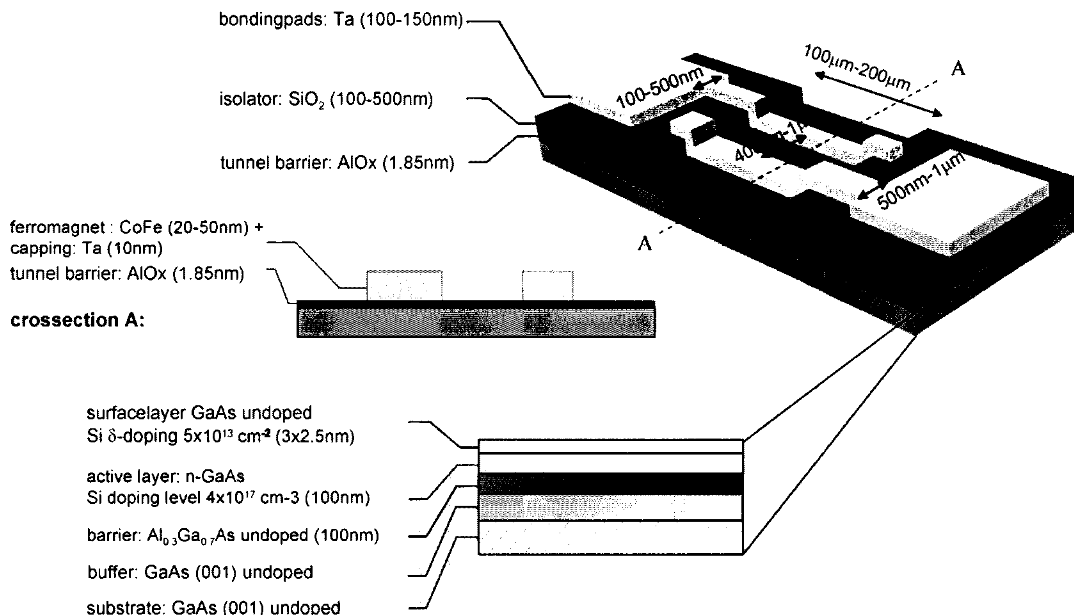

Figure 3.1: Schematic overview of a fully electrical semiconductor-based spin valve device. Dimensions are not drawn to scale. On top of a semiconductor wafer with a uniform Alox layer, two ferromagnetic electrodes of different width are placed. The enlargement shows the stack of layers of which the semiconductor wafer consists. The wiring pads are electrically isolated from the environment.

below 1 μm. Because the two ferromagnetic electrodes must be deposited simultaneously, they are made of the same material, with the same crystalline anisotropy. In addition, at sizes below a few hundred nanometer shape anisotropy is most important. Therefore we chose to control the magnetization via shape anisotropy (a phenomenon that will be explained in more detail in section 3.2.1). The electrodes should have a different width. By sweeping the external field from positive to negative values an vice versa both alignments can be achieved. For magnetization alignment, the electrodes should have a well defined easy-axis (=aspect ratios length/width>4). In section 3.2.1 we will explain magnetization reversal in more detail. For a good definition of the channel length, the width of the electrodes has to be much smaller than, or at least comparable with the channel length. The wires are fabricated with e-beam lithography, a technique which is explained in § 3.3.3. Due to technical limitations of e-beam lithography it is difficult to fabricate wires smaller than 100 nm and two separate electrodes can not become closer than 100 nm.

In addition the spin polarization has to be as high as possible, because the magnetoresistance is for low spin polarization approximately proportional to the square of the spin-polarization of the ferromagnets (equation 2.51). DC sputtered $Co_{90}Fe_{10}$ is stable on Al_2O_3, it has a spin polarizaton of over 50% [30] and a resistivity of $7.5 \cdot 10^{-8}$ Ωm.

GaAs channel

The intrinsic properties of the n-doped GaAs transport channel need to be well defined. The transport channel consists of three layers, namely an i-$Al_{0.3}Ga_{0.7}As$, a n-GaAs and a n^{++}-GaAs layer.

- **Schottky barrier suppression.** Between the n-doped GaAs and the Al_2O_3 a Schottky barrier is formed (see section 2.1.2). Taboryski *et al.* [65] demonstrated that the contact resistance due to this Schottky barrier is reduced from about $1 \cdot 10^{-7}$ Ωm^2 to $0.5 \cdot 10^{-10}$ Ωm^2,

for a high doping in the outermost top layer in their experiments. A 200 nm $4.4 \cdot 10^{18}$ cm^{-3} n-doped GaAs layer was capped with 5 δ-doped layers separated by 25 Å of undoped GaAs. Each of the δ-doped layers contained $5 \cdot 10^{13}$ cm^{-2} Si atoms and they quoted an increase of their carrier concentration in the active layer of only 25%. Using equation 2.1 we calculate that for the same amount of δ-doping one δ-doping layer is necessary at a depth of 2.24 nm. In case of overcompensation (see section GaAs/metal interfaces and Schottky barrier formation), our device would be operating in a regime where the tunnel barrier resistance heavily exceeds the resistance of the resistance of the GaAs channel (figure 2.13) and the MR will be almost undetectable. According to Taboryski, overcompensation has only a slight impact on the carrier concentration in the active layer. Therefore we choose only for three δ-doping layers spaced at 2.5 nm and keep it overcompensated. If the Schottky barrier turned out to be undercompensated, a wide Schottky barrier in combination with a tunnel barrier would be the result. This leads to a negligible tunnel current at low bias (i.e. the impedance mismatch regime) and no feedback from the measurement could be obtained. The n^{++}-GaAs layer is intended to suppress the Schottky barrier formed at the GaAs/ AlOx interface (see section 2.1.2). In the next paragraph, we will discuss the outlook and characteristic numbers of this layer in full detail.

- **Barrier.** In GaAs/ $Al_{0.3}Ga_{0.7}As$ the Γ minimum is the lowest in the conduction band throughout the structure and it is reasonable to neglect the higher bands. The energy level of the conduction band in $Al_{0.3}Ga_{0.7}As$ is 0.33 eV higher than in GaAs. Therefore, 100 nm $Al_{0.3}Ga_{0.7}As$ acts as an impenetrable barrier, provided that the energy of the electrons perpendicular to the barrier is well below the top of the barrier. $Al_{0.3}Ga_{0.7}As$ is chosen because the lattice constant is nearly identical to GaAs. By engineering the conduction band, the electrons are prevented to penetrate too deep in the semiconductor and thus take a longer path, that is deeper inside the GaAs, to the other electrode. A straight path ensures a well defined channel length and minimal spin flips, leading to a higher spin accumulation underneath the detection electrode.

- **Active layer.** The n-GaAs is the active layer, wherein a spin polarized current will be obtained. Maximum spin flip lifetime is obtained in optical measurements by Awschalom *et al.* [41] for an effective carrier concentration of $1 \cdot 10^{16}$ cm^{-3}. An active layer with this critical, relative low doping concentration in combination with the requirement of suppression of the Schottky barrier is difficult to make. Under- or overcompensation of the surface states due to a standard deviation of the n^{++}-GaAs layer, is of the same order. Therefore, our choice was for a doping concentration of $4 \cdot 10^{17}$ cm^{-3}. The mobility is estimated at an order of magnitude of $1.3 \cdot 10^{3}$ cm^2/V·s [65] and the spin life time is estimated at about 80 ns [41]. A thickness of 100 nm is chosen for the active n-doped layer. But through formation of a Schottky barrier at the interface of n-GaAs and $Al_{0.3}Ga_{0.7}As$ the effective depth is expected to decrease to 50 nm (see equation 2.1 and figure 2.1). The conductance of the GaAs channel is given by equation 2.28 and we estimate a square resistance in the order of 2 kΩ.

Dimensions and expected signal

All three conditions of section 3.1 have to be fulfilled and the structure dimensions have to remain technologically feasible. For electrode dimensions (width/length/height) of (100 nm-500 nm/ 100 μm-200 μm/ 20 nm-50 nm) and (500 nm-1000 nm/ 100 μm-200 μm/ 20 nm-50 nm) spaced at 400 nm up to 1000 nm (depending on the width of the electrodes), the magnetoresistance is expected to be measurable.

- A spin diffusion length of $\approx$1.5 μm was estimated based on $\lambda_s = \sqrt{k_B T \tau_{sf} / 2ne^2\rho^*}$ [60] for a spin lifetime of 80 ns given in reference [41]. Therefore, the length of the GaAs transport

channel is smaller then the spin flip length and the first requirement (equation 3.1) is fulfilled.

- With the above mentioned dimensions, we expect for the resistance of the tunnel barriers a value between 1 kΩ and 10 kΩ, for the resistance of the electrode a value of about 100 Ω-1 kΩ and for the resistance of the GaAs transport channel a value between 10 Ω and 100 Ω. Through the presence of the Schottky suppression layer the contact resistance is estimated less then 1 Ω. In conclusion, we fulfill the second condition (equation 3.2).

- The third condition (equation 3.3) is satisfied, because the electrode width is smaller then the typical width for which the single domain state is more stable then the multidomain state. Because the electrodes have a different width, and due to shape anisotropy, the coercive fields (10 mT-100 mT) will be different (see section 3.2.1).

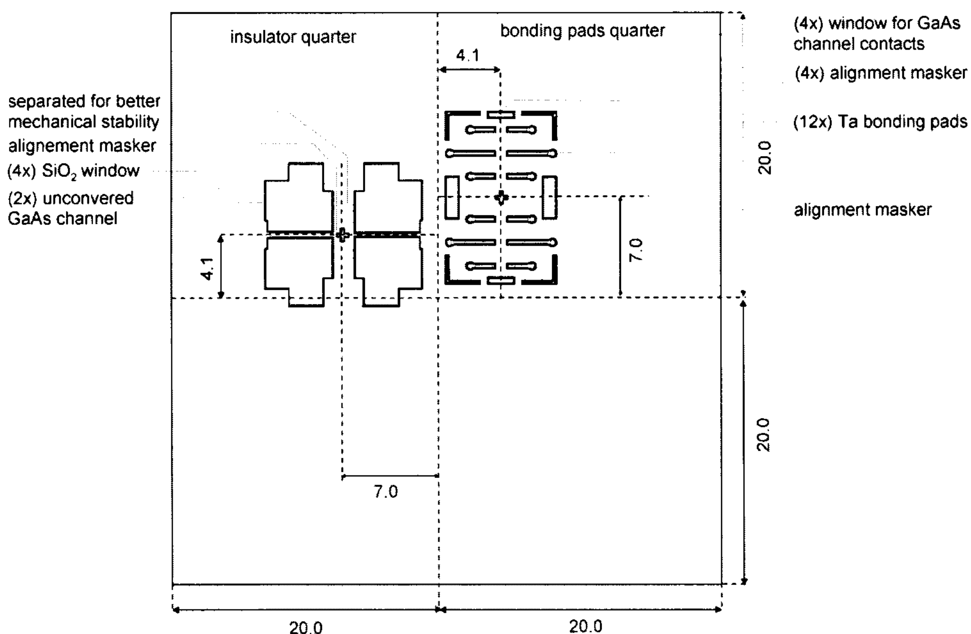

Figure 3.2: Top view of the mask layout, which is used for sputtering the Ta bonding pads (first quarter) and the SiO_2 isolation (second quarter. The mask is rotated 90° in situ (overlay accuracy ≈ 50 μm) and the two layers can be deposited on top of each other.

Compatibility with existing equipment

Sending current through the electrodes requires contacts with external wiring, via large bonding pads. The bonding pads have to be made of a metal, which is stable in air and is available at that moment in our sputter facility, i.e. Ta. Because the ferromagnetic electrodes are deposited a few days later on top of the electrodes, we might choose to use gold for the bonding pads in order to optimize the electrical contacts with the electrodes. The minimum distance between two, with one shadow mask, sputtered wires has to be at least 0.1 mm to obtain well-shaped, non-contacting wires. We chose for a separation of 1.5 mm between the bonding pads in order to have enough working space to make by hand low ohmic contacts with silverpaint. Large contact area would imply high probability of tunneling. So to prevent direct currents between two bonding pads and thus no current will flow through the small electrodes, the bonding pads have to be insulated from the tunnel barrier/ semiconductor substrate. The aspect ratio at the edge should be low to ensure that a deposited layer over the edge remains in contact. We chose for SiO_2 in combination with a shadow mask. The maximum size of a sample is limited by

the sizes of the flow cryostat and by the sample holder (12 mm×14 mm) (see appendix figure 5.4). The envisioned mask is shown in figure 3.2 and in more detail in appendix figure 5.1 and 5.2 in the appendix. It consists of a flat 0.5 mm thick molybdenum (fast degassing, resistant against high temperatures and extremely strong and stiff) plate with in the second quarter four (almost) squares and a cross marking the center of the sample. Between two insulation surfaces a channel as small as possible is defined. The insulation surfaces are separated for better mechanical stability and on each SiO_2 surface fits three bonding pads. The technical limitation of depositing this specific structure with a shadow mask is 0.1 mm, therefore we chose for a channel width of respectively 0.1 mm and 0.2 mm. The first quadrant contains six times two lines for sputtering the large bonding pads, four rectangles for external wire bonding, four corners for position localization during Secondary Electron Microscopy and a cross marking at the center of the sample. The sputter machine enables to turn the mask exactly 90 degrees, and the insulator and bonding pads quadrant are aligned on top of each other within 50 μm. The mean free path of the sputtered particles is much smaller than the distance between source and substrate at typically used Ar pressures. The flux arriving at the substrate does no arrive at a normal incidence angle. This requires that the mask is fully in contact with the substrate interface, obtained when the sample touches the middle of the shadow mask. This condition requires a sample size of at least 10 mm×14 mm.

3.2.1 Magnetization reversal via uniform rotation

The spin transport model as treated in chapter two, describes the difference in conductance of a device for parallel and antiparallel alignment of the magnetization of the two ferromagnetic electrodes. As shown in previous section, this has to be controlled via shape anisotropy. The magnetization M of both electrodes is controlled with an external, in-plane magnetic field H. While switching from negative to positive values hysteresis in the magnetization will be present and parallel and anti-parallel alignment can be achieved.

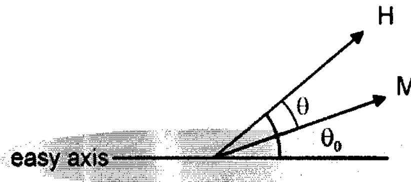

Figure 3.3: Definition of the geometry in the Stoner-Wohlfarth model. The applied magnetic field is at an angle θ_0 with the easy axis, and θ with the magnetization vector.

The simplest description for the magnetization due to an applied magnetic field is provided by the Stoner-Wohlfarth (SW) model. It assumes a single ferromagnetic domain and coherent magnetization. The total energy for an ellipsoid is written as a sum of two, in our case most important anisotropy contributions: shape and magnetostatic anisotropy:

$$E = -\left(H_a + (N_{\parallel} - N_{\perp})M_s\right)\frac{M_s}{2}\cos^2(\theta - \theta_0) - HM_s\cos\theta, \tag{3.4}$$

where $N_{\parallel}$ and $N_{\perp}$ are the demagnetization factors parallel and perpendicular to the easy axis, $M_s = M/\cos\theta$ the saturation magnetization, H_a the anisotropy field, defined as the applied field at which the magnetization is saturated for $\theta_0 = \pi/2$, with θ and θ_0 respectively the angle the magnetization direction and the applied field and the angle between the external field and the easy axis. The origin of shape anisotropy is related to the presence of demagnetizing fields. The magnetization of a magnetic object will tend to align with the direction of the external field. This will form fictitious magnetic poles at the surface, which creates an opposite field of

magnitude inside the object and tends to demagnetize the object. In increasing the strength of a negative field, the energy minimum shifts to smaller values of θ and a discontinuity in θ can occur. The energy minimum with respect to θ is given

$$2\left(H_a + (N_{\|} - N_{\perp})M_s\right)\frac{M_s}{2}\cos(\theta-\theta_0).\sin(\theta-\theta_0) + HM_s\sin\theta = 0 \tag{3.5}$$

This equation can be solved for M/M_s as function of H/H_a for different θ_0 and $(N_{\|} - N_{\perp})$. In figure 3.3 $(N_{\|} = N_{\perp})$ the stable position of the magnetization vector is shown, dependent

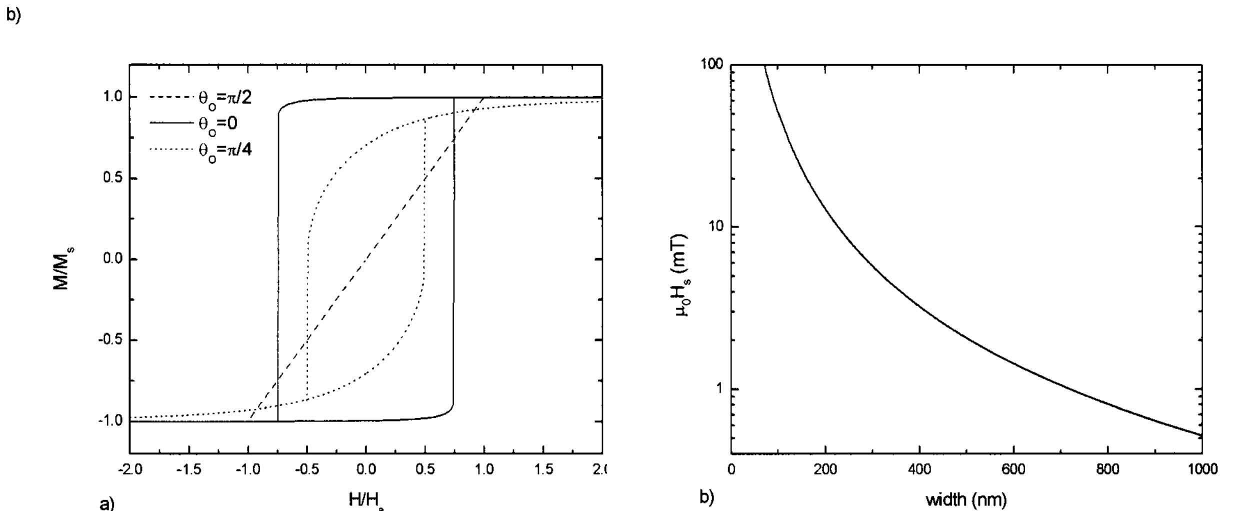

Figure 3.4: (a) Calculated magnetization in the Stoner-Wohlfarth model, for the applied field along the hard axis θ_0=$\pi/2$, the easy axis θ_0=0 and for and for an intermediate angle θ_0=$\pi/4$. (b) Expected behavior of the coercive field of a single domain ferromagnetic bar as a function of its width according to the curling model. $\theta = 0$

on the external magnetic field. In fact, on the vertical axis is shown the cosine of the angle between the the magnetization and the positive direction of the applied field. For a particular magnetic field $H = H_s$, with H_s the switching field, the magnetization reversal process leaves the magnetization in an unstable orientation and a jump to a new stable minimum energy occurs. The switching occurs at the field for which the free energy minimum $dE/d\theta = 0$, becomes flat, $d^2E/d\theta^2 = 0$:

$$H_s = \left(H_a + M_s(N_{\|} - N_{\perp})\right)(\sin^{2/3}\theta_0 + \cos^{2/3}\theta_0)^{-3/2}. \tag{3.6}$$

Using two ferromagnetic electrodes of different shape, the magnetization of the two layers switches to the opposite direction at different values of the applied magnetic field. The applied field is chosen parallel to the easy axis of the electrodes, i.e. $\theta_0 = 0$. The magnetization switch is than instantaneous and complete, and leads during transport measurements to sharp changeovers between low and high resistances (see figure 3.11a). Exactly the same magnetization-applied magnetic field curve is obtained as shown in figure 1.1 for TMR via shape anisotropy. This means that the magnetization of the injector and detector are anti-parallel for external fields $H_{s1} <\mid H\mid_{\uparrow} < H_{s2}$ and $-H_{s1} < -\mid H\mid_{\downarrow} < -H_{s2}$, the arrows denoting the sweep direction. For H outside these ranges the magnetization of injector and detector are parallel.

Single-domain particles do not always change their magnetization by coherent rotation of all moments as just described. Therefore, the SW-model does not predict the coercive field reasonably well when the applied field is close to parallel to the easy axis. Wernsdorfer *et al.* suggested the curling model for describing magnetization reversal for particles that are still too small to contain a domain wall. This model, valid for small values of θ_0, allows for easier magnetization

rotation and hence lower switching fields than in the Stoner-Wohlfarth limit are obtained [66]. A non-uniform magnetization reversal is assumed, because of the magnetization direction is rotated in a plane perpendicular to the anisotropy axis of the wire. This effectively reduces the longitudinal component of the magnetization and hence the magnitude of the switching field. Magnetization switching by curling costs exchange energy, but saves magnetostatic energy by having fewer spins pointing away from the easy axis at any stage of the reversal process. The hard-axis magnetostatic energy has to be replaced with a curling energy due to curling. A rectangular geometry is unfortunately not analytical solvable, but for an infinite cylindrical wire (width/thickness> ∞), the switching field is calculated by Frei *et al.* [67]. The switching field as a function of the direction of the applied magnetic field reads:

$$H_s = \frac{\pi}{2}\frac{M_s}{\mu_0}\frac{a(a+1)}{\sqrt{a^2+(1+2a)\cos^2\theta_0}}, \quad \text{with} \quad a = \frac{d^2 M_s^2}{4A} \tag{3.7}$$

with d the cylinder diameter, μ_0 the permeability of the vacuum and A the exchange interaction constant [68]. We note that the coercive field is only determined by the width of the wire. The saturation magnetization of CoFe is 2 T and the exchange length d_0=$2A^{1/2}/M_s$=20 nm is estimated half of the quoted value for Ni (41 nm) [69]. Figure 3.4 shows the expected switching fields according to equation 3.7. These estimations are based on room temperature. However, for low temperatures the activation energy is lower and the moments become pinned on impurities and defects. A switching field, which is ten times higher as given in figure 3.4 is expected. Another possible mechanism that accounts for the magnetization reversal is the formation of a domain structure within the wire. We can not exclude that nucleation of a domain wall take place at one end of the electrode and it will propagate along the wire.

3.3 Sample fabrication techniques

3.3.1 Sputtering

Sputtering is a process whereby the material to be deposited is bombarded by high energy particles. The particles of target material are ejected from the surface of the target into the volume of the deposition chamber, where they cover a substrate which faces the target and forms a thin film. This is achieved in practice by placing the target material at a high negative potential in a noble gas, usually Ar, environment, which ensures a minimum of chemical reactions with the ejected atoms. The gas is ionized by ignition of an electric discharge between a grounded dark space shield and the cathode, creating a plasma, in which the Ar^+ ions accelerate towards the target where it transfers its momentum to the target atoms. Due to bombardment a number of 'secondary' electrons are emitted from the target surface and are accelerated and collide with the gas atoms and produce the ionization required to sustain the discharge. A cylindrical shaped permanent magnet is placed just above the target material, and generates a magnetic field which serves in this respect as a trap for the electrons and ions. This is because the field lines are mainly parallel to the target surface and cause them to spiral with a drift motion parallel to the surface. The purpose of this is to avoid a motion of the electrons towards the grounded dark space shield and a motion of the ions towards other material than the target material. The plasma is confined in a region near the target surface.

The metal and silicon dioxide layers in this thesis are deposited in a Kurt J. Lesker, UHV sputter-chamber with a base pressure of $< 3 \cdot 10^{-8}$ mbar. Six water cooled sources, operable in DC (metals) or RF (insulators) mode were available. Structures of nanometer sizes can be grown with self-designed masks of molybdenum, which can be placed on top of the sample. Deposition takes place by simple facing the substrate plate under the desired material during a certain time interval. This interval determines the layer thickness, and is controlled through movement of shutters. Calibration of the sputter rate is performed with X-ray diffraction (XRD). In this thesis all layers are sputtered at ambient temperature with a source to substrate distance of 95

mm to allow a maximum area of uniform deposition. Other parameters which must be controlled are the sputter power and Ar flow rate, influencing the number of particles and their energy, respectively.

3.3.2 Molecular Beam Epitaxy

Molecular beam epitaxy (MBE) is a versatile technique for growing thin epitaxial hetero structures made of semiconductors, metals or insulators via thermal evaporation of atoms from a metal source and subsequent condensation in ultrahigh vacuum onto a heated substrate to form a film [70]. The elements aluminium and silicon are vaporized by electrical heating up to its melting point in furnaces. Together with gallium and arsenide from cracker cells, they are directed with orifices towards the substrate. At this low pressure, the mean free path of molecules between collisions is much larger than the width of the chamber. This is the Knudsen regime of a gas, and the furnaces are called Knudsen cells. Molecules that emerge from the K-cells do not diffuse as in a gas at high pressure, but form a molecular beam travelling in straight lines without collisions until they impinge on the substrate or elsewhere. Here it crystallizes in a structure with a well-defined relation between the crystal axis of the film and the crystal axis of the substrate. The composition of the grown epilayer and its dopants depend on the relative arrival rates of the constituent elements and dopants, which in turn depend on the evaporation rates of the appropriate sources. The growth rate of typically a monolayer per second is low enough that surface migration of the impinging species on the growing surface is ensured. Consequently the surface of the grown film is very smooth. Simple mechanical shutters in front of the beam sources are used to interrupt the beam fluxes, that is to start and stop the deposition. Changes in composition and doping can thus be abrupt on an atomic scale. The advantage of MBE growth is that it is carried out under conditions far from thermodynamic equilibrium and it is governed mainly by the kinetics of the surface processes occurring when the impinging beams react with the outermost atomic layers of the substrate crystal. Defects have time to remove. This is in contrast with growth techniques, which are most controlled by diffusion processes occurring in the crystallizing phase surrounding the substrate crystal. A second advantage is an ultra high vacuum environment, to reduce contamination. Moreover the growth may be controlled by in situ surface sensitive diagnostic methods to monitor the growth, layer thickness and the amount of deposited materials.

3.3.3 Electron Beam Lithography

In electron beam lithography (EBL) a focussed beam of high energy electrons exposes an electron sensitive resist on a suitable substrate. All small electrodes and connections to the large contact pads have been fabricated with a RAITH Turnkey 150 scanning electron microscope customized for EBL, with the following specifications; 30 kV ac voltage, 120 mm sample space, laser interferometer xy stage (20 nm accuracy), 10 MHz beam blanker and air damping system. The magnification $\times$ write field area product is fixed at 60000. In order to avoid distortions through deflection of the 'optical' axis, but conversely having an acceptable working area, we choose for a magnification of 100. Now the maximum writing area is fixed at $600\mu m \times 600\mu m$. The smallest possible (DAC) step (pixel size), defined by dividing the field size by 16 bit is 10 nm. For optical lithography, preparation of masks is a time consuming step. For EBL are no masks required, a design is made with a computer program and can be directly used to expose. A disadvantage of EBL is the long scanning time, a crucial parameter in the industry. An electron sensitive resist, usually based on polymethyl methacrylate (PMMA), is spin coated on a sample and afterwards baked in an oven. A predefined pattern is scanned using a high energy electron beam, by which the polymer chains exposed to the electron beam are broken and become soluble in a suitable developer. The maximum resolution obtained in the system is not determined by the diameter of the beam nor the electron wavelength, but by the scattering and subsequent broadening of the electron beam in the resist. This phenomenon is called forward

scattering and the full width halve maximum of effective beam intensity is 30-50 nm. In the second place, scattering of the electron beam in the substrate and the subsequent reflection back into the resist determines the resolution (backscattering; full width halve maximum of effective beam intensity 1-10 μm). The backscattering gives rise to secondary exposure and is especially strong near large exposed areas. The resist sensitivity (charge per unit area) is the product of the beam intensity and the dwell area time (exposure time of an unit area). Next the sample is put in a developer, e.g. methyl isobutyl ketone (MIBK), which removes the exposed area of the resist. After metal deposition with dc sputtering the whole sample is put in a solvent, usually warm acetone, to remove the polymer layer and the metal on top of it (lift off). In the next section we will describe these processes in more detail.

3.4 Sample fabrication

In this section we describe the fabrication process of the lateral double barrier device. Underneath all taken steps are described.

- **step 1: wafer growth**: All the operations in this step are done in-situ in a MBE at IMEC Leuven (Belgium) in the group of G. Borghs and J. de Boeck. A GaAs (100) undoped semi-insulating wafer, which is cleaned by sputtering and afterwards annealed, is used as a substrate. A thick GaAs undoped buffer layer is grown for reducing the roughness, followed by an 100 nm undoped $Al_{0.3}Ga_{0.7}As$ barrier layer in order to ensure carrier confinement. Subsequently a 100 nm active n-GaAs layer: Si doping level ($4 \cdot 10^{17}$ cm^{-3}) is grown. In order to suppress 'Schottky' barrier formation, three 2.5 nm thick undoped GaAs surface layers are grown, containing each a delta-doping of ($5 \cdot 10^{13}$ cm^{-2}). Finally at IMEC, 1.5nm of aluminium is grown and oxidized naturally in order to obtain tunnel barriers. The advantage is that the wafer is now naturally protected against oxidation.

- **step 2: wafer cutting and cleaning**: Out of the 2 inch wafer pieces of 10 mm$\times$14 mm is cut. Next the sample is cleaned from organic material by moving it gently for 10 minutes in a bath of a mixture of 50% acetone and 50% 2-propanol (IPA), close to the boiling point. The acetone residues are removed from the surface in an alcohol bath for 2 minutes. For drying clean, the sample is placed for at least ten minutes in a saturized isopropanol environment. No ultrasonic bath can be used because GaAs is very brittle. As compensation, we hope to increase the effectiveness of removing organic components by heating the cleaning liquid. Instead of the usually used ammonia we choose for acetone.

- **step 3: bonding pads and insulation deposition**: Dust on the sample surface should be avoided. Therefore a clean storage and work environment is necessary. The sample is mounted with conducting silver paint on the holder in the clean room and covered with a lid. The lid is removed in-situ in the sputter machine. Making use of in-situ shadow mask, 0.1 mm and 0.2 mm channels are defined by covering the rest of the sample with a 100-500 nm insulating SiO_2 layer (RF sputtered at ambient temperature). The procedure of sputtering SiO_2 is as follows; we start at 100 W, with a bias voltage of 290 V, a flow rate of 50 sccm Ar, during 60 minutes. At this high flow rates (standard 7 sccm), the number of collisions in the plasma is large, resulting in a low kinetic energy of the particles. To compensate for the low deposition rate, the power is increased (standard 20 W) up to 100 W. A higher power means a higher current, more bombardments and more particle will come off the target surface. If there is a good wetting layer, both the power and flow rate can be cut back to grow a thick insulating layer, successively: 100 W 40 sccm Ar 60 minutes 291 V, 80 W 30 sccm Ar 60 minutes 260 V and 80 W 20 sccm Ar 120 minutes 259 V. Large tantalum bonding pads 100-150 nm are sputtered (20 W, 10 sccm, ambient temperature) on top of the SiO_2.

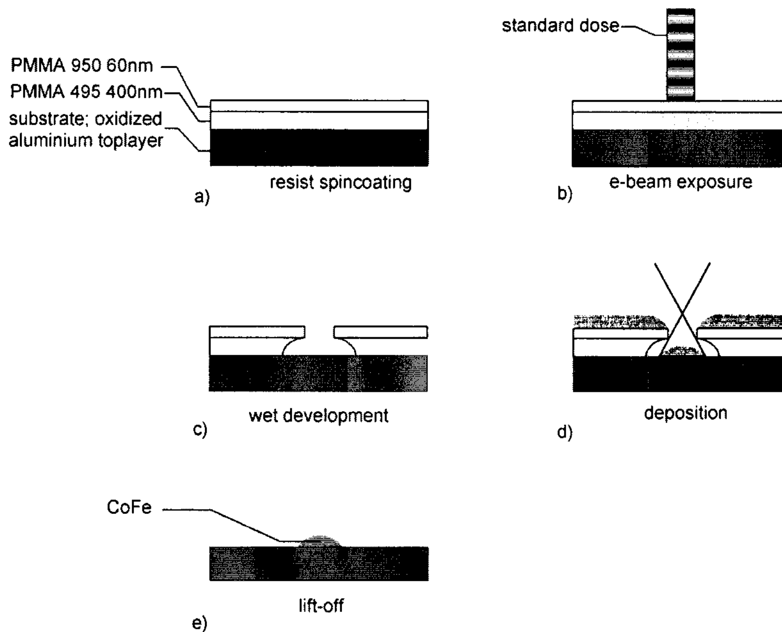

Figure 3.5: (a-d) Schematic representation of the lithographic PMMA bi-layer system to create a mask for shadow sputtering. The procedure is described in the text. (e) Phase contrast lightmicroscope photo of the EBL defined electrodes, connection wires to the Ta bonding pads. (f) Magnification of a part of (e), showing a part of the two separated electrodes and a part of the connection wire to the top Ta bonding pad.

- **step 4: spin coating**: We make use of a PMMA bi-layer for e-beam lithography. The sample is covered for 70% with two drops of a high sensitivity polymethyl methacrylate (PMMA) 495 A6 (respectively molecular weight and percentage of anisole, a solvent) and spin coated at 2000 rpm for 50 seconds until the thickness remains constant. We obtain a 4000 Å bottom layer (see figure 3.5a). The resist is baked for 30 minutes in a hot oven at 175°C. For the top layer a high sensitivity PMMA 950 A2, a spin speed of 5000 rpm for 50 seconds and the same baking setting are used, obtaining a thickness of around 600 Å. For the top layer the solvent is weaker to prevent intermixing of the two layers during application of the second layer. The layers have different molucular weights, the heaviest compound on top. In this way a slightly overhanging resist profile is created, which is important for a good lift off, especially in case of sputtering.

- **step 5: E-beam pattern definition**: The sample is exposed at places where the electrodes are planned, using a 30 keV electron beam with a typical dose of 150 μCcm^{-2} (figure 3.5(b)). The writing area is larger than the electrode dimensions, but smaller as the distance between the large Ta contact pads. For both electrodes 10 μm wide connection wires (see figure 3.6a) to the pads are made by shifting the middle of the writefield 590 μm up- and downwards. Matching of the wires beween two writing areas is ensured by the overlap of the two areas, and in the other direction, by small stripes written perpendicular to the wires. A wet development step is carried out for 60 seconds in a 3:1 mixture of IPA:MIBK, flushed for 60 seconds in IPA and dried with argon (figure 3.5(c)). No surface cleaning is performed, e.g. a short anisotropic oxygen etch in a strong ion etcher to remove the last PMMA remnants left on the substrate (Typically values should be oxygen pressure 10 μbar, power 40 W, etch time 20 seconds).

- **step 6: electrode deposition**: It is worthwhile to view the sample with a phase contrast microscope to check the pattern. The sample is transferred back to the sputter facility to deposit a uniform layer (20 nm) of $Co_{90}Fe_{10}$ (20 W, 7 sccm, ambient temperature), capped with 10 nm of Ta (20 W, 10 sccm, ambient temperature) (figure 3.5(d)). The last step in the process is the lift off (figure 3.5(e)). The sample is immersed in boiling acetone until all residual material has lifted off. Then it is flushed in cold acetone and dried with argon. If the bottom PMMA layer is of the same thickness as the $Co_{90}Fe_{10}$ electrode, the electrode touches the mask. The adhesion (Van der Waals-forces) between the electrode and the substrate can be weaker than the binding force between the PMMA and the electrode. There is a chance that the complete electrode will be removed with the PMMA mask during the lift off. Therefore the bottom layer has to be at least thicker as the $Co_{90}Fe_{10}$ electrode. A factor of 2-3 is recommended for sputtering.

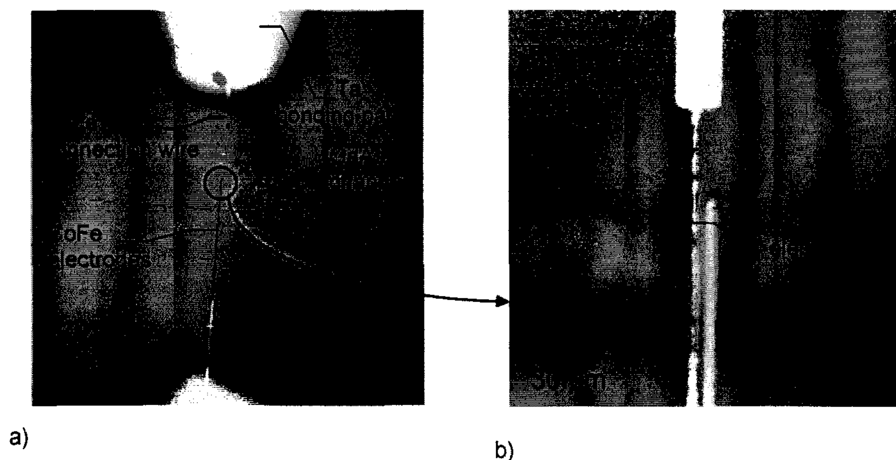

Figure 3.6: (a) Phase contrast lightmicroscope photo of the EBL defined electrodes, connection wires to the Ta bonding pads. (b) Magnification of a part of (a), showing a part of the two separated electrodes and a part of the connection wire to the top Ta bonding pad.

Via above described recipe, lithographic defined masks with high enough undercuts were created, that lift-off was possible (see for an exdample figure 3.6a and b). Subsequently, we were able to produce electrodes with width of 200 nm and 500 nm and a length of 200 μm, at a distance of 800 nm. Smaller spacings up to 400 nm were only obtained for wider electrodes (500-1000 nm respectively).

3.5 Characterization techniques

3.5.1 Transport measurements

Transport measurements are performed with a home-built setup, which is equipped with a 1.35 T magnet and a 1.2-400 K variable temperature helium flow cryostat. A custom made probe for soft contacts between external wiring and the tantalum bonding pads on the sample is available. A separate insulating ertelyte holder is designed (see appendix figure 5.4) to prevent perforation of the thin SiO_2 and Al_2O_3, by for example metal contact pins. This would definitely lead to short-circuits. Fourteen wires coming from an ic-pin, are fixed at the ertelyte holder next to the the sample. They can be bend up to just above the sample surface. Twelve wires are connected to the Ta bonding pads and two are connected at the GaAs channel contacts. Good conducting contacts are made with silver paint. This ertelyte holder exactly fits in the ertelyte head of the probe (see appendix figure 5.3), and the ic-pin fits in another ic-pin (fixed in the

ic-pin holder of gilded copper (see appendix figure 5.3)), which is connected with the external wiring. The design of the probe is suited to fit in the cryostat. A measurement of six devices per run with a magnetic field parallel to the plane of the layers with an arbitrary in-plane angle is allowed. The set-up is current-based, this means that the current is varied (2 nA-100 mA) and a voltage is measured. Resistances of $\sim$0.1 Ω - 500 MΩ could be measured with dc current using a high impedance (>10G Ω), or resistances of $\sim$0.1 Ω - 100 kΩ with ac current (f$\sim$1-100 Hz) using a lock-in amplifier to measure the ac voltages. In addition, V(I), dV/dI(I) and $d^2V/d^2I(I)$ could be measured simultaneously. On top of a dc current a small constant ac current δI_{ac} was applied, which causes a voltage $V_b = V_b(I_{dc} + \delta I_{ac} cos(2\pi f t))$ over the junction. By performing a Taylor expansion about I_{dc}, it follows that the resulting ac voltage at the frequency f (i.e. V_{1f}) proportional is to dV_b/dI and the signal at $2f$ (i.e. V_{2f}) is proportional to d^2V_b/d^2I. V_{1f} and V_{2f} could be measured with two lock-in amplifiers. Within the controlling system, it is possible to program temperature, current or field sweeps during a measurement.

As mentioned in chapter 2, there are in principle two ways to measure transport properties. The first option is a conventional two-point geometry (figure 2.11), where the current flow and measured voltage drop are mutual influencing each other. Besides, it affects the efficiency in tunnel barrier measurements, and it gives possibly rise to AMR contributions and Hall effects. In a non-local four-point geometry (figure 2.17), these effects are absent, but such geometry has to be often measured with more sensitive lock-in techniques. Our lateral device is a metal-insulator-metal structure, which means that is has a capacitance. Thus the conduction at finite frequency can be via tunnelling or via capacitance. At high frequencies, most current will be via the capacitor, since the impedance is inversely proportional to the driving frequency. At low frequency, the current is mostly due to tunnelling, because the capacitor has essentially an infinite impedance. The frequency for which the tunnel current is still an order of magnitude higher greater than the capacitive current is estimated at $1/2\pi CR$, with R the resistance of the whole device ($\approx$ 20 kΩ) and $C = A\epsilon_0\epsilon_r/d$, the capacitor when it is parallel to the resistance of the tunnel barrier. Herein is A the typical area of the electrodes, ϵ_r the relative dielectric constant and d the spacing between the electrodes. It turns out that the capacitor of our device is smaller than the typical capacitance of our measuring setup, 1 nF, and thus the excitation frequency is limited by 100 Hz.

A notorious problem in four point measurements is 'current-crowding'. Current is flowing laterally through one electrode, then vertically through the barrier and again laterally though the channel. If the tunnel barrier resistance is comparable to the electrode sheet resistance, the current flow through the barrier is inhomogeneous. The current will mainly flow through the corners of the barrier. Since the voltage drop is measured at the opposite corners, the measured voltage drop in this case is anomalously low. This leads to very low or even negative apparent resistances.

3.5.2 The Van der Pauw method

In this subsection we will discuss a method proposed by Van der Pauw [71] measuring the square resistance of flat conducting samples of arbitrary shape if the contacts are sufficiently small, fixed at the circumference of the sample and the sample is singly connected, i.e. it should not have isolated holes. First a semi-infinite sample is considered with successive contacts P, Q, R, S at the boundary, respectively spaced at distances a, b and c (figure 3.7a). The resistance $R_{PQ,RS}$ is defined as the potential difference between points R and S divided by the current flowing from contacts P to Q. ρ is the specific resistance of the material and d the thickness. From elementary electrodynamics it can be calculated [72] that:

$$R_{PQ,RS} = \frac{V_S - V_R}{j} = \frac{\rho}{\pi d} \ln \frac{(a+b)(b+c)}{b(a+b+c)}, \tag{3.8}$$

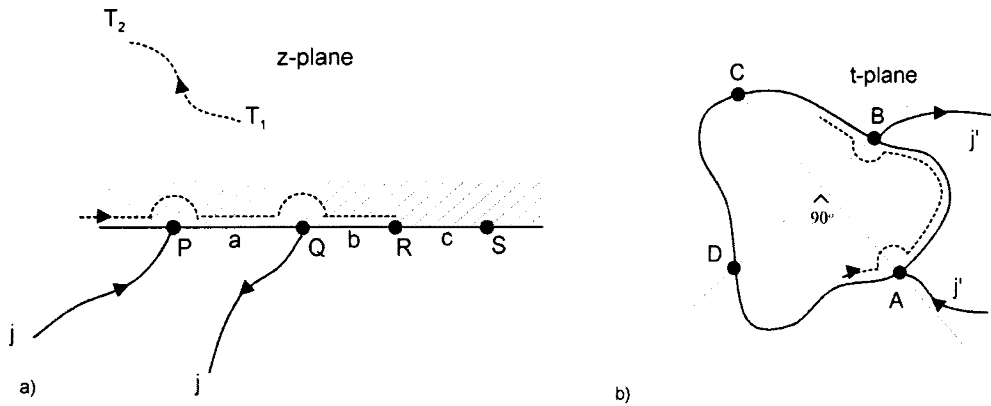

Figure 3.7: (a) A sample in the form of a semi-infinite plane with four contacts along its boundary for which equation 3.10 is proved first. (b) A sample of arbitrary shape, for which is proved that it also satisfies equation 3.10 and 3.14. In the drawing it is shown that the four contact points are spaced at 90°. This requirement is only of importance in our description of the Hall effect (section3.5.3)

and analogously:

$$R_{QR,SP} = \frac{\rho}{\pi d} \ln \frac{(a+b)(b+c)}{ac)}. \tag{3.9}$$

Combining both equations 3.8 and 3.9 gives:

$$\exp(-\pi R_{PQ,RS} d/\rho) + \exp(-\pi R_{QR,SP} d/\rho) = 1. \tag{3.10}$$

Van der Pauw showed that equation 3.10 holds for every arbitrary surface as shown in figure 3.7(right). Below we will illustrate how this is derived. The semi-infinite sample considered above is assumed to coincide with the upper part of a complex z-plane, where $z = x + iy$. A function $f(z) = u(x,y) + v(x,y)$ is chosen where u represents the potential field in the sample. u and v should be real and the Cauchy-Riemann relations $\partial u/\partial x = \partial v/\partial y$ and $\partial u/\partial y = -\partial v/\partial x$ have to be fulfilled. Travelling from an arbitrary point T_1 to another point T_2 both in the upper half-plane (fig. 3.7(right)), the net current traverses our path from right to left is

$$j_{T_{2,1}} = \frac{d}{\rho} \int_{T_1}^{T_2} E_n ds, \tag{3.11}$$

with E_n the normal component of the electric field. Filling in:

$$j_{T_{2,1}} = \frac{d}{\rho} \int_{T_1}^{T_2} \left(-\frac{\partial u}{\partial y} dx + \frac{\partial u}{\partial x} dy \right) = \frac{d}{\rho} \int_{T_1}^{T_2} \left(\frac{\partial v}{\partial x} dx + \frac{\partial v}{\partial y} dy \right) = \frac{d}{\rho} (v_{T_2} - v_{T_1}) \tag{3.12}$$

This expression says that taking a path on the real axis from $-\infty$ to $+\infty$ the value v is constant up to point P. For a half-circle in the upper plane around point P, v increases with $\rho j/d$, similarly at point Q, but then a decrease. Let us consider now an arbitrary shape lying in a different complex t-plane. There is an analytic function such that the upper half-plane in the z-plane is mapped onto the same sample in the t-plane ($t = r + si$). Now the transformation $f(z) = f(z(t)) = k(t) = l + im$ is calculated from which follows that m remains constant at the edge of the sample A, B, C and D in the t-plane are the images of P, Q, R and S in the z-plane. Analogously travelling now counterclockwise along the edge in the t-plane m is constant and find again an increase respectively decrease of $\rho j/d$ at points A and B. Interpreting l as the potential field in the t-plane, and a current j' enters the t-plane with specific resistivity ρ' and thickness

d' at A and leaves at B then the voltage difference V_D-V_C is equal to V_S-V_R. $(d/\rho)R_{PQ,RS}$ remains the same under conformal transformation and equation 3.10 is of general validity. The specific resistance is now uniquely determined with equation (3.10) by two resistances $R_{AB,CD}$ and $R_{BC,DA}$ and will be used in our experiments.

3.5.3 Hall effect

Let us consider a 'bridge-shaped' sample. We assume the current is uniform and the voltage contacts points are perpendicular to the current flow and they are spaced at the same distance of the current flow. The requirements for the Van der Pauw method are still valid. Because in our experiments, square samples with a contact geometry as shown in figure 3.7 are used, errors will be introduced [71]. The mobility ν can be obtained by measuring the change in $R_{BD,AC}$ due to a perpendicular magnetic induction B. The explanation is as follows. A current density $\underline{j}$' from point A to point B through the sample satisfies $\nabla \cdot \underline{j}' = 0$ and $\nabla \times \underline{j}' = \underline{0}$ and the outer lines of flow following the edge, fully determine our boundary conditions. So on applying a external magnetic field perpendicular to the plane of the sample, these lines do not change, but indeed if j' is the current through from one point to an opposite point, there is built up an additional electric potential between the two other 90° turned opposite points equal to

$$\Delta V = \frac{\nu B j' \rho}{t}, \tag{3.13}$$

with t the thickness of the sample. It should be noticed that if the points are not spaced at equal distances from each other, an off diagonal electric potential term is measured. The Hall mobility is then given from equation (3.13) by:

$$\nu = \frac{t}{\rho}\left(\frac{\partial \Delta R_{BD,AC}}{\partial B}\right). \tag{3.14}$$

In practice, the mobility can be determined by measuring the difference in $R_{BD,AC}$ caused by an applied magnetic field. If we assume that the only carriers are electrons, then the effective carrier concentration is directly given by equation (2.28).

3.6 Results

3.6.1 GaAs wafer characterization

On a standard sample GaAs(100)/ GaAs(undoped buffer)/ $Al_{0.3}Ga_{0.7}As$ (100 nm)/ GaAs (Si doped $4{\cdot}10^{17}$ cm^{-3} 100 nm)/ GaAs (Si δ-doped $5{\cdot}10^{13}$ cm^{-2} 3×2.5 nm)/ Al_2O_3 (1.85 nm) four small contacts were made, spaced at 90 degrees and are situated at the edge (see figure 3.7b). The square resistance in the active layer is measured with the Van der Pauw method (see section 3.5.2 eq. 3.10). The layer shows a square resistance of 51 Ω and 59 Ω at 5 K and 300 K, respectively. This is a factor 50 higher than expected. The mobility and effective carrier concentration were obtained from Hall measurements (see figure 3.8) using equations 3.14 and 2.28 and listed in table 3.1 next to the expected values. The mobility is lower as expected, but still indicating excellent growth properties, low density of impurities, defects and dislocations. The effective carrier concentration is two orders higher as desired. In addition, the mobility and effective carrier concentration measured at room temperature differ only 10% from the measured values at 5 K, which is also indicating a highly doped semiconductor [28]. the origin of this discrepancy is a growth error due to uncorrect Si dopant calibration (confirmed by W. van Roy). The Si concentration was roughly ten times higher than intended, resulting in doped delta-layers with an extremely high Si content. Recalculation of the surface doping level into a volume doping, designed to compensate for the Schottky barrier formation, is equivalent to a layer of 7.5 nm of $2{\cdot}10^{21}$ cm^{-3}. If this charge instead of being compensated by the charge of

the interface states, is fully redistributed into the 100 nm thick layer, this would correspond to a bulk doping level of $1.39 \cdot 10^{20}$ cm^{-3}. This is almost in accordance with the measured value of $1.6 \cdot 10^{19}$ cm^{-3}. The fact that the measured electron concentration is lower, is probably caused by covalent bondings of Si atoms, which share their electrons.

Table 3.1: Measured intrinsic properties of a $Al_{0.3}Ga_{0.7}As$)/ GaAs (Si doped) /GaAs (Si δ-doped) wafer compared with the expected values.

	Expected	Measured	
		5K	RT
square resistance	$2.5\ k\Omega$	$51\ \Omega$	$59\ \Omega$
effective carrier concentration	$4.0 \cdot 10^{17}\ cm^{-3}$	$1.69 \cdot 10^{19}\ cm^{-3}$	$1.54 \cdot 10^{19}\ cm^{-3}$
mobility	$1.3 \cdot 10^{3}\ cm^2/V \cdot s$	$720\ cm^2/V \cdot s$	$688\ cm^2/V \cdot s$

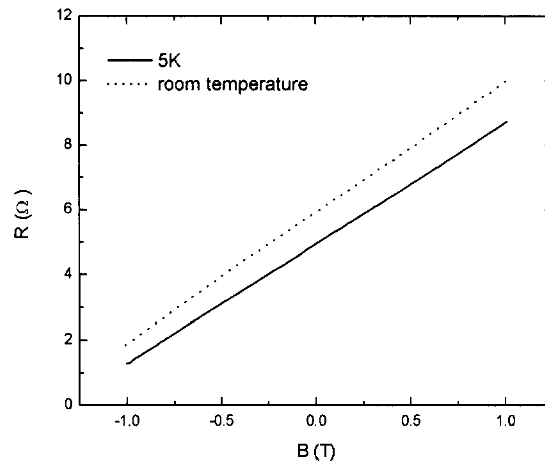

Figure 3.8: Hall measurement at 5 K and room temperature of modulated GaAs wafer. The resistance $R_{BD,AC}$ is measured as function of the magnetic field perpendicular to the sample.

3.6.2 Insulator choice and characterization

Just after sputtering the large bonding pads (step 3 section 3.3) the resistance of the SiO_2 has to be measured locally at 5 K between two bonding pads at low bias voltage (<30 mV) to prevent destruction of the insulating layer. To avoid current leakage through the the SiO_2, the resistance should be much higher than all other device components, i.e. >1 MΩ.

An insulation layer with an extremely low conductance, may appear rather trivial to fabricate. Even if there are no serious conditions to the thickness and material. For this purpose strontium titanate ($SrTiO_3$), Al_2O_3 or baked PMMA are a few considered options. $SrTiO_3$ was deposited analogously to the fabrication description as used by D. Serrate of l'Institut de Ciència de Materials de Barcelona-CSIC, i.e. a 100 W RF, (50.0 sccm Ar + 5.6 sccm O_2) plasma for a total time of 65 minutes. Resistances between two bonding pads up to 1 kΩ were obtained. With hindsight, we can say that probably the same conditions as described below for SiO_2 contributes to this small resistances. A second possibility is oxidation of aluminium, but this process is limited to 25 Å. Repeated growth of insulating Al_2O_3 on top of each other is not technologically feasible, because Al grows in islands on top of Al_2O_3. Experimentally, the maximum obtainable resistance for an area of 5 mm×0.3 mm is in the order of 100 kΩ, independent of the nummer of oxidation steps. PMMA (950k Az) at 5000 rpm spin coated, a third possibility, should be

work out fine as an insulator. With EBL a window can be defined analogously to our channel. After baking at higher temperatures, complete repolymerization is established. Afterwards the electrodes and large contact pads can be deposited in the same manner as described in section 3.3. The issues for this route are the impact of baking on our tunnel barrier, and the extremely high aspect ratios at the edges of the defined window. Therefore to keep a 30 nm thick electrode connected across this sharp edge, the thickness of the PMMA is limited.

Thermal oxidized or spin coated SiO_2 is a commonly used technique for cheap and fast manufactured insulating layers in the commercial industry. These techniques destroy our semiconductor heterostructure or cannot create patterns, respectively. Therefore, we chose for RF sputtering, in combination with shadow masks. For us, it appeared to be not straightforward to attain over a squared millimeter a nanometer thick insulating layer (that is above $1 \cdot 10^{13}\ \Omega \cdot \mu m^2$). The first batches deposited at standard conditions (7 sccm Ar, 40 W RF) indicated at 5 K resistances below 100 kΩ as well as an exponential decrease during heating to room temperature. The first property can be explained by non-ideal growth and the second property is associated with impurities contaminating our structure. In fact the plasma was in contact with the surrounding metals through poor plasma confinement. Therefore the steel ring, which holds the target was substituted by one made of insulating alumina. Simultaneously, the growth characteristics had to be improved. If the growth mode is thermodynamically determined, the process is governed primarily by the film, substrate and interfacial free energies. At most the first monolayers of the film were only wetting the substrate and subsequent growth is in small island or clusters. It is more likely that the low resistance is caused by columnar growth. The film might consists of cylindrical shaped grains which are elongated in the direction normal to the substrate surface. The sputtered tantalum of the bonding pads will go in between the columns and there is a electrical short-cut with the tunnel barrier. This growth mode is dominated by kinetic aspects, e.g. substrate temperature and growth rate [73]. Experimentally is determined that deviation from ambient substrate temperature has no influence on the resistance times area product. However a higher plasma pressure caused by a higher gas flow (50 sccm), will induce more collisions. Less particles with a lower kinetic energy will arrive at the substrate. The decreased deposition rate is compensated by a higher power (100 W), leading to a small increase in bias voltage and a high increase in current. A higher current results in more electron bombardments, and thus more particle will release from the target surface. In order to keep the electric field near the target surface fixed, the dark space shield target distance was increased with 2.5 mm. In this way resistances of insulating layers, measured between two bonding pads, of at least 1 MΩ were found.

3.6.3 Tunnel barrier characterization

The resistance of the CoFe electrode was measured with a four terminal measurement. For this purpose a customized sample was prepared with the same techniques as described in section 3.4. One $Co_{90}Fe_{10}$/Ta electrode of 5 μm wide, 200 μm long and 20 nm+10 nm thick was deposited on top of Al_2O_3. 10 μm EBL defined wide stripes, ensure electrical contact with two opposite bonding pads. Two long 200 nm wide strips connect the ends of the electrode to two other bonding pads. In a four terminal resistance measurement, for the electrode resistance was found 600 Ω at 12.7 K, which is in agreement with the expected value in the order of 1 kΩ (section 3.2). As the electrode resistance is much smaller than the barrier resistance (expected in section 3.2: 1 kΩ-100 kΩ), we conclude that the current will be injected homogeneously in the semiconductor channel.

For investigation of the tunnel barrier properties, two other customized samples were prepared. A $Co_{90}Fe_{10}$/Ta electrode is deposited with a shadow mask as well as one defined with e-beam lithography between two bonding pads on top of the Al_2O_3/GaAs system (see figure 3.9). In table 3.2 the tunnel barrier resistance times area product is shown for both electrodes. Both are higher than estimated in section 3.2. The difference can be explained as due to a too

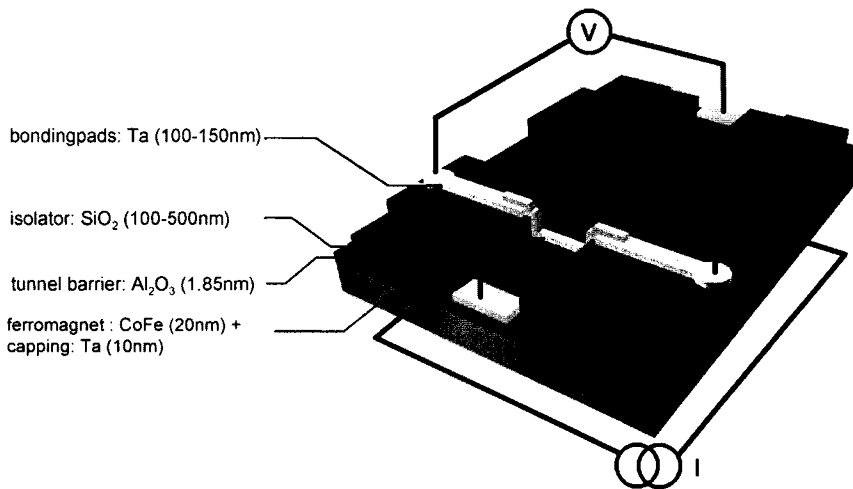

Figure 3.9: Schematic overview of a sample used to measure the tunnel barrier properties. Note that the dimensions are not to scale.

Table 3.2: Measured and expected resistance times area product for an e-beam lithography as wel as shadow mask defined area.

	Dimensions (l×w×h)	Resistance×Area	
		Expected	Measured
E-beam lithography	$200\ \mu m \times 5\ \mu m \times 30\ nm$	$1 \cdot 10^5\ \Omega \cdot \mu m^2$	$5 \cdot 10^{12}\ \Omega \cdot \mu m^2$
Shadow mask	$200\ \mu m \times 200\ \mu m \times 30\ nm$	$1 \cdot 10^5\ \Omega \cdot \mu m^2$	$1 \cdot 10^{10}\ \Omega \cdot \mu m^2$

thick AlOx layer or by the preparation procedure. Some PMMA remnants (undeveloped resist) may lead to decrease in effective tunneling area, resulting in extreme high tunnel barrier resistances. An additional oxide plasma cleaning or a stronger IPA:MIBK solution is recommended. For bias voltages smaller than 1mV, the barrier resistance is larger than the resistances of the electrodes. Thus current distribution effects are in principle not present as described in section 3.2.

For the 5 μm wide electrode, figure 3.10 displays the result of the four terminal voltage current measurements at 300 K and the corresponding dI/dV as a function of the voltage. The shape of the curve is reasonable in agreement with what is expected from the Simmons equation 2.3 with an average barrier height above the Fermi level of 0.82 eV and a thickness of 26.1 Å fitted for negative voltage and 25.8 Å fitted for positive voltages. The non equal curves for both voltage directions reflect an asymmetric barrier as a consequence of the presence of a Schottky barrier as described in section 2.1. Taking into account that the Al_2O_3 tunnel barrier is 18.5 Å, these values would imply a Schottky barrier width of 7.5 Å. A Brinkman fit came out with non realistic values, i.e. 0.4 eV average barrier height, barrier asymmetry -0.9 eV and barrier thickness of 34 Å, because of large bias voltages compared to barrier height. However, we expect that electron tunnelling is probably the main source of conduction. Any other deviations from these simple models is caused for example by hopping conduction (i.e. tunnelling via interface states or impurity states in the barrier) and inelastic tunnelling.

3.6.4 Transport measurements

In a two point local transport measurement a current is send and the voltage is measured between the two electrodes (see figure 2.11b). In a four point non-local measurement the current is send

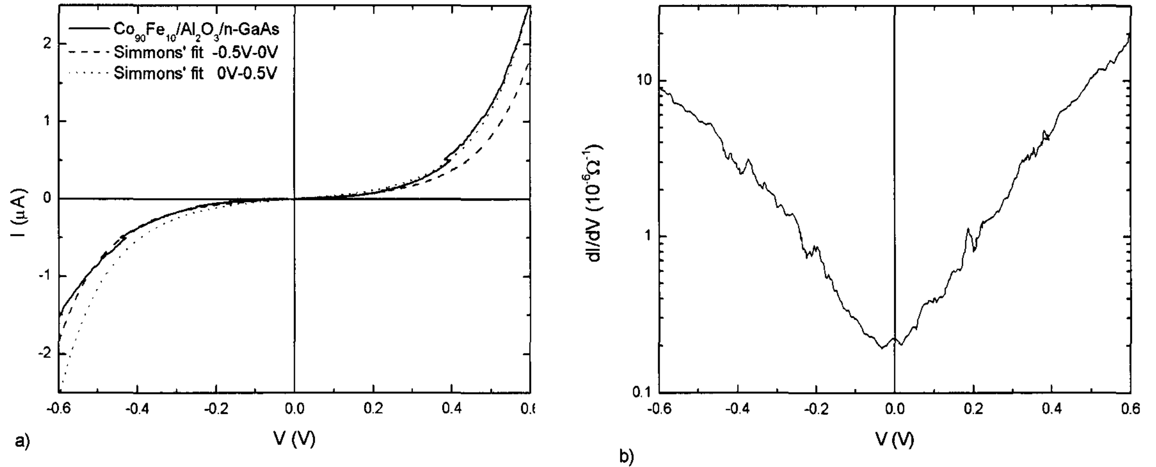

Figure 3.10: (a) Current as a function of the bias voltage for a CoFe/Al_2O_3 system grown on a 'standard' GaAs wafer at 300 K. The dotted (dashed) curve corresponds to a fit to the Simmons' equation for positive (negative) biasvoltages (b) Corresponding conductance (dI/dV) voltage curve.

from one electrode to an extension of the GaAs channel, while the voltage is measured between the second electrode and an GaAs extension on that side (see figure 2.17). As we have seen in section 2.3.5 we expect in both cases, a relative difference in resistance for parallel and antiparallel alignment of the magnetization in the electrodes (see section 3.2.1). The expected magnetoresistance due to spin accumulation in GaAs as function of the applied magnetic field is displayed in figure 3.11a.

On this first devices, two point local transport measurements were carried out at 5 K at a bias voltage between 2.5-3.0 mV. We need to point out that the expected channel resistance was around 0.5 Ω for a 1000 nm long and a 100 mm wide channel (see table 3.1). In the same time, the measured device resistance varied around 17.5 kΩ. This corresponds to a ratio rtb/rch in the order of 10^4. Based on theoretical expectations, the magneto resistance due to spin accumulation is expected to be quenched. As shown in fig. 3.11b, we do not observe any hysteretic magnetoresistance, (i.e. no spin valve effect was observed insofar). The observed magnetoresistance could be explained by AMR or Hall effects, while the oscillations might arise from the temperature drift. In the future, by reducing both the carrier doping of the normal channel and the thickness of the AlOx barrier (i.e. the characteristic resistance area product of the tunnel junctions), better matched devices are expected to show the desired behavior.

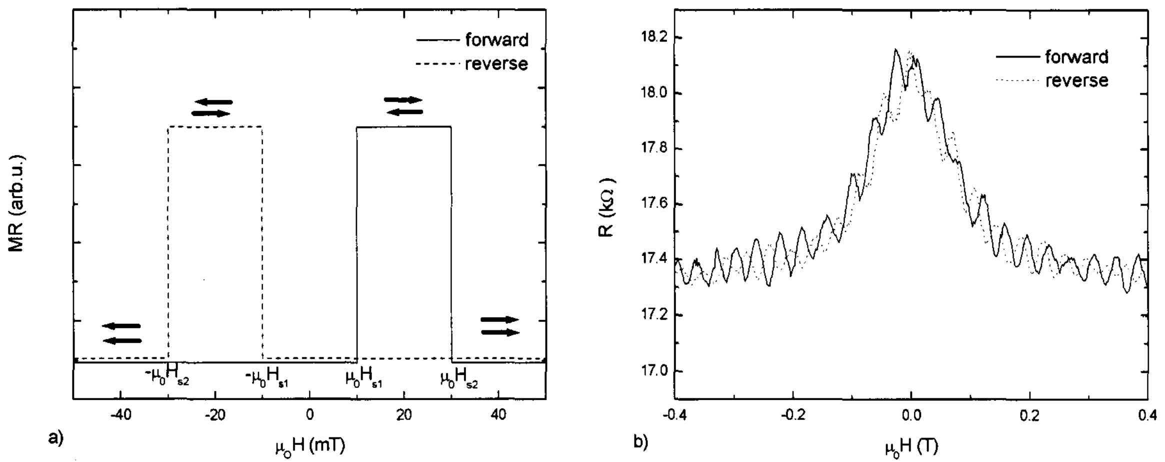

Figure 3.11: (a) The expected spin valve effect due to spin accumulation, where the solid (dashed) line represents a negative (positive) sweep direction. The set of two arrows indicates the direction of the magnetization of the left and right electrode dependent on the applied field. An increase in magnetoresistance is observed, when the configuration is changed from parallel alignment to anti-parallel alignement. (b) Measured magneto resistance in a local measurement geometries at 4.7 K. CoFe electrodes of 200 nm and 500 nm×200 μm spaced at 1 μm, with the applied magnetic field anti-parallel with the electrodes at a bias voltage of 2.67 mV. The solid (dashed) lines corresponds to with a forward (reversed) sweep direction.

Chapter 4

Conclusions and outlook

Electrical spin injection in semiconductors via tunnel or Schottky barrier has been demonstrated [17, 19]. Despite all efforts an all-electrical device demonstrating the manipulation of the electron spin in GaAs has not been reported. Our idea was to make use of a lateral geometry, with two ferromagnetic stripes, acting as injection and detection electrodes, crossing an n-doped GaAs channel. In this way we can make use of standard epitaxially grown GaAs wafers with high mobility and high spin life time. The magnetic properties of the electrodes could be separately controlled by shape anisotropy. In order to have a good spin injection/detection efficiency we tried to use AlOx tunnel barriers. The channel was defined by isolation of the rest of the sample by an insulating SiO_2 layer. We should mention that the realization of such device is non-trivial. It requires a customized MBE-grown GaAs hetero structure (provided by the group of G. Borghs and J. de Boeck from IMEC Leuven) and a combination of multiple in-situ shadow mask deposition and e-beam lithography steps.

A detailed theoretical analysis of the expected magnetoresistance, based on a Boltzmann equation approach is performed. This model is used within the layout analysis of the device and afterwards for interpretation of the observed magnetoresistance. While we have not succeed in demonstrating the spin valve effects, a preparation and characterization recipe for reproducible lateral devices is developed and applied. The following steps towards reaching our goal have been done.

- **Accurate modelling of the device.** From the macroscopic spin transport model derived by Valet and Fert [48], a more general drift-diffusion equation is derived, which is valid for non magnetic semiconductors. Without neglecting higher order terms we obtain the same equation 2.33 as found by Zhu and Flatté [26, 49]. Based on this, the magnetoresistance is calculated for different geometries. We find that the resistance difference between parallel and anti-parallel configuration in a F/I/SC/I/F structure is only of a significant level when the tunnel barrier resistance is approximately equivalent to the resistance of the semiconductor channel. Moreover, in case the MR is caused by spin accumulation in the semiconductor the magnetoresistance should decrease almost exponentially with increasing channel length. In lateral devices the spin polarization in the semiconductor is always small compared to vertical devices. The results of our model are further illustrated by numerical calculations with parameters estimated for CoFe, AlOx and n-type GaAs semiconductor. This results in a magnetoresistance of 8% for lateral devices compared to 13% for vertical devices (conditions: spin diffusion length/channel length equals 5, spin polarization equals 40%, electric field is negligible, injector and detector tunnel barrier resistances normalized by the resistance of the GaAs channel equal 2). If the electric field (applied bias voltage) exceeds a certain critical value in non degenerate semiconductors, there will be two distinct spin diffusion lengths, i.e. up-stream and down-stream spin diffusion lengths. This effect can enhance spin diffusion dramatically and the MR could be as large as 15% for lateral

devices and 25% for vertical devices. Via an extra drain voltage, electric fields can be created such that the MR closely approaches values of vertical devices. It should be noted that these values may be overestimated, because we did not include the dependence of the spin polarization on the bias voltage over the tunnel barriers is not included. Finally, in order to eliminate contributions to Hall effects and AMR, an alternative measurement geometry is described. The disadvantage of a non local measurement is that the expected spin dependent voltage signal is half of the spin dependent voltage signal obtained in a local measurement.

- **GaAs wafer characterization** The determined square resistance and mobility of our GaAs wafer were 51 Ω and 720 $cm^2/V{\cdot}s$ at 5 K respectively, were not in agreement with the expected values (2.5 kΩ and 132 $cm^2/V{\cdot}s$). The cause was an erroneous Si calibration. Therefore, all doping levels were a factor of 10 higher than expected (confirmed by W. van Roy).

- **"Good" tunnel barriers demonstrated.** Current density versus bias voltage characteristics of the tunnel barrier layer is typical for elastic tunneling. However, the measured resistance times area product of $5 \cdot 10^{12}$ $\Omega{\cdot}\mu m^2$ for a 5 μm wide electrode was higher than expected ($1 \cdot 10^5$ $\Omega{\cdot}\mu m^2$. The higher resistance was probably due to PMMA remnants on the surface. The non equal curves for both voltage directions reflect a the presence of a Schottky barrier.

- **"Good" channel insulation demonstrated.** The electrical bonding of the electrodes forced us to sputter a thin high ohmic layer. For this purpose the commonly used insulator silicon dioxide was chosen, and the grow properties in our system and the purity of the layer had to be optimized. Measurements revealed that a higher sputter power, at least 100 W is required for a smooth growth (smaller peak to peak roughness). Metal impurities in our sputtered layer were caused by direct plasma contact with a metal environment. Therefore, a second improvement was a substitution of the iron fixation ring of the target by a ceramic one. We demonstrated that we can fabricate SiO_2 layers with an electrical resistance of above $1 \cdot 10^{13}$ $\Omega \cdot \mu m^2$, measured between two bondingpads.

- **Lithographic defined electrodes (device demonstrated).** Using electron beam lithography, shadow masks with high enough undercuts were fabricated, that lift-off was possible. Ferromagnetic electrodes with width of 200 nm and 500 nm and length of 200 μm were created at a distance of 800 nm. Smaller spacings up to 400 nm were only obtained for wider electrodes (500 nm-1000 nm). More narrow electrodes at closer distances are expected to be possible in future follow-up research.

The first transport measurements show indications of magnetoresistive behavior, but we could not experimentally show any spin valve effect. We conclude that there was no evident proof of spin accumulation in GaAs. In the future, by reducing both the carrier doping of the normal channel and the thickness of the AlOx barrier (i.e. the characteristic resistance area product of the tunnel junctions), better matched devices are expected to show the desired behavior. If the magnetoresistance exponentially decreases with the spacing between the injection and detection electrode (figure 2.13b), we have demonstrated that the magnetoresistance was caused by spin accumulation in GaAs.

Bibliography

[1] G.A. Prinz. *Science*, 282:1660, 1998.

[2] L. Berger. *Physcia*, 30:1141, 1964.

[3] R.I. Potter. *Phys. Rev. B*, 10:4626, 1974.

[4] P.M. Tedrow and R. Merservey. *Phys. Rev. B*, 7:318, 1973.

[5] M.N. Baibich, L.M. Broto, A. Fert, F.N. Van Dau, F. Petroff, A. Friederich, and J. Chazelas. *Phys. Rev. Lett.*, 61:2472, 1988.

[6] M. Julliere. *Phys. Lett.*, 54A:224, 1975.

[7] J.S. Moodera, L.R. Kinder, T.M. Wong, and R. Meservey. *Phys. Rev. Lett.*, 74:3273, 1995.

[8] M. Johnson and R.H. Silsbee. *Phys. Rev. Lett.*, 55:1790, 1985.

[9] S. Datta and B. Das. *Appl. Phys. Lett.*, 56:665, 1989.

[10] J. M. Kikkawa, I. P. Smorchkova, N. Samarth, and D. D. Awschalom. *Science*, 277:1284, 1997.

[11] J.M. Kikkawa and D.D. Awschalom. *Nature*, 397:139, 1999.

[12] G. Schmidt, D. Ferrand, L. Molenkamp, A.T. Filip, and B.J. van Wees. *Phys. Rev. B Rap. Com.*, 62:R4790, 2000.

[13] A.T. Filip. *Spin polarized electron transport in mesoscopic hybrid devices.* PhD thesis, Rijksuniversiteit Groningen, 2002.

[14] E.I. Rashba. *Phys. Rev. B Rapid Comm.*, 62:R16267, 2000.

[15] R. Fiederling, G. Reuscher, W. Ossau, G. Schmidt, A. Waag, and L.W. Molenkamp. *Nature*, 402:787, 2000.

[16] Y. Ohno, D.K. Young, B. Beschoten, F. Matsukura, H. Ohno, and D.D. Awschalom. *Nature*, 402:790, 1999.

[17] H.J. Zhu, M. Ramsteiner, H. Kostial, M. Wassermeier, H.-P. Schönherr, and K.H. Ploog. *Phys. Rev. Lett*, 87:016601, 2001.

[18] S.F. Alvarado and P. Renaud. *Phys. Rev. Lett.*, 68:1387, 1992.

[19] V.F. Montsnyi, J. De Boeck, J. Das, W. Van Roy, G. Borghs, E. Goovaerts, and V.I. Safarov. *Appl. Phys. Lett.*, 81:265, 2002.

[20] M. Tanaka and Y.Higo. *Phys. Rev. Lett.*, 87:026602, 2001.

[21] C.-M. Hu, J. Nitta, A. Jensen, J.B. Hansen, and H. Takayanagi. *Phys. Rev. B*, 63:125333, 2001.

[22] G. Meier, T. Matsuyama, and U. Merkt. *Phys. Rev. B.*, 65:125327, 2002.

[23] R. Mattana, J.-M. George, H. Jaffrés, F. Nguyen Van Dau, A. Fert, B. Lèpine, A. Guivarc'h, and G. Jèzèquel. *Phys. Rev. Lett.*, 90:166601, 2003.

[24] F. Jedema, H. Heersche, A.T. Filip, J.J.A. Baselmans, and B.J. van Wees. *Nature*, 416:713, 2002.

[25] F.J. Jedema. *Electrical Spin Injection in metallic Mesoscopic Spin valves.* PhD thesis, Rijksuniversiteit Groningen, 2002.

[26] Z.G. Yu and M.E. Flatté. *Phys. Rev. B*, 66:201202(R), 2002.

[27] J.H. Davies. *The Physics of Low-dimensional Semiconductors.* Cambridge University Press, Cambrigde, 1998.

[28] S.M. Sze. *Physics of Semiconductor Devices.* Wiley, New York, 1981.

[29] C.B. Duke. *Tunneling in Solids.* Academic Press, London, 1969.

[30] P.R. LeClair. *Fundamental aspects of spin polarized tunneling.* PhD thesis, Technische Universiteit Eindhoven, 2002.

[31] J. G. Simmons. *J. Appl. Phys.*, 34:1793, 1963.

[32] W.F. Brinkman, R.C. Dynes, and J.M. Rowell. *J. Appl. Phys.*, 41:1915, 1970.

[33] M.B. Stearns. *J. Mag. Mag. Mater.*, 8:167, 1977.

[34] E.Y. Tsymbal and D.G. Pettifor. *J. Phys. Cond. Mater.*, 9:L411, 1997.

[35] P.K. de Boer, G.A. de Wijs, and R.A. de Groot. *Phys. Rev. B*, 58:15422, 1998.

[36] R.J. Elliot. *Phys. Rev.*, 96:266, 1954.

[37] Y. Yafet. *Solid State Physics*, volume 14. Academic, New York, 1963.

[38] M.I. D'yakonov and V.I. Perel. *Sov. Phys. JETP*, 33:1053, 1971.

[39] G.L. Bir, A.G. Aronov, and G.E. Pikus. *Sov. Phys. JETP*, 42:705, 1976.

[40] P.H. Song and K.W. Kim. *Phys. Rev. B*, 66:035207, 2002.

[41] J.M. Kikkawa and D.D. Awschalom. *Phys. Rev. Lett.*, 80:4313, 1998.

[42] R.E. Camley and J. Barnas. *Phys. Rev. Lett.*, 63:664, 1989.

[43] J. Barnas, A. Fuss, and P. Gr R.E. Camley.

[44] P.M. Levy, S. Zhang, and A. Fert. *Phys. Rev. Lett.*, 65:1643, 1990.

[45] S.F. Lee, W.P. Pratt, Q. Yang, P. Holody, R. Loloee, P.A. Schroeder, and J. Bass. *J. Magn. Magn. Mater.*, 118:409, 1993.

[46] M. Johnson and R.H. Silsbee. *Phys. Rev. B*, 35:4959, 1987.

[47] P.C. van Son, H. van Kempen, and P. Wyder. *Phys. Rev. Lett.*, 58:2271, 1987.

[48] T. Valet and A. Fert. *Phys. Rev. B*, 48:7099, 1993.

[49] Z.G. Yu and M.E. Flatté. *Phys. Rev. B*, 66:235302, 2002.

[50] K. Flensberg, T.S. Jensen, and N.A. Mortensen. *Phys. Rev. B*, 64:245308, 2001.

[51] I. D'Amico. *Phys. Rev. B*, 69:165305, 2004.

[52] A. Hirschberg. Thermische verschijnselen, 1998.

[53] R.A. Smith. *Semiconductors.* Cambridge Universtity Press, Cambridge, 1978.

[54] I. Malajovich, J.J. Berry, N. Samarth, and D.D. Awschalom. *Nature*, 411:770, 2001.

[55] I. D'Amico and G. Vignale. *Phys. Rev. B*, 62:4853, 2000.

[56] S. Zhang, P.M. Levy, A.C. Marley, and S.S. Parkin. *Phys. Rev. Lett.*, 79:3744, 1997.

[57] A.M. Bratkovsky. *Phys. Rev. B*, 72:2334, 1998.

[58] A.H. Davies and J.M. MacLaren. *J. Appl. Phys.*, 87:5224, 2000.

[59] F.J. Jedema, M.S. Nijboer, A.T. Filip, and B.J. van Wees. *Phys. Rev. B*, 67:085319, 2003.

[60] A. Fert and S. Lee. *Phys. Rev. B*, 53:6554, 1996.

[61] S.F. Lee, W.P. Pratt, Jr., R. Loloee, P.A. Schroeder, and J. Bass. *Phys. Rev. B.*, 46:548, 1992.

[62] R. Coehoorn. Novel magnetoelectronic materials and devices.

[63] R. Meservey and P.M. Tedrow. *Physics Reports*, 238:173, 1994.

[64] R.C. O'Handley. *Modern Magnetic Materials - Principles and Applications.* Wiley-Interscience, Chichester, 2000.

[65] R. Taboryski, T. Clausen, J. Bindsley Hansen, J.L. Skov, J. Kutchinsky, C.B. Sørensen, and P.E¿ Lindelof. *Appl. Phys. Lett.*, 69:656, 1996.

[66] W. Wensdorfer, B. Doudin, D. Mailly, K. Hasselbach, A. Benoit, J. Meier, J.-P. Ansermet, and B. Barbara. *Phys. Rev Lett.*, 77:1873, 1996.

[67] H. Frei, S. Shtrikman, and D. Treves. *Phys. Rev.*, 106:446, 1957.

[68] A. Aharoni. *Phys. Status Solidi*, 16:3, 1966.

[69] M.E. Schabes. *J. Magn. Magn. Mater.*, 95:249, 1991.

[70] Marian A. Herman and Helmut Sitter. *Molecular beam epitaxy : fundamentals and current status.* Springer, Berlin, 1989.

[71] L.J. van der Pauw. *Philips Reseach Reports*, 13:1, 1958.

[72] L.J. van der Pauw. *Philips Research Reports*, 20:220, 1958.

[73] John A. Venables. *Introduction to Surface and Thin Film Processes.* Cambridge University Press, Cambridge, 2000.

Chapter 5

Appendix

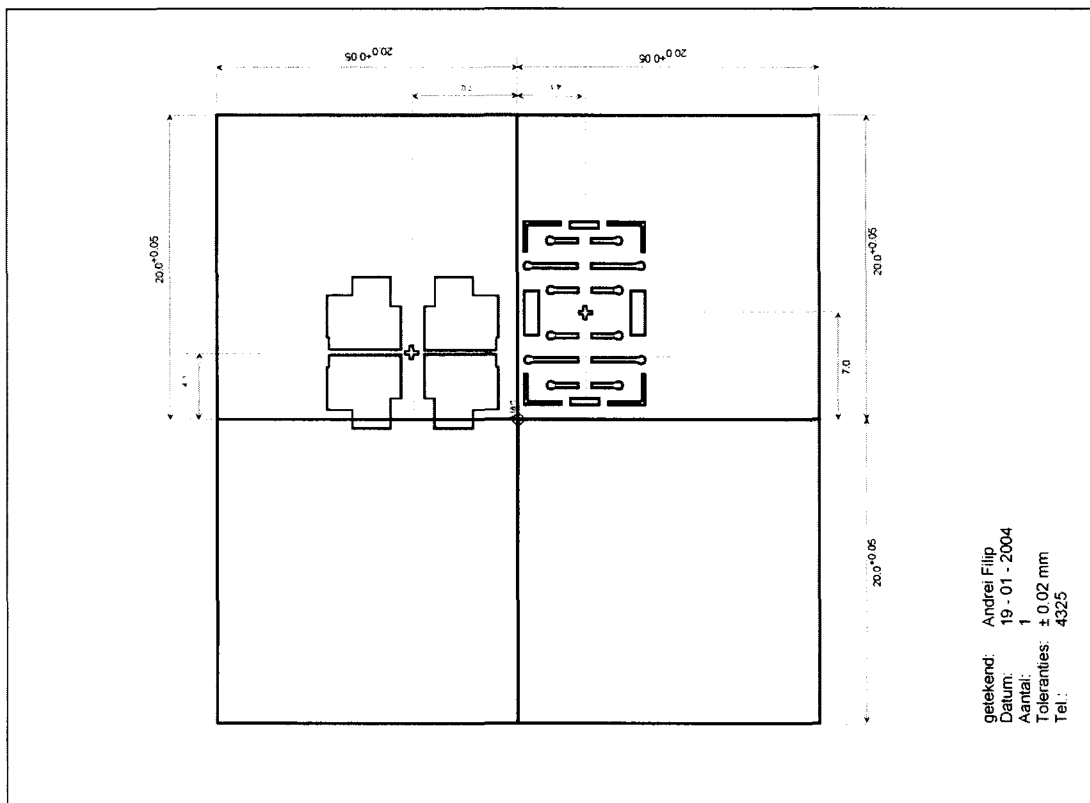

Figure 5.1: Drawing of the mask layout, which is used for sputtering the Ta bonding pads (first quadrant) and the SiO_2 isolation (second quadrant).

Figure 5.2: (Top) Specifications of the first quadrant. (Bottom) Specifications of the second quadrant.

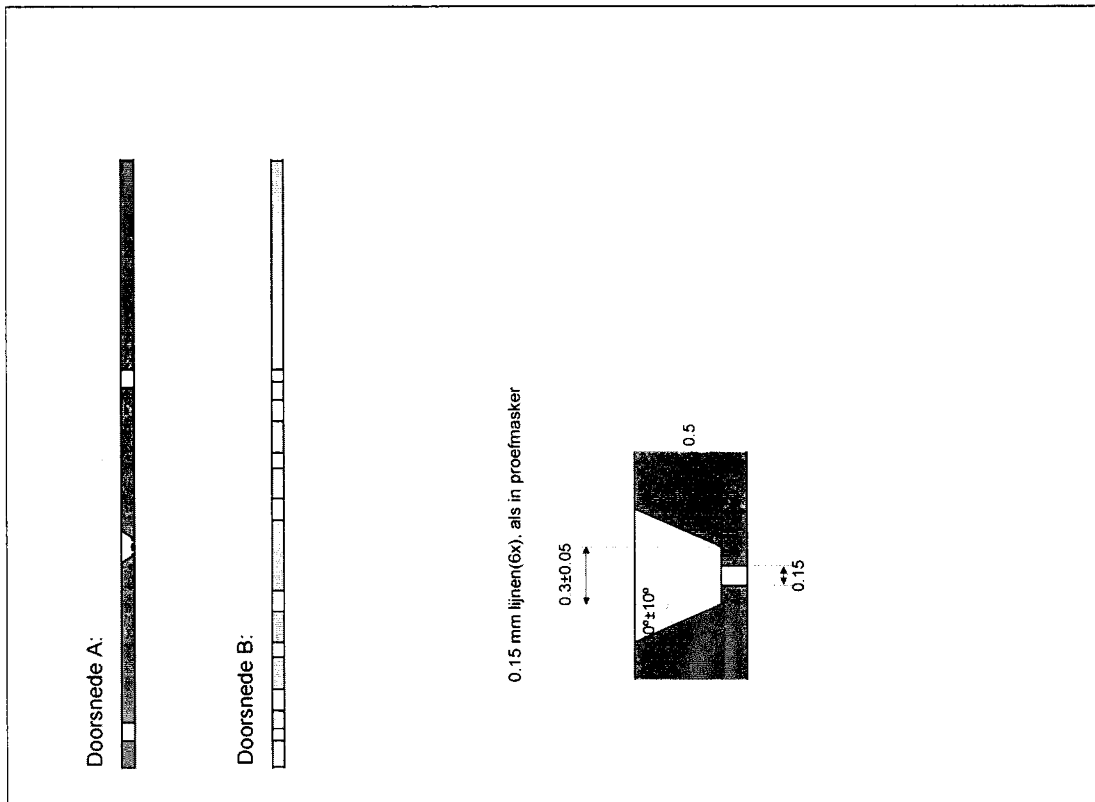

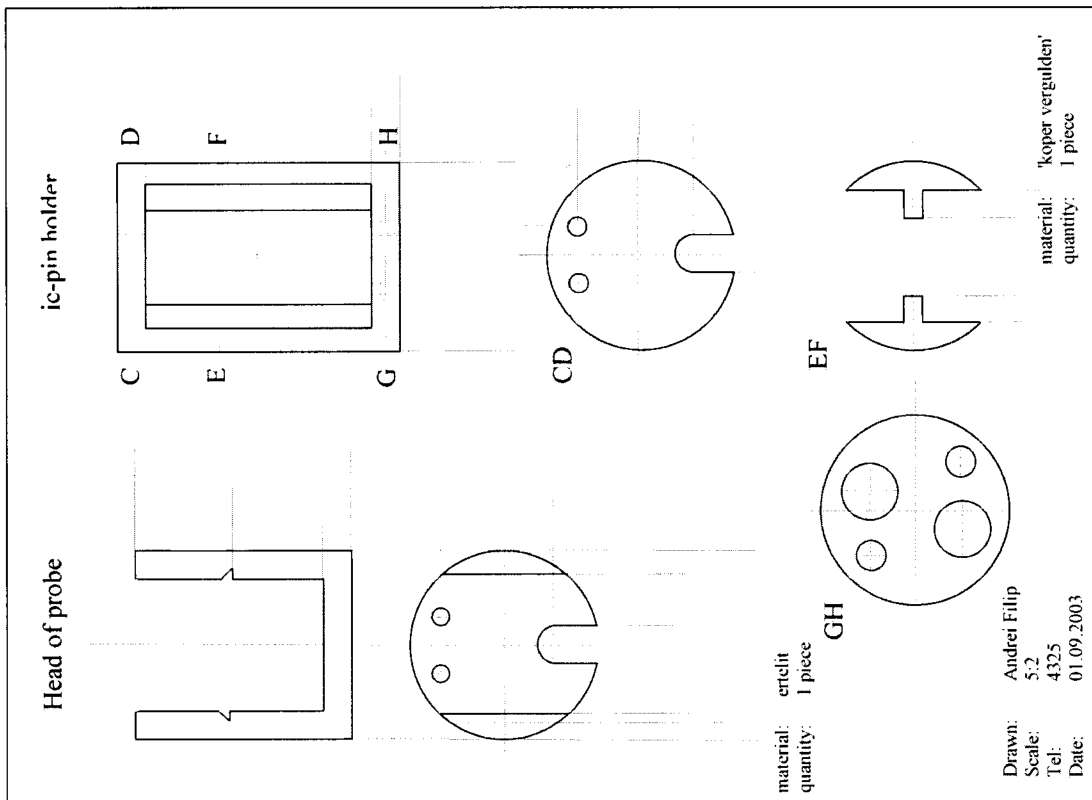

Figure 5.3: (Top) Side view of the mask. (Bottom) Drawing of the head piece and connection part (holder) to the probe.

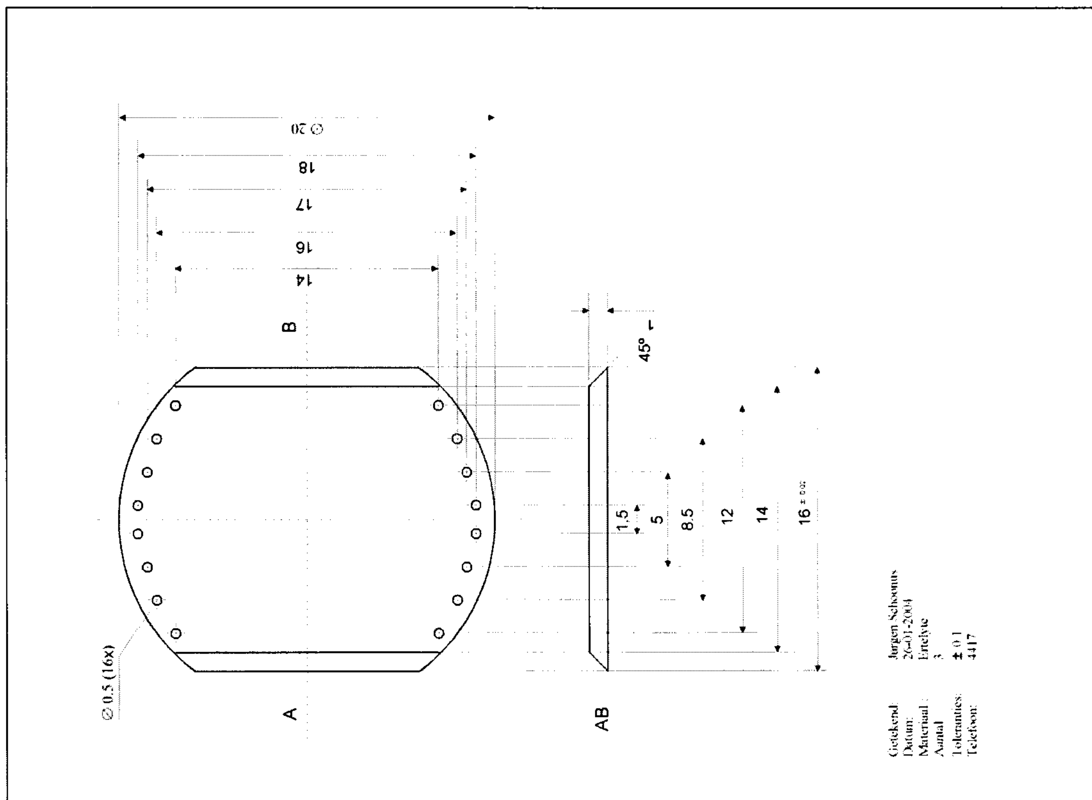

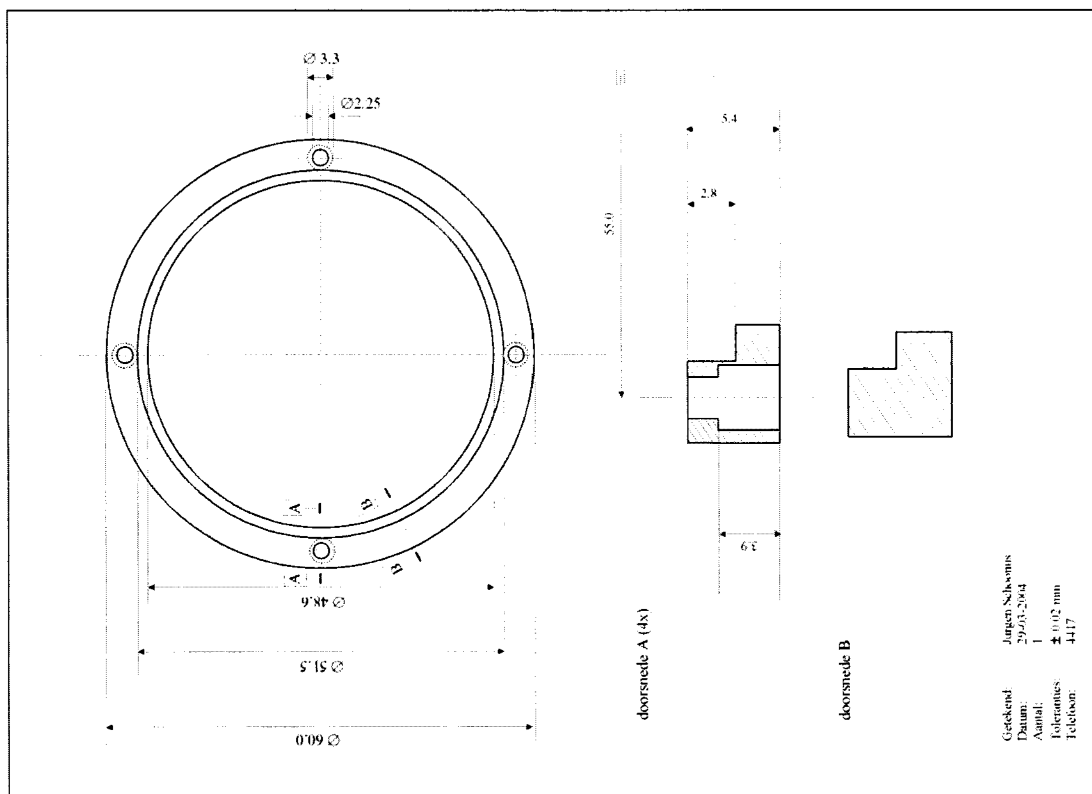

Figure 5.4: (Top) Removable sample holder. (Bottom) Drawing of the alumina ring for fixation of the SiO_2 in the sputter chamber.

Dankwoord

Gedurende het afgelopen jaar heb ik met veel plezier mijn afstudeeronderzoek binnen de capaciteits groep Fysica van Nanostructuren kunnen doen. Op deze plaats wik ik graag al diegenen bedanken die hieraan een bijdrage hebben geleverd. Een aantal mensen wil ik echter in het bijzonder bedanken.

Op de eerste plaats wil ik Andrei Filip bedanken voor zijn enthousiaste begeleiding en zijn nimmer aflatende behulpzaamheid. Tijdens discussies weet hij altijd potentiële oplossingen aan te dragen voor de op dat moment nog onverklaarbare resultaten. Daarnaast ben ik Henk Swagten erkentelijk voor zijn sturende adviezen, inspirerende opmerkingen en het zorgvuldig doorlezen en becommentariëren van dit verslag. Bert Koopmans bedank ik voor het creëren van het project en de nuttige discussies over het werk.

Uitdrukkelijk ben ik Wim van Roy en Jo de Boeck, verbonden aan IMEC Leuven, België dank verschuldigd voor de MBE gegroeide halfgeleider heterostructuren. Fouad Karouta en Erik Jan Geluk van de Opto-Electronic Devices Group, Faculteit Electrotechniek voor het mogen gebruiken van de voor lithografie aangepaste SEM en de vakkundige hulp bij talloze problemen. Verder ben ik Marc van Maris van de Mechanics of Materials Group, Faculteit Werktuigbouwkunde zeer dankbaar voor het beschikbaar stellen van de 'phasecontrast lightmicroscope'. Tenslotte bedank ik Friso Jedema en Willem op 't Root van Philips Research voor hun getoonde belangstelling in mijn werk.